DIRECT AND LARGE-EDDY SIMULATION OF THE COMPRESSIBLE TURBULENT MIXING LAYER

BERT VREMAN

DIRECT AND LARGE-EDDY SIMULATION OF THE COMPRESSIBLE TURBULENT MIXING LAYER

PROEFSCHRIFT

ter verkrijging van
de graad van doctor aan de Universiteit Twente,
op gezag van de rector magnificus,
Prof.dr. Th.J.A. Popma,
volgens het besluit van het College voor Promoties
in het openbaar te verdedigen
op donderdag 14 december 1995 te 15.00 uur

door

Albertus Willem Vreman

geboren op 17 mei 1968
te Aalten

Dit proefschrift is goedgekeurd door de promotor en de assistent-promotor:

Prof.dr.ir. P.J. Zandbergen
Dr.ir. B.J. Geurts

Voorwoord

Het vierjarig onderzoek waaruit dit proefschrift voortvloeide heb ik verricht als lid van de vakgroep Toegepaste Analyse van de faculteit Toegepaste Wiskunde aan de Universiteit Twente. Het proefschrift handelt over de compressibele turbulente menglaag bestudeerd met de directe en large-eddy simulatie technieken. Ongeveer vijf jaren geleden begon men in deze vakgroep compressibele turbulente stromingen te onderzoeken met deze technieken en na verloop van tijd zijn steeds meer mensen in de groep zich hiermee intensief gaan bezighouden. Velen hebben aan het tot stand komen van dit proefschrift bijgedragen, een ieder op zijn eigen manier. Enkelen noem ik hieronder.

Allereerst bedank ik professor Zandbergen voor de gelegenheid die hij mij bood om de afgelopen vier jaar te werken aan dit uitdagende onderwerp en voor zijn supervisie daarbij.
De directe begeleiding werd gegeven door Bernard Geurts en Hans Kuerten. Bernard en Hans, deze begeleiding was niet alleen adequaat, maar ook enthousiast en vriendschappelijk, zodat ik de samenwerking als zeer prettig heb ervaren.
Vele andere collega's hebben ervoor gezorgd dat mijn werkomgeving een aangename omgeving was. Een bijzondere rol vervulden daarin mijn kamergenoten van wie ik Marijke Vallentgoed met name noem. De eerste drie jaren deelde ik mijn werkplek met haar en ik heb goede herinneringen aan de leuke sfeer met heel wat luchtige, maar ook openhartige en van tijd tot tijd diepgaande gesprekken.
Een deel van het onderzoek vond plaats in de faculteit Aeronautical Engineering van het Queen Mary and Westfield College te Londen gedurende de eerste tweeënhalve maand van dit jaar. Ik bedank Neil Sandham en zijn promovendi samen met Kai Luo dat ze me opnamen in hun groep. De fysische expertise van Neil was heel stimulerend voor mijn onderzoek.

Door mijn vriendschap met Cornelise, nu mijn vrouw, waren de laatste achttien maanden van mijn promotie het mooist. Cornelise, ik waardeer enorm dat je in mijn promotieonderzoek interesse toonde, daarin naast mij wilde staan en me hielp waar je kon.
Ook ben ik mijn ouders, broers, zus en vele andere goede vrienden heel dankbaar voor de rol die zij in mijn leven tot nu toe hebben gespeeld.

Het meest gaat echter mijn dank uit naar God, mijn hemelse Vader. Hij, de Gever van alle goede dingen, gaf mij de gezondheid, kracht en motivatie om dit werk te voltooien.

Enschede, november 1995 *Bert Vreman*

Contents

Chapter 1

Introduction

Turbulence, the chaotic and apparently unpredictable state of a fluid, is one of the most challenging problems in fluid dynamics. The smoke of a fire, the wake generated by a moving ship and the flow near a flying aeroplane are examples of turbulent flows. Since turbulence strongly increases the mixing and friction in flows, it is an issue of great practical significance in technology. Numerous scientists have put much effort into the observation, description and understanding of turbulent flows. More than a century ago Reynolds (1883) demonstrated that a flow changes from an orderly to a turbulent state when a certain parameter, now called the Reynolds number, exceeds a critical value. Furthermore, an hierarchy of eddies (whirls) from large to small scales exists in turbulent flows, in which larger eddies transfer energy to smaller eddies, whereas the smallest eddies are dissipated by molecular viscosity. Richardson (1922) formulated this energy cascade process as follows: "Big whirls have little whirls, which feed on their velocity, and little whirls have lesser whirls, and so on to viscosity." Using the energy cascade theory, another famous scientist, Kolmogorov (1941), formulated physical laws for the various scales present in a turbulent flow.

Currently, several approaches to study turbulent flows exist: analytical theory, physical experiment and numerical simulation. The complexity of the problem strongly slows down progress in the analytical approach. Experimental research has been conducted for many years and will remain of fundamental importance in this field. Closely connected with the increase of computational power in recent years, growing attention is paid to the numerical simulation of turbulence, which is also the approach followed in this thesis. This approach is advantageous over experiments when many flow quantities at a single instance or quantities which are difficult to measure are needed. However, the speed and memory size of computers restrict the ability to simulate turbulence, dependent on the amount of scales present in the flow and the complexity of the flow configuration.

We can distinguish between incompressible and compressible turbulent flows. A fluid is called compressible if the density is variable, otherwise it is called incompressible. Compressibility is a fluid property which makes a turbulent fluid even more complicated. Most turbulent research has been directed towards incompressible flow. While incompressible turbulence is still far from understood, even much less is known about its compressible counterpart. Especially when the velocities in the fluid reach values near or higher than the speed of sound, compressibility has a considerable effect on the flow and shock-waves can occur. Renewed interest in high-speed flows from aircraft industry has stimulated fundamental research in the field of compressible turbulence (Lele 1994). In this thesis we consider the turbulent mixing of two adjacent streams of compressible fluid with different speeds. This flow is investigated in the regimes of low, moderate and high compressibility.

Large-Eddy Simulation is an important technique used in the numerical simulation of turbulence. The main purpose of this thesis is to advance this technique for compressible flows. The first section gives an overview of the techniques used in the numerical simulation of turbulence and, in particular, it introduces the Large-Eddy Simulation technique. In order to test existing and new Large-Eddy Simulation models, simulations of a specific three-dimensional turbulent flow have to be conducted. The specific flow simulated in this thesis is the compressible mixing layer, important in many technological applications. Apart from the purpose of testing Large-Eddy Simulation, the simulations of the compressible mixing layer are used to address a number of unanswered important questions about physical processes in this flow. An introduction to the compressible mixing layer is given in section two. After these introductions, we formulate our aims in detail in the third section.

1.1 Numerical simulation of turbulence

The starting point for the numerical simulation of compressible turbulence is formed by the Navier-Stokes equations, which represent conservation of mass, momentum and energy. The conceptually most straightforward technique in the simulation of turbulence is Direct Numerical Simulation (DNS), which directly solves the Navier-Stokes equations using a numerical algorithm (Rogallo & Moin 1984). This 'brute force' approach attempts to solve all spatial and temporal fluctuations in the fluid and, consequently, has to cover a wide range of scales. The computational grid should be sufficiently fine, since all these scales have to be represented on the grid. The DNS provides the flow variables ρ, p and the three velocity components u_i, which fluctuate in time and space. These variables contain all the relevant scales of motion, i.e. the DNS is fully resolved. The

amount of relevant scales in a turbulent flow increases if the Reynolds number increases. The Reynolds number is defined as

$$Re = \frac{\rho_R u_R L_R}{\mu_R}, \tag{1.1}$$

where ρ_R, u_R, L_R and μ_R represent a reference density, velocity, length and viscosity, respectively. This number can be interpreted as the ratio between inertial and viscous forces. Small scales in a turbulent flow are generated by the inertial forces and dissipated by the viscous forces. The viscous forces are relatively small if the Reynolds number is high, which leads to the formation of a relatively large amount of small scales. With the current computational capacity DNS is only feasible for turbulent flows in simple geometries at relatively low Reynolds numbers.

In order to reduce the amount of scales to be solved, an averaging operator can be applied to the Navier-Stokes equations. The classical averaging operator is the ensemble average (Monin & Yaglom 1971), which leads to the Reynolds-Averaged Navier-Stokes equations (RANS). The averaging of nonlinear terms introduces new unknowns in the equations, for which a turbulence model is adopted. The RANS-technique only solves ensemble averaged quantities, describing the mean flow. In contrast to DNS, this computational technique can presently be applied to flows in complex geometries and at high Reynolds numbers. For these reasons, it is widely used in engineering practice. However, the errors introduced by the turbulence modelling reduce the accuracy and more detailed information than provided by the ensemble averaged quantities is often required. For example in aerodynamic applications high accuracy is required, whereas the the available turbulence models lead to poor predictions, especially when shocks and separation are present.

The third technique distinguished here, Large-Eddy Simulation (LES), does not solve the full range of scales either (unlike DNS), but it solves a much larger range of scales than RANS does. In LES the large eddies are solved, which correspond to large scales, while effects of the small eddies are modelled. In this approach the averaging operator is not the ensemble average, but a filter which is a local weighted average over a volume of fluid. Consequently, the LES-formulation employs filtered flow variables, denoted by $\overline{\rho}$, $\overline{p}$ and $\widetilde{u}_i$. The basic filtering is denoted by an overbar, from which a related filtering, needed for compressible flows and denoted by a tilde, is derived. The filtering depends on the filter width Δ, which is a characteristic spatial length-scale, and has approximately the effect that scales larger than Δ (resolved scales) are still present in the filtered variables, whereas contributions of scales smaller than Δ (subgrid scales) have been removed. Application of this averaging procedure to the Navier-Stokes equations yields the filtered Navier-Stokes equations. Like the ensemble averaging, the fil-

tering introduces unknown quantities, so-called subgrid-terms, which have to be modelled in order to close the system of equations. In LES the filtered equations are solved with a numerical algorithm and the resulting filtered variables describe the large-scale motion of the flow. The filtered variables contain much more information than the mean flow solved with the RANS-approach, since only the small-scale turbulence is modelled, instead of the full turbulence. Hence LES is potentially more accurate than RANS, since less modelling errors are introduced. In addition the demand for computer resources in LES is considerably smaller than in DNS, because not all scales need to be solved. Consequently, LES is more likely to become an engineering tool than DNS, since more complicated flows at higher Reynolds numbers can be simulated.

The modelling of the unknown quantities introduced by filtering is called subgrid-modelling. The models involved, referred to as subgrid-models, express the subgrid-terms in filtered flow variables. With respect to the accuracy of LES, subgrid-modelling is an important issue, and, consequently much effort has been put into the development of subgrid-models. For the testing of subgrid-models we distinguish between so-called *a priori* and *a posteriori* tests. Both types of tests require accurate data of a turbulent flow as a point of reference, which can be obtained by experiment or DNS. In this work we choose to use DNS-data for the testing of subgrid-models, since especially for compressible flows detailed experimental data is not easily available. Unfortunately, DNS-data can presently only be obtained for relatively low Reynolds numbers and, consequently, the tests formally validate LES of turbulent flows at low Reynolds number only. However, even low Reynolds number flows can exhibit turbulent behaviour. Furthermore, several important conclusions drawn from tests at low Reynolds numbers do not alter if the tests are performed using experimental data at high Reynolds number (Liu *et al.* 1994).

Figure 1.1 schematically shows the set-up of *a priori* tests for the most important subgrid-term, the turbulent stress tensor

$$\tau_{ij} = \widetilde{u_i u_j} - \widetilde{u}_i \widetilde{u}_j. \tag{1.2}$$

The symbol m_{ij} in the figure represents the subgrid-model for this tensor. The calculation of τ_{ij} starting from the DNS velocity field u_i is straightforward. Since the subgrid-model is a function of filtered variables only, m_{ij} is evaluated starting from the filtered velocity field $\widetilde{u}_i$. The final step in the *a priori* test is the comparison between the model m_{ij} and the exact subgrid-term τ_{ij}. The level of agreement between these two tensors, which can be expressed by a correlation coefficient, measures the quality of the model. This procedure of testing is called *a priori* testing, since no actual Large-Eddy Simulations are performed. Results of *a priori* tests are certainly of some value, but require a careful interpretation.

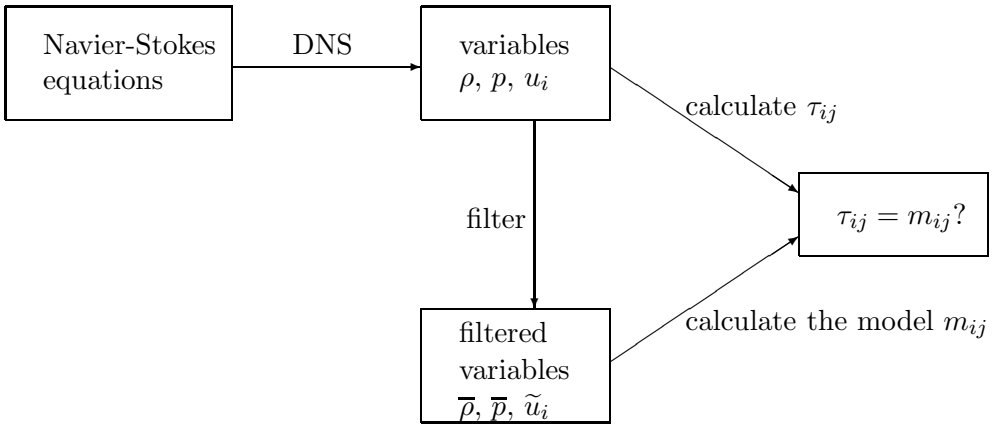

Figure 1.1: Diagram illustrating the technique of *a priori* testing for the turbulent stress tensor τ_{ij}.

They often tend to be too pessimistic, since low correlations between stresses and predictions do not necessarily lead to poor results when the model is implemented in an actual LES (Reynolds 1990; Meneveau 1994). A subgrid-model with a low correlation can still provide reasonable results if it correctly models the turbulent dissipation process. On the other hand, high *a priori* correlations do not necessarily result in an accurate LES. Despite high correlations, models can lead to unstable simulations due to insufficient turbulent dissipation (Vreman *et al.* 1994f).

For these reasons, investigation of the behaviour of subgrid-models in actual simulations is indispensable in order to draw conclusions about the performance of models . *A posteriori* testing, schematically illustrated in figure 1.2, meets this requirement. As in the previous approach, DNS is performed, providing the flow field, which is subsequently filtered in order to obtain the filtered variables. The single arrows in figure 1.2 indicate this route. The other route, indicated by double arrows, also provides a filtered flow field, but now by solving the filtered Navier-Stokes equations using LES with a given subgrid-model. Both routes will result in identical filtered variables for a perfect LES. The level of agreement between the two results measures the quality of the Large-Eddy Simulation.

Discrepancies between filtered DNS and LES-results are introduced by both the subgrid-model and the numerical algorithm. The computational grid-size h is usually taken of the order of the filter width, $h = \Delta$ or $h = \frac{1}{2}\Delta$, which shows that the smallest scales in the filtered field are represented on only a few grid-points. Consequently, not only the physical subgrid-modelling error, but also

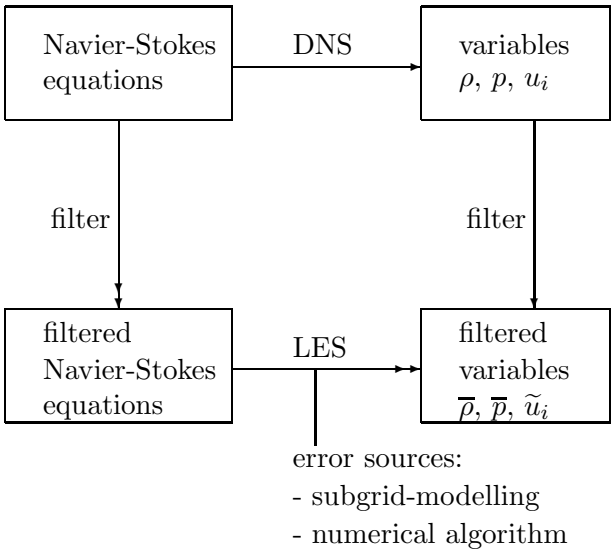

Figure 1.2: Diagram illustrating the technique of *a posteriori* testing.

numerical errors are expected to affect the results. In actual LES these sources of errors interact, which complicates *a posteriori* testing, since the separation of subgrid-modelling and numerical effects in the final discrepancies is difficult. In literature the numerical effects in LES have not been studied in detail; most research has been directed towards the issue of subgrid-modelling. With respect to subgrid-modelling, most effort has been put into the development of models for incompressible flow. In the filtered incompressible Navier-Stokes equations, the turbulent stress tensor, appearing in the momentum equation, is the only subgrid-term. Compressible LES, however, incorporates the filtered energy equation, which introduces several additional subgrid-terms. Almost no research has been directed towards the subgrid-modelling of these compressible quantities.

In the following, we give a rough overview of the developments in the modelling of the most important subgrid-term, the turbulent stress tensor. Since the foundation of LES, which was laid by the meteorologists Smagorinsky (1963), Lilly (1967) and Deardorff (1970), the most popular subgrid-model has been the Smagorinsky model. The model employs an eddy-viscosity, which like molecular viscosity extracts energy from the resolved scales in the simulation. The eddy-viscosity is introduced in order to mimic the turbulent cascade process, transferring energy from the resolved to the subgrid-scales. Successful LES has been performed using the Smagorinsky model, especially for homogeneous and

statistically stationary turbulence. However, in more complicated flows the model does not predict the correct energy transfer in near-wall regions and transitional stages. In order to overcome these deficiencies, Germano (1992) formulated the dynamic eddy-viscosity model, replacing the model constant in the Smagorinsky model with a time- and space-dependent model coefficient. A dynamic procedure adjusts this coefficient to the local turbulence in such a way that locally the correct energy dissipation is provided.

Although the Smagorinsky model in combination with the dynamic procedure is able to provide locally the correct energy dissipation, it has repeatedly been observed that the correlation between the model and the exact turbulent stress is poor. Alternatively, other subgrid-models have been proposed, which do not use an eddy-viscosity hypothesis. An example is the 'gradient' model (Clark *et al.* 1979), which is based on the substitution of Taylor expansions of the unfiltered velocity in terms of the filtered velocity into equation (1.2). Furthermore, Bardina *et al.* (1984) proposed the similarity model, which is obtained if the definition of the turbulent stress tensor (1.2) is applied to the filtered velocity $\widetilde{u}_i$ instead of the unfiltered u_i. However, the gradient and similarity models are not purely dissipative and, consequently, they can give rise to numerical difficulties in actual simulations. Aspects of these three types of basic subgrid-models (eddy-viscosity, gradient and similarity) will further be studied in this thesis in combination with the dynamic procedure. In each case the incorporation of the dynamic procedure will be found to improve the results.

1.2 The compressible mixing layer

Compressible free shear layers occur in many complex problems of technological importance. An example is the flow behind an aerofoil, where two streams of air with different velocities join. The amount of turbulence near an aerofoil is desired to be as low as possible, since turbulence increases the drag of the vehicle. Another case is the flow in jet-propulsion engines based on supersonic combustion, where the efficiency depends on the time needed to mix fuel and oxidizer in the combustor (Lu & Wu 1991; Sandham & Reynolds 1991). For this reason the mixing conditions for free shear layers in such systems should be maximized. To improve such conditions, turbulence plays a central role, since it greatly enhances the mixing properties of a flow. A prototype free shear flow is the mixing layer, which is introduced in this section.

The mixing layer can be studied in a spatial or temporal framework. In experiments the mixing layer is generated by a splitter plate separating two streams of fluid with different speeds. The mixing layer develops from the location where the streams come together, and its thickness increases as a function of the spatial

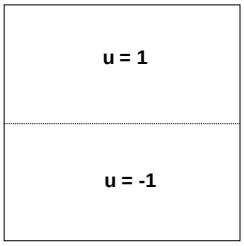

Figure 1.3: Configuration of the temporal mixing layer.

coordinate in the streamwise direction. Numerical simulations of such spatially developing mixing layers have mainly been performed in two dimensions, because the demand on computational resources is very high, since a large extent of the computational box in the streamwise direction is required. For this reason the temporal mixing layer is considered, which qualitatively exhibits the same physical phenomena as the spatial case, but requires an order of magnitude less computational effort. In the temporal framework a computational box is considered which is relatively small in the streamwise direction. This computational domain can be interpreted as a 'window' over the mixing layer that moves with the centre plane velocity in the streamwise direction. In this frame of reference the thickness of the layer increases as a function of time rather than as a function of the streamwise coordinate.

Figure 1.3 illustrates the configuration of the temporal mixing layer. A coordinate system convecting with the mean velocity in the centre plane has been adopted and in this frame of reference the layer contains two streams with equal and opposite free-stream speed U, which is used as reference velocity. Other reference values are half the initial vorticity thickness (L_R) and the free-stream values for the density (ρ_R), temperature (T_R) and viscosity (μ_R). In this case the free-stream Mach number M is equal to the convective Mach number. The convective Mach number is the most important parameter in the characterization of intrinsic compressibility effects. It was introduced by Bogdanoff *et al.* (1983) and extensively used by Papamoschou & Roshko (1988). For streams with equal ratio of specific heats we have $M = (U_1 - U_2)/(c_1 + c_2)$, where U_1 and U_2 are the two free-stream velocities and c_1 and c_2 are the free-stream sound speeds. In our case $U_2 = -U_1$ and $c_1 = c_2$.

We consider the three-dimensional temporal mixing layer in the rectangular domain $[0, L_1] \times [-\frac{1}{2}L_2, \frac{1}{2}L_2] \times [0, L_3]$, where L_1, L_2 and L_3 correspond to the streamwise (x_1), normal (x_2) and spanwise (x_3) directions, respectively. Periodic boundary conditions are imposed in the stream- and spanwise directions,

$$\Phi(x_1 + L_1, x_2, x_3, t) = \Phi(x_1, x_2, x_3, t) = \Phi(x_1, x_2, x_3 + L_3, t) \tag{1.3}$$

where Φ represents an arbitrary flow variable. The boundaries in the normal direction are free-slip walls, which implies a zero normal velocity and zero normal derivatives of density, pressure and tangential velocities. The initial mean velocity profile is the hyperbolic tangent profile,

$$u_1 = \tanh(x_2), \quad u_2 = u_3 = 0, \tag{1.4}$$

whereas the initial temperature profile is obtained from the Busemann-Crocco law (Ragab & Wu 1989),

$$T = 1 + \tfrac{1}{2}(\gamma - 1)M^2(1 - u_1)(u_1 - 1), \tag{1.5}$$

where γ is the ratio of the specific heats C_P and C_V. From the temperature and a uniform mean pressure distribution ($p = 1/(\gamma M^2)$), the density is obtained using the equation of state for an ideal gas. In order to initiate turbulence, a perturbation consisting of eigenfunctions provided by linear stability theory is superimposed on the mean profile (Sandham & Reynolds 1991).

Linear stability theory is essential to understand the initial development of the flow. In this theory the Navier-Stokes equations are linearized around the mean profile to obtain equations for the disturbances around the mean flow field. Each wave disturbance is represented in the form,

$$\phi = \hat{\phi}(x_2)e^{i(\alpha x_1 + \beta x_3 - ct)}, \tag{1.6}$$

where the real part of ϕ is a disturbance on the mean profile of ρ, u_i or T. The parameters α and β are the real wave numbers characterizing the specific mode. Substitution of this disturbance in the linear stability equations yields an eigenvalue problem with complex eigenvalue $c = c_r + ic_i$ and complex eigenfunction $\hat{\phi}$. Instability corresponds with a positive growth rate ($c_i > 0$) and, consequently, an exponential growth of the wave disturbance. The most unstable mode is determined by a pair (α, β) that yields a maximum growth rate. The initial mean flow can also be perturbed with uniform noise. In that case the most unstable mode will be amplified most and will become dominant in the linear regime. Linear stability theory thus describes the flow in the linear regime, which lasts until nonlinear effects set in when the perturbations have grown sufficiently large. The linear stability of the mixing layer has thoroughly been investigated (Michalke 1964,

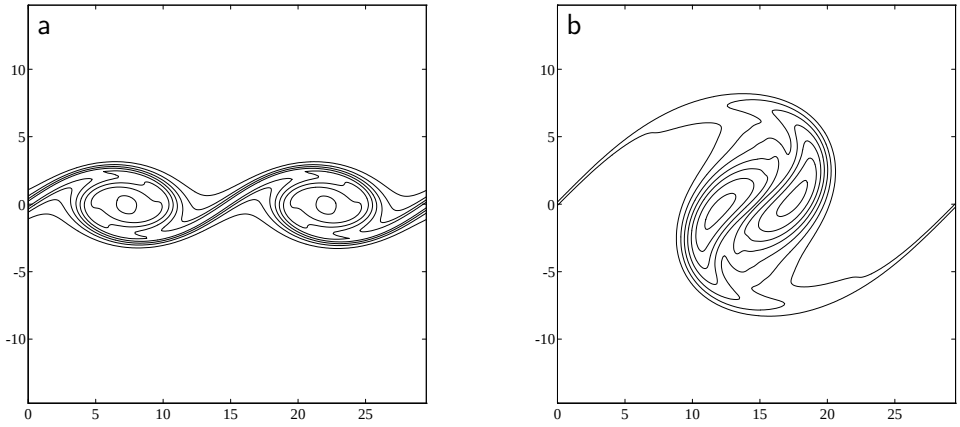

Figure 1.4: Contours of spanwise vorticity in the two-dimensional mixing layer showing the formation of vortices (a) and subsequent pairing (b).

Blumen 1970, Sandham & Reynolds 1991). It was found that for incompressible (M=0) up to moderately compressible flows (M=0.6) the most unstable mode is two-dimensional ($\beta = 0$). If the convective Mach number is higher ($M > 0.6$) a pair of opposite oblique modes, (α, β) and $(\alpha, -\beta)$ with $\beta \neq 0$ becomes most unstable and the primary instability is three-dimensional. The magnitude of the linear growth rate of the most unstable mode decreases if the Mach number increases. Thus, if the Mach number increases from $M = 0$, the growth rate of the most unstable two-dimensional wave decreases. At about $M = 0.6$ the dominant two- and three-dimensional instabilities are equally amplified, whereas beyond this Mach number the most unstable wave is three-dimensional.

In order to give a first impression of the mixing layer, we discuss the evolution of the mixing layer in the nonlinear stages for the two-dimensional case. The two-dimensional mixing layer has numerically been investigated for several Mach numbers using both the temporal and the spatial approach (Lesieur *et al.* 1988; Sandham & Reynolds 1989; Ragab & Sheen 1992; Vreman *et al.* 1995a). In these simulations the two-dimensional instability, amplified in the linear regime, saturates when nonlinear effects set in, leading to the formation of a row of spanwise vortices. If in the temporal case L_1 equals n times the wave length of the dominant mode, a row of n spanwise vortices form in the computational domain (Lesieur *et al.* 1988, Lesieur 1990). In the further evolution of the flow adjacent vortices start to rotate around a common centre and merge. Vortices formed by merging subsequently pair with other vortices. Figure 1.4 shows the formation

and the subsequent pairing of vortices in a simulation with $n = 2$ (Vreman *et al.* 1995a). The nonlinear processes considerably stimulate the growth of the thickness of the shear layer compared to the laminar growth in the linear regime. When the Mach number is larger than 0.7, supersonic regions occur in the flow and shock-waves form on top of the vortices (Sandham & Reynolds 1989; Lele 1989).

The development of the three-dimensional mixing layer is quite different from the two-dimensional case, especially for high Mach numbers where the primary instability is three-dimensional. Numerical simulations for the three-dimensional mixing layer have been performed within the temporal framework only. First, we turn to the incompressible case, which has been investigated by Moser & Rogers (1993) and Comte *et al.* (1992). The primary instability is two-dimensional, therefore two-dimensional rollers of spanwise vorticity develop, perpendicular to the stream-wise direction. As in the two-dimensional case these large-scale structures pair, resulting in larger rollers which subsequently merge. However, in the three-dimensional case the primary instability forming these rollers is followed by a three-dimensional secondary instability, producing braids of streamwise vorticity between the rollers. These instabilities are followed by a transition to small-scale turbulence, resulting in a complicated disordered flow, although the roller structures can still be discerned.

With respect to the compressible mixing layer in three dimensions, the flow exhibits features similar to the incompressible case, if the Mach number is low. However, at higher Mach numbers ($M > 0.6$) the scenario is different, since the primary instability is then three-dimensional. From this instability a staggered pattern of Λ-vortices develops, instead of the rollers perpendicular to the stream-wise direction. Recent simulations at $M = 0.8$ demonstrate that after the Λ-vortices have developed, the transition to small-scale turbulence starts, accompanied by an enhanced mixing of the flow (Luo & Sandham 1994, 1995). In contrast to the two-dimensional mixing layer, no shocks occur in the three-dimensional case up to $M = 1.05$ (Sandham & Reynolds 1991), and whether they occur in three-dimensional flows at higher Mach number was until recently an open question (Lele 1994, Vreman *et al.* 1995f). A well established compressibility effect is the reduced non-dimensionalised turbulent shear layer growth with increased Mach number (Brown & Roshko 1974). Although this effect has been widely debated in literature, no convincing explanation of the reduced growth rate in the turbulent regime has been given.

In this thesis results of three-dimensional numerical simulations will be presented for three different Mach numbers: low compressibility ($M = 0.2$), moderate compressibility ($M = 0.6$) and high compressibility ($M = 1.2$). Examination of the DNS-results at $M = 1.2$ reveals the occurrence of shocks in the turbulent

regime. Furthermore, we will analyse the mechanism responsible for the reduced growth rate in compressible mixing layers.

1.3 Purpose and outline

In this section we formulate our research questions more specifically and give a global overview of the contents of the following chapters. The primary aim of this thesis is further development of LES for compressible flows. We have selected the compressible mixing layer in order to develop the LES-technique for compressible flow. The mixing layer evolves from a laminar to a turbulent state, thus the complete path from transition to turbulence is incorporated in the testing of subgrid-models. Since the flow is strongly affected by compressibility, it is also a suitable test-case for compressible subgrid-modelling. The testing procedures of LES, introduced in section 1, require both DNS and LES. The simple configuration of the flow and the relatively fast evolution into a turbulent state are appropriate to make DNS possible. On the other hand, DNS of the mixing layer will not serve as a data-base for the testing of LES only. The second aim of this thesis is to investigate the physical phenomena in the mixing layer at high Mach numbers. In the following we discuss the research questions corresponding to the two aims of this thesis.

In order to develop LES models for compressible flow simulations, we will first turn to questions regarding the modelling of the turbulent stress tensor. This tensor is not a compressibility term and, consequently, these questions are also relevant for incompressible LES. We will consider a number of subgrid-models for the turbulent stress tensor, including dynamic models (chapter 3). The recently developed dynamic procedure has been a major step forward in LES of transitional and inhomogeneous flows. The dynamic procedure is usually applied in conjunction with the Smagorinsky model and the question arises whether the procedure could also improve other subgrid-models. In addition to the standard dynamic eddy-viscosity model, we will present the dynamic mixed and Clark models. The dynamic mixed model has appeared in literature before, but contains a mathematical inconsistency, which is removed in our formulation. Furthermore, an exact relation between the different filter widths in the dynamic procedure does not exist for top-hat filters. We will derive an approximate relationship, which is optimal in a certain sense.

Another research question concerns the combination of filter and subgrid-model. It is generally assumed that the choice of a specific model is not related to the filter choice. However, we will show that the turbulent stress tensor is positive definite for certain filters only (chapter 4). The requirement that a subgrid-model should also be positive definite in such cases yields constraints on

the choice of the subgrid-model given a certain filter type.

Which model has to be preferred in actual Large-Eddy Simulations is the third question that needs to be answered. Many subgrid-models for the turbulent stress tensor are available, but systematic comparisons of the performance of a wide range of subgrid-models in an inhomogeneous flow are rarely found in literature. Such a comparison for the mixing layer at low Mach number will be presented in chapter 5. For this purpose, we will perform DNS of the mixing layer at $M = 0.2$ and compare the filtered results with LES incorporating the subgrid-models from chapter 3. Large-Eddy Simulations using these subgrid-models at high Reynolds number will also be conducted. It will appear that the dynamic models are considerably better than the non-dynamic models.

Apart from errors due to subgrid-modelling we have also errors introduced by the numerical scheme. Further improvement of a certain subgrid-model is only useful if the numerical errors are smaller than the subgrid-modelling errors. The question of the role of the numerical errors relative to the subgrid-modelling errors has insufficiently been answered in literature and is therefore addressed (chapter 6). The numerical errors are not determined by the numerical scheme only but also by the ratio Δ/h. In order to investigate the effect of numerical errors, we will compare LES for several numerical schemes and Δ/h-ratios.

The fifth question is which subgrid-terms in the energy equation are important and how they have to be modelled. Compressible LES does not require the modelling of the turbulent stress tensor only, but also the modelling of the subgrid-terms in the energy equation. It is expected that subgrid-terms in the energy equation are negligible at low Mach number, but become more important at higher Mach numbers. Furthermore, in recent studies of compressible LES not all relevant subgrid-terms in the energy equation have been taken into account. Models for these subgrid-terms will be formulated and tested in LES of the mixing layer at $M = 0.2$, 0.6 and 1.2 (chapter 7).

With respect to the second aim, the physical phenomena in the mixing layer at high Mach numbers, we will focus on two research questions. First, we will discuss the shocks that occur in the supersonic mixing layer at $M = 1.2$ (chapter 8). Shocks in numerical simulations of the three-dimensional mixing layer have not been observed before and only very limited experimental information is available. For this reason, we will study the physical nature and origin of these shocks. Furthermore, the numerical treatment of shocks in a turbulent flow is an important problem. The numerical scheme has to be able to accurately represent the turbulent motions and the shock-waves simultaneously. Both requirements are satisfied by the numerical scheme we present in chapter 8.

The reason of mixing layer growth rate reduction with increasing Mach number is the second question to be answered regarding the physical processes in

the compressible mixing layer (chapter 9). The assumption of dilatation dissipation due to shocks is essential in the explanations given in literature for the effect of Mach number on the growth rate. From a comparison of DNS at several Mach numbers, we will show that dilatation dissipation cannot cause the growth rate reduction. Furthermore, we will present a simple algebraic model based on pressure fluctuations, which is able to give quantitative predictions of the Mach number effect on the growth rate.

We finally summarize the contents of this thesis. The governing equations in DNS and LES and their numerical discretizations are formulated in chapter 2. In chapter 3 the subgrid-models for the turbulent stress tensor are presented. Realizability conditions for the turbulent stress tensor are derived in chapter 4. Actual tests of LES for the compressible mixing layer are conducted in chapters 5 to 7. In chapter 5 DNS and LES are performed for the mixing layer at $M = 0.2$ in order to test the subgrid-models for the turbulent stress tensor. The role of numerical errors is investigated in chapter 6. Compressible subgrid-modelling is the subject of chapter 7, where models for the subgrid-terms in the energy equation are formulated and tested for $M = 0.2$ and $M = 0.6$. The following two chapters concern physical phenomena in the compressible mixing layer. The shocks in DNS of the supersonic mixing layer at $M = 1.2$ are studied in chapter 8, whereas the effect of Mach number on the shear layer growth and the turbulent statistics is investigated in chapter 9. Conclusions and recommendations for future research are presented in chapter 10.

Chapter 2

Governing equations in DNS and LES

In the first section of this chapter the Navier-Stokes equations are presented. They describe the motion of compressible flow and are the governing equations in a DNS. LES employs the filtered Navier-Stokes equations, formulated in section 2. The modelling of the subgrid-terms in these equations is postponed until the following chapters. In section 3 the numerical techniques used in DNS and LES are presented, including a new fourth-order accurate scheme.

2.1 The Navier-Stokes equations

The Navier-Stokes equations, which represent conservation of mass, momentum and energy[1], read

$$\begin{aligned} \partial_t \rho + \partial_j(\rho u_j) &= 0, && (2.1)\\ \partial_t(\rho u_i) + \partial_j(\rho u_i u_j) + \partial_i p - \partial_j \sigma_{ij} &= 0 \quad (i = 1, 2, 3), && (2.2)\\ \partial_t e + \partial_j((e + p)u_j) - \partial_j(\sigma_{ij} u_i) + \partial_j q_j &= 0, && (2.3) \end{aligned}$$

where the symbols ∂_t and ∂_j denote the partial differential operators $\partial/\partial t$ and $\partial/\partial x_j$ respectively and the summation convention for repeated indices is used. The independent variables t and x_j represent time and the spatial coordinates, respectively. The velocity vector is denoted by $\mathbf{u}$, while ρ is the density and p the pressure. Moreover, e is the total energy density

$$e = E(\rho, \mathbf{u}, p) = \frac{p}{\gamma - 1} + \frac{1}{2}\rho u_i u_i. \tag{2.4}$$

[1] In contrast with many textbooks on fluid dynamics, where the momentum equation is called the Navier-Stokes equation, we call the set of conservation laws the Navier-Stokes equations.

The viscous stress tensor $\boldsymbol{\sigma}$ is based on the temperature T and velocity vector $\mathbf{u}$,

$$\sigma_{ij} = F_{ij}(\mathbf{u}, T) = \frac{\mu(T)}{Re} S_{ij}(\mathbf{u}) \quad (i, j = 1, 2, 3), \tag{2.5}$$

where

$$S_{ij}(\mathbf{u}) = \partial_j u_i + \partial_i u_j - \tfrac{2}{3}\delta_{ij}\partial_k u_k \quad (i, j = 1, 2, 3) \tag{2.6}$$

is the strain rate tensor. The tensor δ_{ij} is the Kronecker delta, defined as $\delta_{ij} = 1$ if $i = j$ and $\delta_{ij} = 0$ if $i \neq j$. For air the dynamic viscosity $\mu(T)$ is in good approximation given by Sutherland's law,

$$\mu(T) = T^{\frac{3}{2}} \frac{1 + C}{T + C}. \tag{2.7}$$

In addition $\mathbf{q}$ represents the heat flux vector, given by

$$q_j = Q_j(T) = -\frac{\mu(T)}{(\gamma - 1)RePrM^2} \partial_j T \quad (j = 1, 2, 3). \tag{2.8}$$

The temperature T is related to the density and the pressure by the ideal gas law

$$T = G(\rho, p) = \gamma M^2 \frac{p}{\rho}. \tag{2.9}$$

These equations have been made dimensionless by introducing a reference length L_R, velocity u_R, density ρ_R, temperature T_R and viscosity μ_R. In addition γ, the ratio of the specific heats C_P and C_V, and the Prandtl number Pr are given the values $\gamma = 1.4$ and $Pr = 1$, while we use $C = 0.4$, which corresponds to a reference temperature of $276K$. The values of the Reynolds number (1.1) and the reference Mach number

$$M = u_R / a_R, \tag{2.10}$$

where a_R is the reference value for the speed of sound, are given for each case separately. For the temporal mixing layer, L_R is half the initial vorticity thickness, whereas the other reference values are the upper stream values. Initial and boundary conditions for the mixing layer have been described in section 1.2.

The terms in the Navier-Stokes equations (2.1-2.3) contain the time derivative operator ∂_t or the spatial derivative operator ∂_j. With respect to the terms containing spatial derivatives, we distinguish between convective and viscous terms. Viscous terms are those containing the viscous stress tensor σ_{ij} or the heat-flux q_j, whereas the other terms are called convective.

filter	filter function $G(\mathbf{x}, \boldsymbol{\xi})$	Fourier transform $G^*(\mathbf{k})$
top-hat	$\begin{cases} \frac{1}{\Delta^3} & \text{if } \lvert x_i - \xi_i \rvert < \Delta_i/2, \\ 0 & \text{otherwise.} \end{cases}$	$\prod_{i=1}^{3} \frac{\sin(\Delta_i k_i/2)}{\Delta_i k_i/2}$
Gaussian	$(\frac{6}{\pi\Delta^2})^{\frac{3}{2}} e^{-6(\frac{(x_1-\xi_1)^2}{\Delta_1^2}+\frac{(x_2-\xi_2)^2}{\Delta_2^2}+\frac{(x_3-\xi_3)^2}{\Delta_3^2})}$	$e^{-(\Delta_1^2 k_1^2+\Delta_2^2 k_2^2+\Delta_3^2 k_3^2)/24}$
spectral cut-off	$\prod_{i=1}^{3} \frac{\sin(k_c(x_i-\xi_i))}{\pi(x_i-\xi_i)}$ with $k_c = \frac{\pi}{\Delta_i}$	$\begin{cases} 1 & \text{if } \lvert k_i \rvert < k_c, \\ 0 & \text{otherwise.} \end{cases}$

Table 2.1: Filter functions in physical and spectral space. The summation convention is not used.

2.2 The filtering approach

In the Large-Eddy Simulation of turbulent flow, any flow variable f is decomposed in a large-scale contribution $\overline{f}$ and a small-scale contribution f', i.e. $f = \overline{f} + f'$. The filtered part $\overline{f}$ is defined as follows:

$$\overline{f}(\mathbf{x}) = \int_\Omega G(\mathbf{x}, \boldsymbol{\xi}) f(\boldsymbol{\xi}) d\boldsymbol{\xi}, \tag{2.11}$$

where $\mathbf{x}$ and $\boldsymbol{\xi}$ are vectors in the flow domain Ω. The filter function G depends on the parameter Δ, called the filter width, and satisfies the condition

$$\int_\Omega G(\mathbf{x}, \boldsymbol{\xi}) d\boldsymbol{\xi} = 1 \tag{2.12}$$

for every $\mathbf{x}$ in Ω. For compressible flows, Favre (1986) introduced a related filter operation,

$$\tilde{f} = \frac{\overline{\rho f}}{\bar{\rho}}, \tag{2.13}$$

which leads to the decomposition $f = \tilde{f} + f''$.

Typical filters commonly used in Large-Eddy simulation, the top-hat, Gaussian and spectral cut-off filter, are listed in table 2.1. The symbol Δ_i denotes the filter width in the i-direction, whereas Δ is defined as

$$\Delta = (\Delta_1 \Delta_2 \Delta_3)^{1/3}. \tag{2.14}$$

For constant Δ_i, the filter functions in table 2.1 can be written as $G(\mathbf{x}-\boldsymbol{\xi})$. In this case the filter operation is a convolution integral. It is linear and commutes with partial derivatives (Geurts *et al.* 1994, Ghosal & Moin 1995). The corresponding Favre filter is also linear,but does not commute with partial derivatives. If the filter operation is a convolution integral, the filtering can be performed in spectral space as follows:

$$\bar{u}_i^*(\mathbf{k}) = G^*(\mathbf{k})u_i^*(\mathbf{k}), \tag{2.15}$$

where $\mathbf{k}$ is the wave vector, u_i^* and $\bar{u}_i^*$ are the Fourier transforms of u_i and $\bar{u}_i$, and G^* is the Fourier transform of G with respect to the vector $\mathbf{x}-\boldsymbol{\xi}$.

The filtered Navier-Stokes equations are valid when the 'bar-filter' is any linear operator that commutes with the partial differential operators ∂_t and ∂_j. These equations are obtained if the 'bar'-filter is applied to the Navier-Stokes equations and the filtered energy equation is rewritten (Vreman *et al.* 1995a):

$$\begin{aligned}
\partial_t\bar{\rho} + \partial_j(\bar{\rho}\tilde{u}_j) &= 0, && (2.16)\\
\partial_t(\bar{\rho}\tilde{u}_i) + \partial_j(\bar{\rho}\tilde{u}_i\tilde{u}_j) + \partial_i\bar{p} - \partial_j\breve{\sigma}_{ij} &= -\partial_j(\bar{\rho}\tau_{ij}) \\
&\quad +\partial_j(\bar{\sigma}_{ij} - \breve{\sigma}_{ij}), && (2.17)\\
\partial_t\breve{e} + \partial_j((\breve{e}+\bar{p})\tilde{u}_j) - \partial_j(\breve{\sigma}_{ij}\tilde{u}_i) + \partial_j\breve{q}_j &= -\alpha_1 - \alpha_2 - \alpha_3 + \alpha_4 \\
&\quad +\alpha_5 + \alpha_6. && (2.18)
\end{aligned}$$

The basic filtered flow variables are the filtered density $\bar{\rho}$, the filtered pressure $\bar{p}$ and the Favre filtered velocity vector $\tilde{\mathbf{u}}$. The filtered temperature is obtained Favre-filtering the ideal gas law,

$$\tilde{T} = G(\bar{\rho}, \bar{p}). \tag{2.19}$$

Other quantities are functions of these filtered variables,

$$\begin{aligned}
\breve{e} &= E(\bar{\rho}, \tilde{\mathbf{u}}, \bar{p}), && (2.20)\\
\breve{\sigma}_{ij} &= F_{ij}(\tilde{\mathbf{u}}, \tilde{T}), && (2.21)\\
\breve{q}_j &= Q_j(\tilde{T}). && (2.22)
\end{aligned}$$

We have written the equations (2.16-2.18) such that the left-hand sides are the Navier-Stokes equations (2.1-2.3) expressed in the filtered variables $\bar{\rho}$, $\tilde{u}_i$ and $\bar{p}$.

The right-hand sides of (2.16-2.18) contain the so-called subgrid-terms, which represent the effect of the unresolved scales. Unlike the terms at the left-hand sides, these terms cannot be expressed in the filtered flow variables. Since we use Favre filtered velocities, no subgrid-terms appear in the filtered continuity equation. The filtered momentum equation contains two subgrid-terms. The turbulent stress tensor,

$$\bar{\rho}\tau_{ij} = \overline{\rho u_i u_j} - \overline{\rho u}_i\overline{\rho u}_j/\overline{\rho} = \overline{\rho}(\widetilde{u_i u_j} - \tilde{u}_i\tilde{u}_j), \tag{2.23}$$

results from the nonlinearity of the convective term, whereas the second term in the filtered momentum equation results from the nonlinearity of the viscous term and the fact that the Favre filter and partial derivatives do not commute. The second term is always neglected in high Reynolds number flows. *A priori* tests confirm that it is an order of magnitude smaller than the first term (Vreman *et al.* 1995a; see also section 7.1).

The subgrid-terms in the energy equation are defined as:

$$\alpha_1 = \tilde{u}_i \partial_j(\bar{\rho}\tau_{ij}) \tag{2.24}$$

$$\alpha_2 = \partial_j(\overline{pu_j} - \bar{p}\tilde{u}_j)/(\gamma - 1), \tag{2.25}$$

$$\alpha_3 = \overline{p\partial_j u_j} - \bar{p}\partial_j \tilde{u}_j, \tag{2.26}$$

$$\alpha_4 = \overline{\sigma_{ij}\partial_j u_i} - \bar{\sigma}_{ij}\partial_j \tilde{u}_i \tag{2.27}$$

$$\alpha_5 = \partial_j(\bar{\sigma}_{ij}\tilde{u}_i - \breve{\sigma}_{ij}\tilde{u}_i) \tag{2.28}$$

$$\alpha_6 = \partial_j(\bar{q}_j - \breve{q}_j). \tag{2.29}$$

The term α_1 is the turbulent stress on the scalar level. It represents the kinetic energy transfer from resolved to subgrid scales. Furthermore, α_2 is the pressure-velocity subgrid-term, representing the effect of the subgrid turbulence on the conduction of heat in the resolved scales. The pressure-dilatation α_3 is purely a compressibility effect, since it vanishes if the flow is divergence free with constant density. The subgrid-scale turbulent dissipation rate α_4 is the amount subgrid kinetic energy converted into internal energy by viscous dissipation. The last two terms, α_5 and α_6, are created by the nonlinearities in the viscous stress and heat flux, respectively. Like $\partial_j(\bar{\sigma}_{ij} - \breve{\sigma}_{ij})$ in the momentum equations, these two terms are small compared to the other subgrid-terms (see section 7.1).

The filtered energy equation describes the evolution of $\breve{e}$, the resolved total energy, which is the sum of the filtered internal energy ($\bar{p}/(\gamma-1)$) and the resolved kinetic energy ($\frac{1}{2}\bar{\rho}\tilde{u}_i\tilde{u}_i$). The resolved kinetic energy equation is obtained by multiplication of (2.17) with $\tilde{u}_i$ and contains the subgrid-terms $-\alpha_1$ and $\tilde{u}_i\partial_j(\bar{\sigma}_{ij} - \breve{\sigma}_{ij})$. Hence, the filtered internal energy equation, obtained by subtracting the resolved kinetic energy equation from (2.18) does not contain α_1, while α_5 is modified.

The subgrid-terms contain information from the unfiltered field. Subgrid-models have to be included for these terms in order to express the filtered Navier-Stokes equations in filtered variables only. The turbulent stress tensor τ_{ij} is the only subgrid-term in incompressible flow. For this reason, we expect that compressible LES at low Mach numbers primarily requires the modelling of τ_{ij}. The modelling of this tensor and related aspects are addressed in chapters 3-6. We expect the subgrid-terms in the energy equation to become more important if the Mach number is increased. The modelling of these terms is addressed in chapter 7.

	convective terms		viscous terms	
A	D_1	weighted second-order	D_2	second-order
A'	D_1'	second-order	D_2	second-order
B	D_3	weighted fourth-order	D_2	second-order
B'	D_3'	fourth-order	D_2	second-order
C	D_4	spectral	D_4	spectral
D	D_5	third-order upwind	D_2	second-order

Table 2.2: The numerical methods A, A', B, B', C and D.

2.3 Numerical schemes

In this section we present the numerical algorithms used to solve the Navier-Stokes equations (in DNS) and the filtered Navier-Stokes equations (in LES). The equations are discretized on a uniform rectangular grid and the grid size in the x_i-direction is denoted by h_i. In DNS, all relevant scales present in the turbulent flow have to be represented on the grid, consequently, the grid size in DNS is determined by the smallest turbulent length scale, the Kolmogorov dissipation scale. The smallest resolved scale in LES is the filter width Δ, which determines the grid size. Usually h_i is chosen equal to Δ_i or $\frac{1}{2}\Delta_i$. The optimal choice of the ratio Δ_i/h_i will be discussed in chapter 6. In the following we turn to the discretization of the temporal and spatial derivatives respectively.

The time stepping method which we adopt is an explicit four-stage compact-storage Runge-Kutta method. When we consider the scalar differential equation $du/dt = f(u)$, this Runge-Kutta method performs within one time step δt,

$$u^{(j)} = u^{(0)} + \beta_j \delta t f(u^{(j-1)}), \quad (j = 1, 2, 3, 4) \tag{2.30}$$

with $u^{(0)} = u(t)$ and $u(t + \delta t) = u^{(4)}$. With the coefficients $\beta_1 = 1/4$, $\beta_2 = 1/3$, $\beta_3 = 1/2$ and $\beta_4 = 1$ this yields a second-order accurate time integration method (Jameson 1983). In Large-Eddy Simulations with explicit methods truncation errors resulting from the spatial discretization method appear to be more important than truncation errors resulting from the discretization in time. The reason is that the time step determined by the stability restriction of the numerical scheme is considerably smaller than the shortest turbulent time-scale, which is the turn-over time of eddies of the size Δ.

Table 2.2 presents six different methods for the discretization of the spatial derivatives. The table distinguishes between convective and viscous terms. The operators D_j in the table refer to the numerical approximation of the ∂_1-operator for the corresponding method. The ∂_2 and ∂_3-operators are treated by analogy to

the ∂_1-operator. Subgrid-terms are discretized with the same order of accuracy as the viscous terms. In particular the divergences of the turbulent stress tensor are approximated with the discretization method for the divergences of the viscous stress tensor. In the following the methods A, A', B, B',C and D are described in more detail for uniform grids.

Method A is a robust second-order finite volume method, which can easily be formulated for non-uniform grids as well (Kuerten *et al.* 1993). The discretization for the convective terms is the cell vertex trapezoidal rule, which is a weighted second-order central difference. In vertex (i, j, k) the corresponding operator D_1 for a function f is defined as

$$\begin{aligned} (D_1 f)_{i,j,k} &= (s_{i+1,j,k} - s_{i-1,j,k})/(2h_1) \\ \text{with} \quad s_{i,j,k} &= (g_{i,j-1,k} + 2g_{i,j,k} + g_{i,j+1,k})/4 \\ \text{with} \quad g_{i,j,k} &= (f_{i,j,k-1} + 2f_{i,j,k} + f_{i,j,k+1})/4. \end{aligned} \tag{2.31}$$

The viscous terms contain second-order derivatives. In method A the viscous stress tensor σ_{ij} and heat flux q_j are calculated in centres of cells. In centre $(i + \frac{1}{2}, j + \frac{1}{2}, k + \frac{1}{2})$ the corresponding discretization $D_2 f$ has the form

$$\begin{aligned} (D_2 f)_{i+\frac{1}{2},j+\frac{1}{2},k+\frac{1}{2}} &= (s_{i+1,j+\frac{1}{2},k+\frac{1}{2}} - s_{i,j+\frac{1}{2},k+\frac{1}{2}})/h_1 \\ \text{with} \quad s_{i,j+\frac{1}{2},k+\frac{1}{2}} &= (f_{i,j,k} + f_{i,j+1,k} + f_{i,j,k+1} + f_{i,j+1,k+1})/4. \end{aligned} \tag{2.32}$$

The divergences of the viscous stress tensor and heat flux are subsequently calculated with the same discretization rule applied to control volumes centred around vertices (i, j, k). Method A is robust with respect to odd-even decoupling. This is illustrated if we consider a function f with $f_{i+1,j,k} = -f_{i,j,k}$, called a π-wave (or $2h$-wave) in the x_1-direction. The scheme for the viscous terms as described above dissipates such π-waves. Moreover, the discretization of the convective terms with D_1 is such that π-waves in the x_2- and x_3-directions do not appear in $D_1 f$. The standard second-order central difference (labelled as D_1') is obtained if s in equation (2.31) is replaced by f. In that case π-waves in the x_2- and x_3-directions persist in $D_1 f$. This argument illuminates why this finite volume method is more robust than the standard second-order central difference and why no artificial dissipation is needed to prevent numerical instability in the present application. In method A' the discretization for the convective terms is the standard second-order central difference, whereas the viscous terms are discretized as in method A.

Using this knowledge we constructed a new fourth-order accurate method which is more robust than the standard five-point fourth-order discretization. Method B employs this discretization for the convective terms, while the viscous

terms are still treated as in method A. The corresponding expression for $D_3 f$ has the following form:

$$\begin{aligned} (D_3 f)_{i,j,k} &= (-s_{i+2,j,k} + 8s_{i+1,j,k} - 8s_{i-1,j,k} + s_{i-2,j,k})/(12h_1) \qquad (2.33) \\ \text{with} \quad s_{i,j,k} &= (-g_{i,j-2,k} + 4g_{i,j-1,k} + 10g_{i,j,k} + 4g_{i,j+1,k} - g_{i,j+2,k})/16 \\ \text{with} \quad g_{i,j,k} &= (-f_{i,j,k-2} + 4f_{i,j,k-1} + 10f_{i,j,k} + 4f_{i,j,k+1} - f_{i,j,k+2})/16. \end{aligned}$$

This scheme is conservative, since it is a weighted central difference. The coefficients in the definition for $g_{i,j,k}$ are chosen such that $g_{i,j,k}$ is a fourth order accurate approximation to $f_{i,j,k}$ and π-waves in the x_3-direction give no contributions to $g_{i,j,k}$. The definition for $s_{i,j,k}$ has the same properties with respect to the x_2-direction. Consequently, this method is more robust with respect to odd-even decoupling than the standard five-points fourth-order central difference (labelled as D_3'), which is recovered if s in equation (2.33) is replaced by f. The latter discretization is used for the convective term in method B', whereas the viscous terms in B' are discretized as in method B. For convenience, we refer to methods B and B' as fourth-order methods, but we remark that the formal spatial accuracy of the scheme is only second-order due to the treatment of the viscous terms. However, since the instabilities in the mixing layer are *convective* instabilities, the convective terms play a more important role than the viscous terms, and, for this reason it is expected that a more accurate treatment of only the convective terms is sufficient in order to obtain a more accurate method. Another example of numerical simulations in which the convective terms are treated with a fourth-order, while the viscous terms are treated with a second-order accurate scheme, is found in Normand & Lesieur (1992).

Method C is a pseudo-spectral scheme for the convective and viscous terms. Derivatives in the periodic x_1- and x_3-directions are evaluated using discrete Fourier-transforms. Free-slip boundaries are imposed in the x_2-direction, which implies that a flow variable is symmetric or anti-symmetric at these boundaries. To evaluate derivatives in the x_2-direction, discrete cosine and sine expansions are employed for the symmetric ($\bar{\rho}$, $\tilde{u}_1$, $\tilde{u}_3$, $\breve{e}$) and anti-symmetric variables ($\tilde{u}_2$), respectively. This spectral method does not dissipate π-waves, which leads to contributions to the so-called 'odd ball' wavenumber. As in Sandham & Reynolds (1989), the odd ball component (π-wave) is explicitly removed at each stage within a time step to prevent numerical instability.

Finally, method D is a shock-capturing method to be used in supersonic flow calculations (chapter 8). The convective terms are discretized with the third-order accurate MUSCL-scheme, fully described by Van der Burg (1993), whereas the viscous terms are treated with the second-order scheme described above.

Chapter 3

Subgrid-models for the turbulent stress tensor

The turbulent stress tensor τ_{ij} is the most important subgrid-term in LES. Much effort has been put into the development of good subgrid-models (Moin & Jimenez 1993) and, consequently, a large number of subgrid-models exist. In this chapter we consider six subgrid-models for this tensor: the Smagorinsky model (Smagorinsky 1963), the similarity model (Bardina *et al.* 1984; Liu *et al.* 1994), the gradient model (Clark *et al.* 1979; Liu *et al.* 1994), the dynamic eddy-viscosity model (Germano 1992), the dynamic mixed model (Zang *et al.* 1993; Vreman *et al.* 1994b) and the dynamic Clark model (Vreman *et al.* 1995c). These models are important representatives of the available subgrid-models, although we have restricted this study to models which do not require the solution of an additional differential equation (Moin & Jimenez 1993).

The first two sections of this chapter[1] contain the formulations of these six subgrid-models and the third section is devoted to a problem caused by one of the models. The Smagorinsky, similarity and gradient models, to be called basic models, are formulated in section 1. The dynamic procedure is explained in section 2. The procedure is based on the Germano identity, which is a relation between turbulent stresses at different filter levels. Section 2 presents a generalised Germano identity, applicable to arbitrary nonlinear functions. Furthermore, we formulate the three dynamic models, formed from the basic models in combination with the dynamic procedure introduced by Germano (1992). In this section we also report and present a solution to a specific problem which arises if top-hat filters are used in the dynamic procedure. Section 3 is devoted to a theoretical analysis of the gradient model, since actual simulations indicate that this model has bad stability properties. The nature of the instability is explained from this analysis,

[1] This chapter is based on the papers Vreman *et al.* 1994bf and 1995c.

which is performed for a model equation in one dimension. The conclusions are summarized in section 4.

3.1 Basic models

In this section we present three models for the turbulent stress tensor $\bar{\rho}\tau_{ij}$: the Smagorinsky, similarity and gradient model. The Smagorinsky model is an eddy-viscosity model, unlike the similarity and gradient model. In each case the model is denoted by m_{ij}.

3.1.1 The Smagorinsky model

The first model is the well-known Smagorinsky model (Smagorinsky 1963; Rogallo & Moin 1984), given by

$$m_{ij} = -\bar{\rho}C_S^2\Delta^2|S(\tilde{\mathbf{u}})|S_{ij}(\tilde{\mathbf{u}}) \quad \text{with} \quad |S(\tilde{\mathbf{u}})|^2 = \tfrac{1}{2}S_{ij}(\tilde{\mathbf{u}})S_{ij}(\tilde{\mathbf{u}}), \tag{3.1}$$

where S_{ij} is the strain rate defined by equation (2.6). With respect to the Smagorinsky constant C_S several values have been proposed: e.g. 0.2 in isotropic turbulence (Deardorff 1971) and 0.1 in turbulent channel flow (Deardorff 1970). With the use of power laws for the shape of the energy spectrum, Schumann (1991) suggests $C_S = 0.17$. This eddy-viscosity model formally models the anisotropic part of the tensor τ_{ij} only, which is defined as:

$$\bar{\rho}\tau_{ij}^a = \bar{\rho}\tau_{ij} - \tfrac{2}{3}\bar{\rho}k, \tag{3.2}$$

with $k = \frac{1}{2}\tau_{ii}$. The isotropic part of the tensor is usually not modelled, but incorporated in the filtered pressure. This issue will be further addressed in chapter 4. The major short-coming of the Smagorinsky model is its excessive dissipation in laminar regions with mean shear, because S_{ij} is large in regions with mean shear (Germano *et al.* 1991). Furthermore, the correlation between the Smagorinsky model and the actual turbulent stress is quite low (about 0.3 in several flows). The similarity and gradient model, described below, do not suffer from excessive dissipation in laminar regimes and correlate much better with the actual turbulent stress (0.6 to 0.9 in several flows (Liu *et al.* 1994, Vreman *et al.* 1995a)).

3.1.2 The similarity model

The similarity model, formulated by Bardina *et al.* (1984) and revisited by Liu *et al.* (1994), is not of the eddy-viscosity type. It is based on the assumption that the velocities at different levels give rise to turbulent stresses with similar

structures. More specifically, the definition of $\overline{\rho}\tau_{ij}$ in terms of the unfiltered variables ρ and ρu_i is applied to the filtered variables $\overline{\rho}$ and $\overline{\rho u}_i$. Thus a tensor m_{ij} is defined,

$$m_{ij} = \overline{\overline{\rho u}_i \overline{\rho u}_j / \overline{\rho}} - \overline{\overline{\rho u}_i} \overline{\overline{\rho u}}_j / \overline{\overline{\rho}} = \overline{\overline{\rho}\tilde{u}_i \tilde{u}_j} - \overline{\overline{\rho}\tilde{u}_i} \overline{\overline{\rho}\tilde{u}}_j / \overline{\overline{\rho}}, \tag{3.3}$$

which is used as a model for $\overline{\rho}\tau_{ij}$. In contrast to $\overline{\rho}\tau_{ij}$, the tensor m_{ij} can be calculated in a Large-Eddy Simulation, since it is fully expressed in the filtered variables.

The correlation between the similarity model and the exact turbulent stress is relatively high. This indicates that the similarity model predicts important structures of the turbulent stress at the right locations. However, the magnitude of the turbulent stress is less accurately predicted. The definition of the similarity model implies that the model only takes into account the contribution of the filtered variables to the turbulent stress. Therefore, the similarity model does generally not overestimate the turbulent stress, but rather underestimates them, in particular in the turbulent regime. Hence, in laminar regions this model is not expected to be too dissipative, unlike the Smagorinsky model. In turbulent regions, however, the dissipation of small scales by the similarity model may be insufficient.

3.1.3 The gradient model

In the following we will derive the gradient model m_{ij} for $\bar{\rho}\tau_{ij}$ using Taylor expansions of the filtered velocity. Our procedure is slightly different from the procedure followed by Clark *et al.* (1979). Clark *et al.* decompose the turbulent stress into three parts, the so-called Leonard, cross and Reynolds components, and apply the expansions to each component separately. We directly apply the expansion to the total turbulent stress. Furthermore, we present the formulation for the compressible turbulent stress tensor, thus generalizing the derivation by Clark *et al.*.

For the top-hat filter $\bar{f}$ is defined as:

$$\overline{f}(\mathbf{x}) = \frac{1}{\Delta_1 \Delta_2 \Delta_3} \int_{-\frac{1}{2}\Delta_3}^{\frac{1}{2}\Delta_3} \int_{-\frac{1}{2}\Delta_2}^{\frac{1}{2}\Delta_2} \int_{-\frac{1}{2}\Delta_1}^{\frac{1}{2}\Delta_1} f(\mathbf{x}+\mathbf{y}) d\mathbf{y}. \tag{3.4}$$

The function $f(\mathbf{x}+\mathbf{y})$ is expanded as a Taylor series around $\mathbf{x}$, and after evaluation of the integral we obtain:

$$\overline{f} = f + \tfrac{1}{24}\Delta_k^2 \partial_k^2 f + \mathcal{O}(\Delta^4). \tag{3.5}$$

The same formula holds for Gaussian filters (Love 1980). We use this formula to rewrite the turbulent stress tensor:

$$\begin{aligned}
\overline{\rho}\tau_{ij} &= \overline{\rho u_i u_j} - \overline{\rho u}_i \overline{\rho u}_j / \overline{\rho} \\
&= \rho u_i u_j + \tfrac{1}{24}\Delta_k^2 \partial_k^2 (\rho u_i u_j) \\
&\quad -(\rho u_i + \tfrac{1}{24}\Delta_k^2 \partial_k^2 (\rho u_i))(\rho u_j + \tfrac{1}{24}\Delta_k^2 \partial_k^2 (\rho u_j))/(\rho + \tfrac{1}{24}\Delta_k^2 \partial_k^2 \rho) \\
&\quad +\mathcal{O}(\Delta^4) \\
&= \tfrac{1}{12}\Delta_k^2 \rho (\partial_k u_i)(\partial_k u_j) + \mathcal{O}(\Delta^4), \qquad (3.6)
\end{aligned}$$

where we used the relation

$$1/(\rho + \tfrac{1}{24}\Delta_k^2 \partial_k^2 \rho) = \frac{1}{\rho} - \frac{1}{24\rho^2}\Delta_k^2 \partial_k^2 \rho + \mathcal{O}(\Delta^4). \qquad (3.7)$$

The next step is to express equation (3.6) into filtered variables. Using equation (3.7), the Favre-filtered velocity can be written as

$$\begin{aligned}
\tilde{u}_i &= \overline{\rho u}_i / \overline{\rho} \\
&= (\rho u_i + \tfrac{1}{24}\Delta_k^2 \partial_k^2 (\rho u_i))/(\rho + \tfrac{1}{24}\Delta_k^2 \partial_k^2 \rho) + \mathcal{O}(\Delta^4) \\
&= u_i + \tfrac{1}{24}\Delta_k^2 \partial_k^2 u_i + \frac{1}{12\rho}\Delta_k^2 (\partial_k \rho)(\partial_k u_i) + \mathcal{O}(\Delta^4) \qquad (3.8)
\end{aligned}$$

We observe that for both the bar- and Favre filter, unfiltered and filtered variables differ by a term of the order $\mathcal{O}(\Delta^2)$:

$$\rho = \overline{\rho} + \mathcal{O}(\Delta^2), \qquad (3.9)$$

$$u_i = \tilde{u}_i + \mathcal{O}(\Delta^2). \qquad (3.10)$$

Substituting expressions (3.9) and (3.10) into (3.6) yields:

$$\overline{\rho}\tau_{ij} = \tfrac{1}{12}\Delta_k^2 \overline{\rho} (\partial_k \tilde{u}_i)(\partial_k \tilde{u}_j) + \mathcal{O}(\Delta^4). \qquad (3.11)$$

The first term on the right-hand side is referred to as the 'gradient' model,

$$m_{ij} = \tfrac{1}{12}\Delta_k^2 \overline{\rho} (\partial_k \tilde{u}_i)(\partial_k \tilde{u}_j). \qquad (3.12)$$

Observe that the expansion is mathematically correct provided the variables can be differentiated sufficiently often, but for rapidly fluctuating variables the $\mathcal{O}(\Delta^4)$ term may not be small. The gradient model can also be derived by not expanding the turbulent stress itself, but the similarity model of the turbulent stress (Vreman *et al.* 1995c). In the latter derivation only Taylor expansions of the *filtered* quantities $\overline{\rho}$ and $\widetilde{u}_i$ are employed, which are varying more smoothly over lengths of $\mathcal{O}(\Delta)$ than the *unfiltered* variables used in (3.6).

Simulations with the gradient model appear to be unstable and grid-refinement with respect to time or space does not prevent, but rather stimulate the growth of the instability (Vreman *et al.* 1995c). The character of this instability is analysed in section 3.3. To overcome this instability, the model can be supplied with a 'limiter' which prevents energy backscatter (Liu *et al.* 1994). A simple procedure for such a limiter is to represent the turbulent stress τ_{ij} in the filtered equations by cm_{ij}, i.e. the gradient model multiplied with a function c, which is given by:

$$c = \begin{cases} 1 & \text{if } m_{ij}\partial_j \tilde{u}_i \leq 0 \\ 0 & \text{otherwise.} \end{cases} \tag{3.13}$$

After this substitution the subgrid-model is ensured to dissipate kinetic energy of the resolved scales to subgrid scales. The simulation with the gradient model performed in chapter 5 adopts such a limiter, but unfortunately turns out to be relatively inaccurate.

Another way to overcome the instability is to add an eddy-viscosity model to the gradient model. Since Clark *et al.* (1979) added the Smagorinsky eddy-viscosity, the sum of the gradient and Smagorinsky model is called the Clark model. The Smagorinsky part in the Clark model is thus considered to act as a model for the rest-term in (3.11). However, like the Smagorinsky model itself, the Clark model is excessively dissipative in the transitional regime.

Hence, to stabilize the gradient model with either a limiter or the Smagorinsky model leads to inaccurate simulations. A better way to stabilize the gradient model is provided by the dynamic procedure, which yields the dynamic Clark model, to be presented in the next section.

3.2 Dynamic models

Three dynamic models for the turbulent stress tensor $\bar{\rho}\tau_{ij}$ will be presented: the dynamic eddy-viscosity, dynamic mixed and dynamic Clark model. The dynamic eddy-viscosity model (Germano 1992) is the Smagorinsky model in which the model constant is replaced by a coefficient which depends on the local turbulent structure of the flow. The dynamic eddy-viscosity model overcomes several shortcomings of the Smagorinsky model, e.g. the excessive dissipation in laminar regions. The local value of the coefficient is obtained by substitution of the Smagorinsky model into the Germano identity, which is a relation between the turbulent stress tensor at several filter levels. The dynamic eddy-viscosity model has been successfully applied to LES of transitional channel flow (Germano *et al.* 1991) and to a number of other flows as well (Moin & Jimenez 1993).

In this section we present a generalised form of the Germano identity for a subgrid-term resulting from the filtering of an arbitrary nonlinear function. In

addition to the formulation of the dynamic eddy-viscosity model, we formulate the dynamic mixed and dynamic Clark model, in which the dynamic procedure is applied to the mixed and Clark model respectively. The mixed model is the sum of the similarity and Smagorinsky model, whereas the Clark model is the sum of the gradient and Smagorinsky model. The mixed and Clark model suffer from similar short-comings as the Smagorinsky model itself. These short-comings can be removed by applying the dynamic procedure.

3.2.1 The generalised Germano identity

We define the subgrid-term corresponding to an arbitrary nonlinear function or operator $f(\mathbf{w})$, where $\mathbf{w}$ is a vector function of space and time, as follows:

$$\tau_f = \overline{f(\mathbf{w})} - f(\overline{\mathbf{w}}). \tag{3.14}$$

We call τ_f the subgrid-term on the F-level, where the bar denotes the basic filter operation. Apart from the grid-filter level (F-level), denoted by the bar-filter corresponding with the filter width Δ, Germano (1992) introduced a test-filter (at the G-level), which is denoted by the hat $\widehat{(\cdot)}$ and corresponds with the filter width 2Δ. The consecutive application of these two filters, resulting in e.g. $\widehat{\overline{\rho}}$, defines a filter on the 'FG-level' with which a filter width $\kappa\Delta$ can be associated. The value of κ equals 2 for the spectral cut-off filter (Germano 1991) and $\sqrt{5}$ for Gaussian filters (Germano 1992). For spectral cut-off and Gaussian filters, κ can be determined exactly, since the consecutive application of two of these filters yields a filter function of the same type. However, the consecutive application of two top-hat filters does not yield a top-hat filter. For top-hat filters an optimal value $\kappa = \sqrt{5}$ can be derived as shown in the next section. The subgrid-term on the FG-level reads

$$T_f = \widehat{\overline{f(\mathbf{w})}} - f(\widehat{\overline{\mathbf{w}}}) \tag{3.15}$$

The following identity can be derived between the subgrid-terms at the FG- and the F-level

$$T_f - \widehat{\tau_f} = L_f, \tag{3.16}$$

where the right-hand side L_f can be explicitly calculated from the variable $\bar{\mathbf{w}}$ on the F-level,

$$L_f = \widehat{f(\overline{\mathbf{w}})} - f(\widehat{\overline{\mathbf{w}}}). \tag{3.17}$$

The terms at the left-hand side of the generalised Germano identity (3.16) cannot be calculated from the variables on the F-level.

This generalised identity reduces to the Germano identity for the turbulent stress tensor in the case

$$f(\mathbf{w}) = \rho u_i u_j \qquad \text{with} \qquad \mathbf{w} = (\rho, \mathbf{u}). \tag{3.18}$$

In this case identity (3.16) is equivalent to

$$\widehat{\overline{\rho}}T_{ij} - \widehat{\overline{\rho}\tau_{ij}} = L_{ij}, \tag{3.19}$$

where τ_{ij} is the turbulent stress tensor and the other terms are given by

$$\widehat{\overline{\rho}}T_{ij} = \widehat{\overline{\rho u_i u_j}} - \widehat{\overline{\rho u}}_i\widehat{\overline{\rho u}}_j/\widehat{\overline{\rho}}, \tag{3.20}$$

$$L_{ij} = (\overline{\rho u}_i\overline{\rho u}_j/\overline{\rho})\widehat{\ } - \widehat{\overline{\rho u}}_i\widehat{\overline{\rho u}}_j/\widehat{\overline{\rho}}. \tag{3.21}$$

The notation $(.)\widehat{\ }$ indicates that the hat-filter is applied to the expression between the brackets. It is used in conjunction with the identically defined notation $\widehat{(.)}$ for convenience in the exposure. The terms at the left-hand side of the Germano identity (3.19) are the turbulent stress tensor on the FG-level and the turbulent stress tensor on the F-level filtered with the test-filter, respectively. The tensor L_{ij} can explicitly be calculated from the variables on the F-level, ρ and $\overline{\rho\mathbf{u}}$. The three dynamic models for the turbulent stress tensor in the following are obtained by substituting the corresponding base models into the Germano identity.

3.2.2 The dynamic eddy-viscosity model

The dynamic eddy-viscosity model (Germano 1992) adopts Smagorinsky's eddy-viscosity formulation, but the square of the Smagorinsky constant C_S is replaced by a coefficient C_d:

$$m_{ij} = -\bar{\rho}C_d\Delta^2|S(\tilde{\mathbf{u}})|S_{ij}(\tilde{\mathbf{u}}). \tag{3.22}$$

The coefficient C_d is dynamically adjusted to the local structure of the flow in the following way. The subgrid-model (3.22) is substituted into the Germano identity, which means that expressions for T_{ij} and τ_{ij} are obtained by formulating the subgrid-model in FG-filtered quantities and F-filtered quantities, respectively. This yields

$$C_d M_{ij} = L_{ij}, \tag{3.23}$$

with

$$M_{ij} = -\widehat{\overline{\rho}}(\kappa\Delta)^2|S(\mathbf{v})|S_{ij}(\mathbf{v}) + (\overline{\rho}\Delta^2|S(\tilde{\mathbf{u}})|S_{ij}(\tilde{\mathbf{u}}))\widehat{\ }. \tag{3.24}$$

The symbol $S_{ij}(\mathbf{v})$ represents the strain rate based on the Favre-filtered velocity on the FG-level ($v_i = \widehat{\overline{\rho u}}_i/\widehat{\overline{\rho}}$) and $|S(\mathbf{v})|^2 = \frac{1}{2}S_{ij}^2(\mathbf{v})$.

The symmetric tensor equation (3.23) represents a system of six equations for the single unknown C_d. Hence, a least square approach (Lilly 1992) is followed to calculate the model coefficient,

$$C_d = \frac{< M_{ij}L_{ij} >}{< M_{ij}M_{ij} >}. \tag{3.25}$$

Notice that m_{ij} formally models the anisotropic part of the turbulent stress. Therefore the model should be substituted in the anisotropic part of the Germano identity. However, substitution in the anisotropic part of the identity leads to the same coefficient C_d, since $M_{ij}L_{ij} = M_{ij}L^a_{ij}$. In order to prevent numerical instability caused by negative values of C_d, the numerator and denominator in equation (3.25) are averaged over the homogeneous directions, which is expressed by the symbol $< . >$. Furthermore, the model coefficient C_d is artificially set to zero at locations where the right-hand side of (3.25) returns negative values. One assumption of the formulation above is that variations of C_d on the scale of the test-filter are small. An alternative formulation which does not require this assumption has been proposed by Piomelli & Liu (1994). Some Large-Eddy Simulations in this thesis have been repeated using this formulation, but no significant differences were found.

3.2.3 The dynamic mixed model

The relatively accurate representation of the turbulent stress by the similarity model and a proper dissipation provided by the dynamic eddy-viscosity concept are combined in the dynamic mixed model. This model has been introduced by Zang *et al.* (1993), and modified by Vreman *et al.* (1994b) in order to remove a mathematical inconsistency. The dynamic mixed model employs the sum of the similarity and Smagorinsky eddy-viscosity model as base model:

$$m_{ij} = \overline{\overline{\rho u}_i \overline{\rho u}_j / \overline{\rho}} - \overline{\overline{\rho u}}_i \overline{\overline{\rho u}}_j / \overline{\overline{\rho}} - \overline{\rho} C_d \Delta^2 |S(\tilde{\mathbf{u}})| S_{ij}(\tilde{\mathbf{u}}). \tag{3.26}$$

The dynamic model coefficient C_d is obtained by substitution of this model into the Germano identity, which yields:

$$H_{ij} + C_d M_{ij} = L_{ij}, \tag{3.27}$$

where the tensors L_{ij} and M_{ij} are defined by equations (3.21) and (3.24) and the tensor H_{ij} is defined as

$$H_{ij} = \widehat{\overline{\widehat{\rho u}_i \widehat{\rho u}_j / \widehat{\rho}}} - \frac{\widehat{\widehat{\rho u}}_i \widehat{\widehat{\rho u}}_j}{\widehat{\widehat{\rho}}} - (\overline{\overline{\rho u}_i \overline{\rho u}_j / \overline{\rho}} - \overline{\overline{\rho u}}_i \overline{\overline{\rho u}}_j / \overline{\overline{\rho}})\widehat{\ }. \tag{3.28}$$

The differences between the formulation proposed by Zang *et al.* and Vreman *et al.* are related to different formulations for the model representing T_{ij}. Zang *et al.* express this term using velocities on the F-level, while Vreman *et al.* express this term using velocities on the FG-level. The latter approach is mathematically consistent with the definition of T_{ij} and was observed to yield improved results (Vreman *et al.* 1994b). By analogy with the formulation of the dynamic eddy-viscosity model, the dynamic model coefficient is obtained with the least square

approach:

$$C_d = \frac{< M_{ij}(L_{ij} - H_{ij}) >}{< M_{ij} M_{ij} >}, \tag{3.29}$$

which completes the formulation of the dynamic mixed model.

3.2.4 The dynamic Clark model

In section 3.1.3 we discussed two problems caused by the original Clark model. If the Smagorinsky eddy-viscosity is used, the model is too dissipative. However, if the eddy-viscosity part is omitted, the simulation becomes unstable. As indicated by the analysis in the next section, this instability is caused by the model, not by the numerical method, and can be overcome by sufficient dissipation. The dynamic procedure provides a solution for both problems.

Hence, the dynamic Clark model (Vreman *et al.* 1995c) employs the Clark model as base model:

$$m_{ij} = \tfrac{1}{12}\Delta_k^2 \overline{\rho}(\partial_k \tilde{u}_i)(\partial_k \tilde{u}_j) - \overline{\rho} C_d \Delta^2 |S(\tilde{\mathbf{u}})| S_{ij}(\tilde{\mathbf{u}}). \tag{3.30}$$

The formulation is similar to the formulation of the dynamic mixed model, the only difference being the 'gradient' part, which replaces the similarity part of the dynamic mixed model. Substitution of the dynamic Clark model into the Germano identity yields equation (3.27). In this case, however, the tensor H_{ij} expresses the difference of the gradient model on the FG-level and the F-level:

$$H_{ij} = \tfrac{1}{12}(\kappa\Delta_k)^2 \widehat{\overline{\rho}} \partial_k v_i \partial_k v_j - (\tfrac{1}{12}\Delta_k^2 \overline{\rho} \partial_k \tilde{u}_i \partial_k \tilde{u}_j)\widehat{\ }. \tag{3.31}$$

The dynamic model coefficient C_d is obtained with the right-hand side of expression (3.29).

With respect to computational efficiency the dynamic Clark model does not require much more work than the dynamic eddy-viscosity model, unlike the dynamic mixed model. The derivatives of the filtered velocity are already calculated in order to obtain the strain rate at different filter levels. The extra work needed is mainly due to the six filterings in equation (3.31) indicated by $(.)\widehat{\ }$. The formulation of H_{ij} for the dynamic mixed model, however, contains much more filtering operations, required for the evaluation of the similarity model at different levels. Consequently, the computational cost for the dynamic mixed model is considerably higher than for the dynamic eddy-viscosity and dynamic Clark model.

3.2.5 The top-hat filter in the dynamic procedure

The dynamic procedure requires formulations of the subgrid-model at the F-level and the FG-level. The F-level is associated with the filter width Δ, the G-level

with the filter width 2Δ and the FG-level with the filter width $\kappa\Delta$. In this subsection we argue that in conjunction with top-hat filters the value of κ should not be 2 (as used for instance by Zang *et al.* (1993)), but rather $\sqrt{5}$.

We denote the original filter function by G_a with filter width $a = \Delta$ and the test-filter function by G_b with filter width $b > a$. The filter function corresponding to the consecutive application of these two filters is denoted by H and satisfies the following formula:

$$H(\mathbf{y}) = \int_\Omega G_b(\mathbf{y} - \mathbf{z}) G_a(\mathbf{z}) d\mathbf{z}. \tag{3.32}$$

If G_a and G_b are spectral filters, H is a spectral filter as well with filter width b, whereas if G_a and G_b are Gaussian filters, H is a Gaussian filter with filter width $\sqrt{a^2 + b^2}$. However, the consecutive application of two top-hat filters is not a top-hat filter; the filter function H has a trapezoidal shape. In Large-Eddy Simulations employing the dynamical procedure with top-hat filters, the filter width of H is usually assumed to be the same as the filter width of G_b (Zang *et al.* 1993). However, this approximation cannot be very good, because the H-filter will certainly render smoother signals than the G_b-filter, so the filter width associated with H should be larger than b. We proceed to show how an appropriate value for the filter width of H can be found. Since the three-dimensional filter function is usually a product of three one-dimensional filter functions, the analysis can be performed in one dimension. Suppose that H is the trapezoidal filter function resulting from the consecutive application of two one-dimensional top-hat filter functions G_a and G_b with $b > a$. This yields the following expression:

$$H(y) = \begin{cases} \frac{1}{ab}(y + \frac{1}{2}(b+a)) & \text{if } -\frac{1}{2}(b+a) < y < -\frac{1}{2}(b-a), \\ \frac{1}{b} & \text{if } -\frac{1}{2}(b-a) \le y \le \frac{1}{2}(b-a), \\ -\frac{1}{ab}(y - \frac{1}{2}(b+a)) & \text{if } \frac{1}{2}(b-a) < y < \frac{1}{2}(b+a), \\ 0 & \text{if } |y| \ge \frac{1}{2}(b+a)\ . \end{cases} \tag{3.33}$$

We next find an optimal approximation of H by a top-hat filter function G_c, given by

$$G_c(y) = \begin{cases} \frac{1}{c} & \text{if } -\frac{1}{2}c < y < \frac{1}{2}c, \\ 0 & \text{if } |y| \ge \frac{1}{2}c\ . \end{cases} \tag{3.34}$$

For this purpose we minimise the L_2-norm of the error, which is a function of c:

$$\delta(c) = \|G_c - H\| \tag{3.35}$$

The choice of the L_2-norm has the advantage that the error is also minimum in spectral space, due to Parseval's theorem. The minimum value of c will certainly

satisfy $b-a \leq c \leq b+a$. In this range the square of the error equals (after some calculation):

$$(\delta(c))^2 = \frac{1}{b} - \frac{a}{3b^2} + \frac{b+a}{ab} + \frac{1}{c}(\frac{a}{2b} + \frac{b}{2a}) + \frac{c}{2ab} \tag{3.36}$$

Minimisation of the error requires

$$\frac{d}{dc}(\delta(c))^2 = 0, \tag{3.37}$$

which finally yields

$$c = \sqrt{a^2 + b^2} \tag{3.38}$$

It is remarkable that this relation, which represents an optimal approximation for top-hat filters, is identical to the exact relation for Gaussian filters. Furthermore it appears that when equation (3.38) is satisfied for top-hat filters, not only $\delta(c)$ is minimum, but that also the second moments of G_c and H are equal:

$$\int_{-\frac{1}{2}c}^{\frac{1}{2}c} y^2 G_c(y) dy = \int_{-\frac{1}{2}(b+a)}^{\frac{1}{2}(b+a)} y^2 H(y) dy. \tag{3.39}$$

Usually the ratio between the filter width of the test and original filter is equal to 2 ($b = 2a$), in which case equation (3.38) gives $c = \sqrt{5}a$, which corresponds to $\kappa = \sqrt{5}$.

3.3 The unstable nature of the gradient model

Large-Eddy Simulations with the pure gradient model are unstable. Incorporation of a limiter or the Smagorinsky eddy-viscosity can lead to stable simulations, but the results are inaccurate (Vreman *et al.* 1995c). However, the dynamic combination of the gradient and eddy-viscosity model presented in subsection 3.2.4 results in stable and sufficiently accurate simulations. In this section we will analyse the nature of the instability of the pure gradient model for a one-dimensional model problem.

3.3.1 Analysis in one dimension

It is well-known that the Burgers equation is a simple model that describes flow phenomena which are qualitatively similar to Navier-Stokes flows in several respects. Since the Burgers equation is a one-dimensional scalar equation, mathematical analysis is often possible. The equation has been the subject of several studies of LES (Love 1980, Humi 1990). In this section we examine the Burgers

equation supplemented with the one-dimensional version of the gradient part of the Clark model. The linear stability of a sinusoidal profile will be investigated, in order to gain some understanding of the instability of the gradient model encountered in the previous section. The connection between linear and nonlinear stability is known for Navier-Stokes flows and has been formulated in the following way (Henningson & Reddy 1994). If a flow is linearly unstable then it is nonlinearly unstable to arbitrarily small initial disturbances. On the other hand, if a flow is linearly stable then it is nonlinearly stable, provided the initial disturbance is sufficiently small. The linear analysis thus provides information on the nonlinear equation.

The Burgers equation with the gradient subgrid-model is written as:

$$\partial_t u + \tfrac{1}{2}\partial_x(u^2) - \nu\partial_x^2 u = -\tfrac{1}{2}\eta\partial_x(\partial_x u)^2 + f(x), \tag{3.40}$$

where ∂_t and ∂_x denote the time and spatial derivative respectively, u is the one-dimensional velocity and ν the viscosity. The left-hand side of this equation contains all terms in the standard Burgers equation. The right-hand side represents the gradient model with positive parameter $\eta = \frac{1}{12}\Delta^2$ plus a forcing term f.

The following analysis shows that smooth solutions of equation (3.40) can be extremely sensitive to small perturbations, leading to severe instabilities. In particular, we consider the linear stability of a 2π-periodic, stationary solution, $U(x,t) = \sin(x)$ on the domain $[0, 2\pi]$ with periodic boundary conditions. For $\eta \neq 1$ the forcing function f is determined by the requirement that U is a solution of equation (3.40). We notice that no forcing is needed to ensure that U is an exact solution for the inviscid case with $\eta = 1$. We substitute a superposition of U and a perturbation v,

$$u(x,t) = U(x) + v(x,t), \tag{3.41}$$

into equation (3.40) and linearize around U, omitting higher order terms in v:

$$\partial_t v + (1-\eta)\sin(x)\ \partial_x v + (v + \eta\partial_x^2 v)\cos(x) = \nu\partial_x^2 v. \tag{3.42}$$

We use the following Fourier expansion for v

$$v = \sum_{k=-\infty}^{\infty} \alpha_k(t) e^{ikx}, \tag{3.43}$$

where i is the imaginary unit with $i^2 = -1$. After substitution of this series into equation (3.42) and ordering of terms, we obtain an infinite system of ordinary differential equations for the Fourier coefficients α_k:

$$\dot{\alpha}_k = \tfrac{1}{2}k(\eta k - \eta - 1)\alpha_{k-1} - k^2\nu\alpha_k + \tfrac{1}{2}k(\eta k + \eta + 1)\alpha_{k+1}, \tag{3.44}$$

where k is a number in $\mathbb{Z}$.

The instability mentioned in the previous section concerns the gradient model, in which no eddy-viscosity is adopted, while the molecular viscosity is relatively small. Therefore, to understand the nature of this instability for the Burgers equation, we first analyse system (3.44) assuming $\nu = 0$. Instead of the infinite system, we consider a sequence of finite dimensional systems,

$$\dot{\mathbf{z}}_n = M_n \mathbf{z}_n \tag{3.45}$$

where $\mathbf{z}_n$ is a vector containing the $2n+1$ Fourier coefficients $\alpha_{-n}...\alpha_n$ and M_n is a $(2n+1) \times (2n+1)$ tri-diagonal matrix:

$$\mathbf{z}_n = \begin{bmatrix} \alpha_{-n} \\ . \\ . \\ \alpha_{-1} \\ \alpha_0 \\ \alpha_1 \\ . \\ . \\ \alpha_n \end{bmatrix}, \qquad M_n = \begin{bmatrix} 0 & l_n & & & & & & & \\ r_n & . & . & & & & & & \\ & . & . & l_2 & & & & & \\ & & r_2 & 0 & l_1 & & & & \\ & & & 0 & 0 & 0 & & & \\ & & & & l_1 & 0 & r_2 & & \\ & & & & & l_2 & . & . & \\ & & & & & & . & . & r_n \\ & & & & & & & l_n & 0 \end{bmatrix}, \tag{3.46}$$

with

$$l_k = \tfrac{1}{2}k(\eta k - \eta - 1), \tag{3.47}$$

$$r_k = \tfrac{1}{2}(k-1)(\eta k + 1). \tag{3.48}$$

The eigenvalues of A_n determine the stability of the problem. The system is unstable if the maximum of the real parts of the eigenvalues is positive.

In the following we will consider the asymptotic behaviour for large values of n of the maximum of the real parts of the eigenvalues of M_n. We denote the eigenvalues of M_n by λ_j, whereas λ_{max} represents an eigenvalue with

$$|\lambda_{max}| = \max|\lambda_j|. \tag{3.49}$$

In the next subsection the proof is found of the following three properties:

1. if λ is an eigenvalue then $-\lambda$ is an eigenvalue; (3.50)
2. $|\lambda_{max}| \sim \eta n^2$; (3.51)
3. $|\mathrm{Im}(\lambda_{max})| \leq n - 1$. (3.52)

The first point implies that λ_{max} can be chosen such that $\mathrm{Re}(\lambda_{max}) \geq 0$. Hence, the combination of these three properties yields the asymptotic behaviour of the maximum of the real parts of the eigenvalues:

$$\mathrm{Re}(\lambda_{max}) \sim \eta n^2. \tag{3.53}$$

Thus we have shown that the inviscid system is linearly unstable and that the largest real part of the eigenvalues is asymptotically proportional to n^2, where n is the number of Fourier modes taken into account.

It should be observed that the instability is severe, since the system is not only unstable, but the growth rate of the instability is infinitely large as $n \to \infty$. The instability is fully due to the incorporation of the gradient model, since all eigenvalues of the matrix M_n are purely imaginary in case the inviscid Burgers equation without subgrid-model is considered ($\eta = 0$). In numerical simulations the instability will grow with a finite speed, since then the number of Fourier modes is limited by the finite grid. Moreover, expression (3.53) illustrates that grid-refinement (with η kept constant), which corresponds to a larger n, will not stabilize the system, but enhance the instability. Three-dimensional simulations were observed to show features similar to this one-dimensional behaviour. Grid-refinement in LES with the gradient model (Vreman *et al.* 1995c) enhanced the instability when Δ was kept fixed (the grid-spacing h was decreased). However, when the filter width Δ was reduced simultaneously with the grid-refinement, i.e. Δ/h was kept constant, the instability was not enhanced. In fact the growth rate of the instability of the one-dimensional problem can be expressed in Δ and the grid-spacing h: $\eta n^2 \sim (\Delta/h)^2$. Consequently, the instability is not enhanced if the ratio between Δ and h is kept constant.

Finally, we will consider the more complicated case $\nu \neq 0$. The linear system in equation (3.44) now gives rise to matrices M_n which have a negative principal diagonal. It is known that for every fixed value of n there exists an eigenvalue arbitrarily close to the eigenvalue of the inviscid system (λ_{max}) if ν is sufficiently small (Chatelin 1993, (Lemma 4.3.1)). Hence for small values of ν the viscous system for finite n is still linearly unstable. The matrix M_n is strictly diagonally dominant if

$$\nu > \eta + 1, \tag{3.54}$$

while all rows except n and $n+2$ are already diagonally dominant if $\nu > \eta$. If the matrix is diagonally dominant, the real parts of all eigenvalues are negative and, consequently, the system is stable. This indicates that stability can be achieved by a sufficiently large viscosity, which does not depend on n, but only on η. Thus, we conclude that if the gradient model is supplemented with an adequate eddy-viscosity the instability will be removed. The original Clark model, which indeed contains enough eddy-viscosity to avoid instabilities, is too dissipative. An adequate eddy-viscosity formulation which stabilizes the gradient model, while not being too dissipative, occurs in the dynamic Clark model (section 3.2.4).

3.3.2 The eigenvalues in the one-dimensional analysis

In this subsection the proof of the three statements in (3.50) to (3.52) concerning the eigenvalues of the matrix M_n is given.[2] The structure of the matrix M_n is such that an eigenvalue is equal to zero or an eigenvalue of the following matrix:

$$A_n = \begin{bmatrix} 0 & r_2 & & & \\ l_2 & . & . & & \\ & . & . & r_{n-1} & \\ & & l_{n-1} & 0 & r_n \\ & & & l_n & 0 \end{bmatrix}. \tag{3.55}$$

Consequently, to consider the eigenvalues of A_n is sufficient. These eigenvalues are roots of the characteristic polynomial $P_n(\lambda)$ of the matrix A_n:

$$P_n(\lambda) = \det(\lambda I_n - A_n), \tag{3.56}$$

where I_n is the $n \times n$ unity matrix. If we decompose this determinant with respect to the last column, we obtain:

$$P_1(\lambda) = \lambda, \tag{3.57}$$

$$P_2(\lambda) = \lambda^2 - r_2 l_2, \tag{3.58}$$

$$P_n(\lambda) = \lambda P_{n-1}(\lambda) - r_n l_n P_{n-2}(\lambda), \quad n > 2. \tag{3.59}$$

This recursive relation demonstrates that $P_n(\lambda) = 0$ implies $P_n(-\lambda) = 0$. Thus if λ is an eigenvalue, $-\lambda$ is also an eigenvalue and thus property (3.50) has been established.

Next, we consider the statement about the asymptotic behaviour of $|\lambda_{max}|$, expressed in (3.51). In order to proof this statement we formulate a lower- and upper-bound for $|\lambda_{max}|$ which are both asymptotically proportional to ηn^2. An upper-bound is obtained when the Gershgorin theory is applied to A_n:

$$|\lambda_{max}| \leq l_{n-1} + r_n = \eta(n-1)^2 \sim \eta n^2. \tag{3.60}$$

Since $|\lambda_{max}| > |\lambda_i|$ for $i = 1, .., n$ and λ_i represents one of the n roots of the polynomial $P_n(\lambda)$, the following relation provides a lower-bound for $|\lambda_{max}|$:

$$|\lambda_{max}| \geq |\lambda_1 \lambda_2 ... \lambda_n|^{\frac{1}{n}} = |P_n(0)|^{\frac{1}{n}}. \tag{3.61}$$

The recursive relation (3.59) provides

$$P_n(0) = -r_n l_n P_{n-2}(0), \tag{3.62}$$

[2] Dr. R.M.J. van Damme (Department of Applied Mathematics, University of Twente) significantly contributed to the proof of (3.51).

with

$$r_n l_n = \tfrac{1}{4}(n-1)n(\eta^2(n^2-n)-\eta-1) \sim \tfrac{1}{4}\eta^2(n-1)^2n^2. \tag{3.63}$$

If n is even and the coefficient l_k is non-zero for even k (r_k is always non-zero), we obtain the following estimate, using Stirling's formula:

$$|\lambda_{max}| \geq |P_n(0)|^{\frac{1}{n}} \sim ((\tfrac{1}{4}\eta^2)^{\frac{n}{2}}(n!)^2)^{\frac{1}{n}} \geq \tfrac{1}{2}\eta(\frac{n}{e})^2 \sim \eta n^2. \tag{3.64}$$

The equations (3.60) and (3.64) together yield

$$|\lambda_{max}| \sim \eta n^2. \tag{3.65}$$

The case for odd n is more complicated, but does not need to be considered, since the behaviour for even n already provides sufficient information about the system. Furthermore, the above argument alters when $l_k = 0$ for a certain (even) value of k. If $l_k = 0$ the characteristic polynomial can be written as

$$P_n(\lambda) = P_{k+1}(\lambda)Q_{n-k+1}(\lambda), \tag{3.66}$$

where $Q_{n-k+1}(\lambda)$ represents the characteristic polynomial of the tri-diagonal matrix with lower diagonal $l_{k+1}..l_n$ and upper diagonal $r_{k+1}..r_n$. The maximum root of Q_{n-k+1} can be estimated like in equation (3.64) and its asymptotic behaviour is also proportional to ηn^2.

Finally, we derive an upper-bound for the imaginary part of an eigenvalue λ of A_n, expressed in (3.51). Denoting the corresponding eigenvector with $\mathbf{y}$ we have

$$A_n\mathbf{y} = \lambda\mathbf{y}. \tag{3.67}$$

The matrix A_n can be split into a symmetric matrix B_n and an anti-symmetric matrix C_n:

$$A_n = B_n + C_n \tag{3.68}$$

with

$$B_n = \begin{bmatrix} 0 & b_2 & & \\ b_2 & \cdot & \cdot & \\ & \cdot & \cdot & b_n \\ & & b_n & 0 \end{bmatrix}, \qquad C_n = \begin{bmatrix} 0 & c_2 & & \\ -c_2 & \cdot & \cdot & \\ & \cdot & \cdot & c_n \\ & & -c_n & 0 \end{bmatrix}, \tag{3.69}$$

and

$$b_k = \tfrac{1}{2}(r_k + l_k) = \tfrac{1}{2}\eta k^2 - \tfrac{1}{2}\eta k + \tfrac{1}{4}, \tag{3.70}$$

$$c_k = \tfrac{1}{2}(r_k - l_k) = \tfrac{1}{2}k - \tfrac{1}{4}. \tag{3.71}$$

In the following we denote the Eucledian inner product in $\mathbb{C}^n$ by $(\cdot,\cdot)$ and the complex conjugate by the superscript $(*)$. Next, we derive the following relation between λ and λ^*:

$$\begin{aligned}
\lambda(\mathbf{y},\mathbf{y}) &= (A_n\mathbf{y},\mathbf{y}) \\
&= (B_n\mathbf{y},\mathbf{y}) + (C_n\mathbf{y},\mathbf{y}) \\
&= (\mathbf{y},B_n^T\mathbf{y}) + (\mathbf{y},C_n^T\mathbf{y}) \\
&= (\mathbf{y},B_n\mathbf{y}) - (\mathbf{y},C_n\mathbf{y}) \\
&= (\mathbf{y},A_n\mathbf{y}) - 2(\mathbf{y},C_n\mathbf{y}) \\
&= \lambda^*(\mathbf{y},\mathbf{y}) - 2(\mathbf{y},C_n\mathbf{y}) \qquad (3.72)
\end{aligned}$$

Now we can express an upper-bound for the imaginary part of λ as:

$$|\mathrm{Im}(\lambda)| = \tfrac{1}{2}|\lambda-\lambda^*| = |\frac{(\mathbf{y},C_n\mathbf{y})}{(\mathbf{y},\mathbf{y})}| \leq \frac{\|\mathbf{y}\|\ \|C_n\mathbf{y}\|}{\|\mathbf{y}\|^2} \leq \|C\|_{sp}, \qquad (3.73)$$

since $\|C_n\mathbf{y}\| \leq \|C_n\|_{sp}\|\mathbf{y}\|$, where the subscript $'sp'$ denotes the spectral matrix norm. The spectral matrix norm $\|C\|_{sp}$ is defined as the square root of the maximum of the absolute eigenvalues of the matrix $C_n^TC_n$, which is equal to the maximum absolute eigenvalue of C_n, since C_n is anti-symmetric. Finally, the following result is obtained using the Gershgorin theory:

$$|\mathrm{Im}(\lambda)| \leq |c_{n-1}| + |c_n| = n-1, \qquad (3.74)$$

which expresses an upper-bound for the imaginary parts of the eigenvalues.

3.4 Conclusions

In this chapter six subgrid-models for the turbulent stress tensor have been presented: three basic subgrid-models and three dynamic models composed of the basic models. A comparison of simulation results obtained with these models is found in chapter 5.

The basic subgrid-models are the Smagorinsky, similarity and gradient model. The three dynamic models considered are the dynamic eddy-viscosity, the dynamic mixed and the dynamic Clark model. The dynamic models rely upon the Germano identity for the turbulent stress tensor. We have generalised the Germano identity in order to be able to apply the procedure to other subgrid-terms as well. Furthermore, an improved formulation of the dynamic mixed model has been proposed. The dynamic Clark model is the gradient model supplemented with an dynamic eddy-viscosity. It has been introduced to overcome the intrinsic instability of the pure gradient model and the excessive dissipation of the original

Clark model. With respect to the dynamic procedure using top-hat filters, an optimum value for the filter width of two consecutively applied top-hat filters was obtained. This value is different from the value that has previously been used for top-hat filters, whereas it is identical to the exact value for Gaussian filters.

The gradient model has been considered in more detail. First, we have extended the formal derivation of the incompressible gradient model to be able to use the model in compressible flow simulations. In order to clarify the nature of the instability of the gradient model, the one-dimensional Burgers equation supplemented with the gradient model has been analysed. A linear stability analysis of a sinusoidal profile of the modified Burgers equation has been performed. In the limit of vanishing viscosity, the maximum of the positive real parts of the eigenvalues has been shown to be proportional to the square of the number of modes, if a finite number of modes is taken into account. This shows that the instability becomes more severe, if the resolution is increased. For an infinite number of modes, the growth-rate of the instability is infinitely large. The one-dimensional analysis also indicates that a sufficient amount of viscosity can stabilize the model, independent of the number of modes. These analytical results for the one-dimensional case are similar to the behaviour of the instability observed in three-dimensional simulations with the gradient model.

Chapter 4

Realizability conditions for the turbulent stress tensor

In this chapter[1] we examine the turbulent stress tensor τ_{ij} in the filtering approach, defined by equation (2.23) from a theoretical point of view. The filtering approach, which is the basis of LES, is different from the classical way to average the Navier-Stokes equations. In the classical approach, also known as the statistical approach, the equations are averaged with a statistical mean or ensemble average (Tennekes & Lumley 1972). The turbulent stress reduces to the Reynolds stress, which is a statistical central moment, and satisfies the so-called 'realizability conditions' (Du Vachat 1977; Schumann 1977). Unlike the ensemble average in the statistical approach, the averaging operator in the filtering approach does not satisfy the Reynolds rules for the mean (Monin & Yaglom 1971, p. 207). Although for this reason the turbulent stress in the filtering approach is not equal to the Reynolds stress, several analogies between the turbulent stress in the filtering approach and the Reynolds stress exist. First, the turbulent stress in the filtering approach satisfies the Reynolds equations, which are the partial differential equations that can be derived for the Reynolds stress in the statistical approach (Germano 1992). In addition to this property, which is called the averaging invariance of the filtered equations, Germano presents an algebraic identity for the turbulent stress (section 3.2.1). Invariances or algebraic properties related to the Large-Eddy Simulation technique and their applications on subgrid-modelling are scarcely found in literature. In addition to Germano's work, the work of Speziale (1985) has to be mentioned, in which the Galilean invariance of subgrid-models is discussed.

In this chapter it will be shown that the realizability conditions for the Reynolds stress in the statistical approach are also valid for the turbulent stress

[1] This chapter is based on the paper Vreman *et al.* 1994a.

in the filtering approach, if and only if the filter function is positive. The proof of this statement is given in section 4.1, while in the section 4.2 the theory is illustrated for three filters commonly used in Large-Eddy Simulation. Furthermore, in section 4.3 it is argued that a consistent subgrid-model for the turbulent stress should satisfy the same inequalities as the turbulent stress itself. Whether this requirement is fulfilled is investigated for several existing subgrid-models. Moreover, it is shown that for eddy-viscosity models the realizability conditions lead to a lower bound for the generalised turbulent kinetic energy.

For sake of transparency we use the incompressible formulation of the turbulent stress tensor,

$$\tau_{ij} = \overline{u_i u_j} - \overline{u}_i \overline{u}_j, \tag{4.1}$$

The compressible case is covered when the bar filter is replaced by the Favre filter.

4.1 Realizability conditions

The filtering approach presented in section 2.2 is different from the statistical approach, in which the averaging operator represents the ensemble average and τ_{ij} is equal to the Reynolds stress $\overline{u_i' u_j'}$. Since the averaging operator is a statistical mean, it is well-known that the tensor $\overline{u_i' u_j'}$ is positive semidefinite (Du Vachat 1977; Schumann 1977). If the tensor τ_{ij} is positive semidefinite (or 'positive' for convenience) then the following inequalities hold (Ortega 1987, p. 36):

$$\tau_{ii} \geq 0 \quad \text{for} \quad i \in \{1,2,3\}, \tag{4.2}$$

$$|\tau_{ij}| \leq \sqrt{\tau_{ii}\tau_{jj}} \quad \text{for} \quad i,j \in \{1,2,3\}, \tag{4.3}$$

$$\det(\tau_{ij}) \geq 0. \tag{4.4}$$

By analogy to the statistical approach we refer to these three properties as 'realizability conditions'. If the filtering approach is followed, in general $\tau_{ij} \neq \overline{u_i' u_j'}$ and, therefore, we will investigate the conditions under which τ_{ij} is positive semidefinite.

The turbulent stress tensor τ_{ij} in Large-Eddy Simulation is preferred to be 'positive' for a number of reasons. First, if τ_{ij} is 'positive', the generalised turbulent kinetic energy formally introduced by Germano (1992),

$$k = (\tau_{11} + \tau_{22} + \tau_{33})/2, \tag{4.5}$$

is a positive quantity at each location of the flow domain for an arbitrary velocity field. This quantity is frequently used in the theory of subgrid-modelling and is often required to be positive. As an example, we mention the available k-equation

models, which would become ill-defined for negative values of k. Moreover, twice the turbulent kinetic energy is an upper bound for all components of the turbulent stress, i.e. $|\tau_{ij}| \leq 2k$ for all i and j, which follows from the estimates given in equation (4.3). Other analogies between the classical approach with the ensemble average and the filtering approach exist, if τ_{ij} is 'positive'. For example, as in the classical approach, the fractions $\tau_{ij}/\sqrt{\tau_{ii}\tau_{jj}}$ in the filtering approach can be considered as correlation coefficients. The existence of such analogies could be a reason why turbulence models developed for the ensemble averaged equations can often be applied in Large-Eddy Simulation. An example is Smagorinsky's model (Smagorinsky 1963), which is quite similar to the classical mixing length model by Prandtl.

In the following it will be proved that τ_{ij} in LES is positive semidefinite if and only if the filter kernel $G(\mathbf{x}, \boldsymbol{\xi})$ is positive for all $\mathbf{x}$ and $\boldsymbol{\xi}$. As a first step, suppose $G \geq 0$. In order to prove that τ_{ij} is 'positive' for all $\mathbf{x}$ in the flow domain Ω, a subset $\Omega_{\mathbf{x}}$ is defined, being the support of the function $\boldsymbol{\xi} \rightarrow G(\mathbf{x}, \boldsymbol{\xi})$. Moreover $F_{\mathbf{x}}$ is the space of real functions on the domain $\Omega_{\mathbf{x}}$. Since $G \geq 0$, for $f, g \in F_{\mathbf{x}}$ the expression

$$(f, g)_{\mathbf{x}} = \int_{\Omega_{\mathbf{x}}} G(\mathbf{x}, \boldsymbol{\xi}) f(\boldsymbol{\xi}) g(\boldsymbol{\xi}) d\boldsymbol{\xi} \tag{4.6}$$

defines an inner product on $F_{\mathbf{x}}$ (Rudin 1973, p. 292). Next, we show that the turbulent stress can be written as an inner product. Using the definition of the filter operator, equation (2.11), and property (2.12) yields

$$\begin{aligned}
\tau_{ij}(\mathbf{x}) &= \overline{u_i u_j}(\mathbf{x}) - \overline{u}_i(\mathbf{x})\overline{u}_j(\mathbf{x}) \\
&= \overline{u_i u_j}(\mathbf{x}) - \overline{u}_i(\mathbf{x})\overline{u}_j(\mathbf{x}) - \overline{u}_j(\mathbf{x})\overline{u}_i(\mathbf{x}) + \overline{u}_i(\mathbf{x})\overline{u}_j(\mathbf{x}) \\
&= \int_{\Omega_{\mathbf{x}}} G(\mathbf{x}, \boldsymbol{\xi}) u_i(\boldsymbol{\xi}) u_j(\boldsymbol{\xi}) d\boldsymbol{\xi} - \overline{u}_i(\mathbf{x}) \int_{\Omega_{\mathbf{x}}} G(\mathbf{x}, \boldsymbol{\xi}) u_j(\boldsymbol{\xi}) d\boldsymbol{\xi} \\
&\quad - \overline{u}_j(\mathbf{x}) \int_{\Omega_{\mathbf{x}}} G(\mathbf{x}, \boldsymbol{\xi}) u_i(\boldsymbol{\xi}) d\boldsymbol{\xi} + \overline{u}_i(\mathbf{x})\overline{u}_j(\mathbf{x}) \int_{\Omega_{\mathbf{x}}} G(\mathbf{x}, \boldsymbol{\xi}) d\boldsymbol{\xi} \\
&= \int_{\Omega_{\mathbf{x}}} G(\mathbf{x}, \boldsymbol{\xi}) (u_i(\boldsymbol{\xi}) - \overline{u}_i(\mathbf{x}))(u_j(\boldsymbol{\xi}) - \overline{u}_j(\mathbf{x})) d\boldsymbol{\xi} = (v_i^{\mathbf{x}}, v_j^{\mathbf{x}})_{\mathbf{x}}, \quad (4.7)
\end{aligned}$$

with $v_i^{\mathbf{x}}(\boldsymbol{\xi}) \equiv u_i(\boldsymbol{\xi}) - \overline{u}_i(\mathbf{x})$ defined on $\Omega_{\mathbf{x}}$. In this way the tensor τ_{ij} forms a 3×3 Grammian matrix of inner products. Since such a matrix is always positive semidefinite (Ortega 1987, p. 74), τ_{ij} is positive semidefinite and satisfies the realizability conditions. Remark that $v_i^{\mathbf{x}}(\boldsymbol{\xi})$ is not identical to the standard velocity fluctuation $u_i'(\boldsymbol{\xi}) = u_i(\boldsymbol{\xi}) - \overline{u}_i(\boldsymbol{\xi})$, since $v_i^{\mathbf{x}}(\boldsymbol{\xi})$ also depends on $\mathbf{x}$. Consequently, expression (4.7) is not equal to $\overline{u_i' u_j'}$.

We proceed to show that $G \geq 0$ is not only a sufficient, but also a necessary condition for τ_{ij} to be positive semidefinite. Suppose the condition $G \geq 0$ is not

fulfilled for a piecewise-continuous filter function G. Then vectors $\mathbf{x}$ and $\hat{\boldsymbol{\xi}}$ in Ω and a neighbourhood of $\hat{\boldsymbol{\xi}}$, $V = \{\boldsymbol{\xi} \in \Omega : |\boldsymbol{\xi} - \hat{\boldsymbol{\xi}}| < \delta\}$ exist, such that $G(\mathbf{x}, \boldsymbol{\xi}) < 0$ for all $\boldsymbol{\xi} \in V$. For a function u_1 on Ω with $u_1(\boldsymbol{\xi}) \neq 0$ if $\boldsymbol{\xi} \in V$ and $u_1(\boldsymbol{\xi}) = 0$ elsewhere, $\tau_{11}(\mathbf{x})$ appears to be negative:

$$\tau_{11}(\mathbf{x}) = \overline{u_1^2}(\mathbf{x}) - (\overline{u}_1(\mathbf{x}))^2 \leq \overline{u_1^2}(\mathbf{x}) = \int_V G(\mathbf{x}, \boldsymbol{\xi})(u_1(\boldsymbol{\xi}))^2 d\boldsymbol{\xi} < 0. \tag{4.8}$$

Consequently, the tensor τ_{ij} is not positive semidefinite, which completes the proof that τ_{ij} is positive semidefinite if and only if the filter function G is positive.

We finally show that the fractions $\tau_{ij}/\sqrt{\tau_{ii}\tau_{jj}}$ in the filtering approach can be interpreted as local statistical correlation coefficients. For a given $\mathbf{x}$ we can define a local stochastic variable $\boldsymbol{\Xi}_\mathbf{x}$ for the location vector $\boldsymbol{\xi}$ with probability density function $P_\mathbf{x}(\boldsymbol{\xi}) = G(\mathbf{x}, \boldsymbol{\xi}) \geq 0$. Hence, the filtered velocity $\bar{u}_i$ can be interpreted as the statistical mean $E_\mathbf{x}$ of the stochastic variable $u_i(\boldsymbol{\Xi}_\mathbf{x})$ and the turbulent stress tensor τ_{ij} as the covariance $\mathrm{cov}_\mathbf{x}(u_i(\boldsymbol{\Xi}_\mathbf{x})u_j(\boldsymbol{\Xi}_\mathbf{x}))$.

4.2 Filters

In the previous section we have shown that the turbulent stress tensor is positive semidefinite if and only if the condition $G \geq 0$ is fulfilled. If this is the case, we call the corresponding filter a *positive filter*. In this section we consider some of the positive and non-positive filters which frequently appear in the literature about Large Eddy Simulation. Moreover, turbulent kinetic energies obtained with positive and non-positive filters are compared for a fully developed turbulent flow field.

Typical filters commonly used in Large Eddy Simulation, the top-hat, Gaussian and spectral cut-off filter, have been listed in table 2.1. The top-hat and Gaussian filters are positive, whereas the spectral cut-off is not. Hence τ_{ij} is 'positive' if the first two filters are applied, but not if the spectral cut-off is applied to the velocity field. For compressible flows the Favre filter is used, $\tilde{u}_i = \overline{\rho u_i}/\overline{\rho}$, where ρ is the density (Erlebacher *et al.* 1992). In fact $\tilde{u}_i$ can be written as

$$\tilde{u}_i(\mathbf{x}) = \int_\Omega H(\mathbf{x}, \boldsymbol{\xi}) u_i(\boldsymbol{\xi}) d\boldsymbol{\xi} \tag{4.9}$$

with

$$H(\mathbf{x}, \boldsymbol{\xi}) = \frac{G(\mathbf{x}, \boldsymbol{\xi})\rho(\boldsymbol{\xi})}{\int_\Omega G(\mathbf{x}, \boldsymbol{\eta})\rho(\boldsymbol{\eta}) d\boldsymbol{\eta}}. \tag{4.10}$$

The function $H(\mathbf{x}, \boldsymbol{\xi})$ is clearly a filter-function, since $\int_\Omega H(\mathbf{x}, \boldsymbol{\xi}) d\boldsymbol{\xi} = 1$. Moreover, the Favre filter is positive if the corresponding $G(\mathbf{x}, \boldsymbol{\xi})$ is positive. Thus,

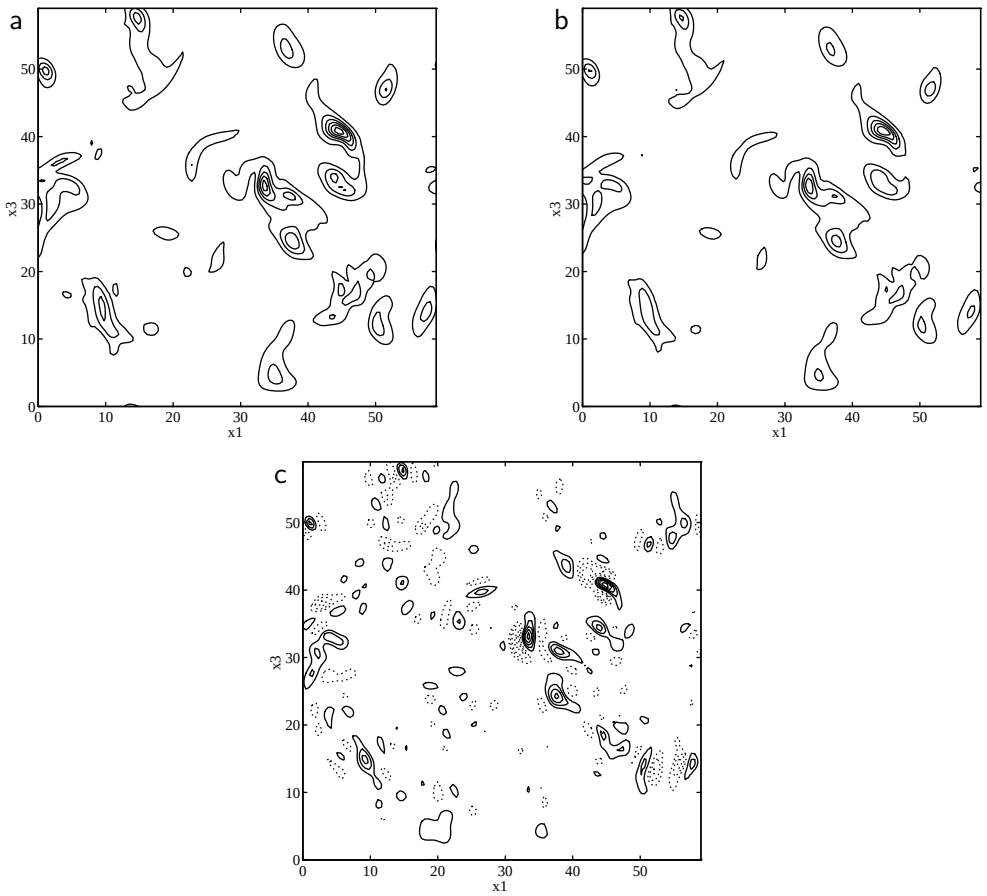

Figure 4.1: Contours of the generalised turbulent kinetic energy in the centre plane of the mixing layer at $t = 80$ for (a) the top-hat filter, (b) the Gaussian filter and (c) the spectral cut-off filter. Solid and dotted contours indicate positive and negative values respectively. The contour increment is 0.04.

this filter inherits positivity from the underlying 'bar'-filter, but does in general not commute with partial derivatives, unlike the filters listed in table 2.1.

Next the specific behaviour of the turbulent stress based on the spectral cut-off filter is illustrated. First, as an example the sinusoidal velocity profile $u_1 = \sin(ak_c x_1)$ with $\frac{1}{2} < a < 1$ is considered and the cut-off filter is applied with cut-off wavenumber k_c. Since u_1 is a single Fourier mode, the filter operation is easily performed in Fourier space. This implies

$$\tau_{11} = \overline{\tfrac{1}{2} - \tfrac{1}{2}\cos(2ak_c x_1)} - (\tfrac{1}{2} - \tfrac{1}{2}\cos(2ak_c x_1)) = \tfrac{1}{2}\cos(2ak_c x_1), \qquad (4.11)$$

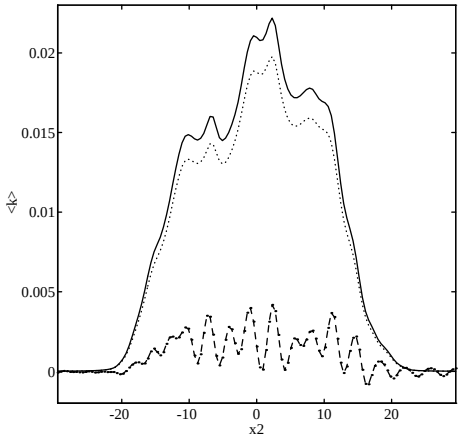

Figure 4.2: The generalised turbulent kinetic energy averaged in the homogeneous directions as a function of the normal coordinate (x_2) for the mixing layer at $t = 80$. Top-hat filter (solid), Gaussian filter (dotted) and spectral cut-off filter (dashed).

which is not positive for all x_1. Consequently, for spectrally filtered fields τ_{ij} does not satisfy the realizability conditions. As a further illustration the generalised turbulent kinetic energy is calculated by filtering a turbulent velocity field. For this purpose we use the database of a Direct Numerical Simulation of the temporal mixing layer in three dimensions with a convective Mach number of 0.2 (Vreman *et al.*, 1995a). At this Mach number the flow can be regarded as incompressible (Sandham & Reynolds, 1991). The simulation was performed on a uniform cubic grid with grid-spacing h and 128^3 grid-points. Furthermore, an additional simulation on a 192^3-grid confirmed the accuracy of the database (see section 5.1). In the following the turbulent flow field at $t = 80$ is used for the calculation of the generalised turbulent kinetic energy k, defined in equation (4.5). We compare k obtained with the top-hat and Gaussian filter, as examples of positive filters, to k obtained with the spectral cut-off filter. The filter width Δ, which is the same in the three filter functions, is chosen equal to $4h$, which implies that if a Large-Eddy Simulation of this flow is performed with grid-spacing Δ, the grid contains 32^3 cells. In figure 4.1 contours of k are shown in the centre plane of the shear layer for the three filters. Moreover, k averaged in the two homogeneous directions of the flow ($< k >$) is plotted as a function of the normal coordinate in figure 4.2. These figures show that the generalised turbulent kinetic energy k is positive everywhere, if the top-hat or Gaussian filter is used. However, if the spectral cut-off is employed, k and even $< k >$ are negative in

some parts of the flow.

As a conclusion, unlike the top-hat and Gaussian filters, the spectral cut-off filter gives rise to a turbulent stress tensor which does not satisfy the realizability conditions. This does not imply that τ_{ij} becomes ill-defined for the spectral cut-off filter. However, certain properties of τ_{ij} which are true for positive filters do not hold for the spectral cut-off. In particular the generalised turbulent kinetic energy, k, obtained with spectrally filtered velocity fields, can locally be negative. Similarly, the generalised turbulent dissipation rate (Germano 1992, equation (25)),

$$\epsilon = \nu \sum_{i=1}^{3} \sum_{k=1}^{3} (\overline{(\partial_k u_i)^2} - \overline{\partial_k u_i}^2), \tag{4.12}$$

can locally be negative if a spectral filter is used, while it is positive for positive filters. Some consequences of these properties will be discussed in the next section. Finally, the fact that τ_{ij} based on spectrally filtered fields is not 'positive' might explain the large amount of backscatter for this filter when compared to positive filters (Piomelli *et al.* 1990b).

4.3 Subgrid-models

The Large-Eddy Simulation approach is to close the filtered equations by replacing the exact turbulent stress τ_{ij} with a subgrid-model, represented by the tensor m_{ij}. A model which shares some basic properties with the turbulent stress is appealing from a theoretical point of view. For example, since τ_{ij} is a symmetric tensor, the model m_{ij} is preferred to be symmetric as well, which is true for all existing subgrid-models. Secondly, the filtered Navier-Stokes equations are Galilean invariant. As Speziale (1985) has argued, they should retain this property if τ_{ij} is replaced by the model m_{ij}. The observation that τ_{ij} is 'positive' for positive filters is another basic property of the turbulent stress. Therefore, it is reasonable to require the model m_{ij} to be 'positive' as well, if a positive filter is adopted. Such a requirement is not only based on theoretical, but also on practical grounds. For example, it provides a useful lower bound for the generalised turbulent kinetic energy in case an eddy-viscosity model is adopted, as will be shown below. In the following the three basic subgrid-models introduced in section 3.2 are considered and the question whether they are 'positive' for positive filters is addressed. We also discuss the dynamic models and some other models that occur in literature.

First consider Bardina's scale-similarity model in the incompressible formulation (Bardina *et al.* 1984):

$$m_{ij} = \overline{\overline{u}_i \overline{u}_j} - \overline{\overline{u}}_i \overline{\overline{u}}_j. \tag{4.13}$$

This tensor is obtained if the definition of the turbulent stress τ_{ij} (equation (4.1)) is applied to the filtered velocity field $\overline{u}_i$. The tensor m_{ij} is also called the resolved turbulent stress (Germano 1992) and is clearly 'positive' for positive filters. Another 'positive' tensor is the gradient model, which reads in its incompressible formulation (Clark *et al.* 1979),

$$m_{ij} = \tfrac{1}{12}\Delta^2(\nabla\overline{u}_i \cdot \nabla\overline{u}_j). \tag{4.14}$$

This tensor is positive semidefinite since it can be interpreted as a Grammian matrix with respect to the Eucledian inner product in $\mathbb{R}^3$. Notice that m_{ij} is 'positive', even if the filter is not positive, and, consequently the use of this model in conjunction with e.g. the spectral cut-off filter is not consistent.

The two subgrid-models discussed above are not of the eddy-viscosity type. Next we turn to the group of eddy-viscosity models (e.g. Rogallo & Moin 1984). The anisotropic part of the turbulent stress, $\tau^a_{ij} = \tau_{ij} - \frac{2}{3}k\delta_{ij}$, is modelled with

$$m^a_{ij} = -\nu_e S_{ij}. \tag{4.15}$$

The symbol ν_e represents the eddy-viscosity and S_{ij} is a short notation for the strain-rate $S_{ij}(\overline{\mathbf{u}})$ defined in (2.6). The sum of the anisotropic and isotropic parts is formally written as

$$m_{ij} = -\nu_e S_{ij} + \tfrac{2}{3}k\delta_{ij}. \tag{4.16}$$

An interesting result is obtained if m_{ij} is required to satisfy the realizability conditions. This requirement implies:

$$m^2_{12} + m^2_{13} + m^2_{23} \leq m_{11}m_{22} + m_{11}m_{33} + m_{22}m_{33}. \tag{4.17}$$

Equation (4.16) is substituted in this expression, which yields

$$\nu_e^2(S^2_{12} + S^2_{13} + S^2_{23}) \leq \nu_e^2(S_{11}S_{22} + S_{11}S_{33} + S_{22}S_{33}) + \tfrac{4}{3}k^2. \tag{4.18}$$

Here the property that the tensor S_{ij} is trace-less has been employed. This property is also used to rewrite the terms between parentheses in the right-hand side of equation (4.18) as follows:

$$\begin{aligned} S_{11}S_{22} + S_{11}S_{33} + S_{22}S_{33} &= \tfrac{1}{2}(S_{11} + S_{22} + S_{33})^2 - \tfrac{1}{2}(S^2_{11} + S^2_{22} + S^2_{33}) \\ &= -\tfrac{1}{2}(S^2_{11} + S^2_{22} + S^2_{33}). \end{aligned}$$

Substituting this expression in equation (4.18) finally yields:

$$k \geq \tfrac{1}{2}\sqrt{3}(\nu_e\sqrt{S}) \quad \text{with} \quad S = \tfrac{1}{2}\sum_{i,j} S^2_{ij}. \tag{4.19}$$

This inequality presents a lower bound for the generalised turbulent kinetic energy k, in the case an eddy-viscosity model is adopted in conjunction with a positive filter.

The lower bound for k provides information on the isotropic part of the turbulent stress in the eddy-viscosity formulation. In a Large Eddy Simulation of incompressible flow the isotropic part is usually added to the filtered pressure, resulting in a modified pressure (Rogallo & Moin 1984). In that case, the Large-Eddy Simulation solves the modified pressure, while the (filtered) pressure itself remains unknown, which is undesirable in applications in which the pressure is an important quantity. The approach involving a modified pressure especially causes problems in the Large-Eddy Simulation of compressible flows, since in the evolution equations for compressible flows the pressure does not only appear in the momentum equations, but also in the energy evolution equation and in the equation of state. For these reasons subgrid-models have been proposed that explicitly prescribe k in order to model the isotropic part of the turbulent stress. For such models inequality (4.19) is particularly interesting since it implies inequalities for the model coefficients, as shown in the following part of this section.

In fact inequality (4.19) can be used to suggest a subgrid-model for k corresponding to a specific eddy-viscosity model. We will demonstrate this for the Smagorinsky model, which leads to the Yoshizawa model for k. A similar procedure could be followed for e.g. the structure function eddy-viscosity model (Normand & Lesieur 1992). In a formulation equivalent to that given by Leith (1991) the Smagorinsky eddy-viscosity (Smagorinsky 1963) is defined as

$$\nu_e = C_S^2 \Delta^2 \sqrt{S}, \tag{4.20}$$

where C_S is the Smagorinsky constant. Inequality (4.19) now reduces to

$$k \geq \tfrac{1}{2}\sqrt{3} C_S^2 \Delta^2 S, \tag{4.21}$$

which suggests the following subgrid-model for k:

$$k = C_k \Delta^2 S, \tag{4.22}$$

where the constant C_k has to satisfy

$$C_k \geq \tfrac{1}{2}\sqrt{3} C_S^2. \tag{4.23}$$

This inequality expresses a necessary condition for realizability, if a positive filter is used. The model for the generalised turbulent kinetic energy k in equation (4.22) is similar to the estimates for k, given by Lilly (1967), Deardorff (1970), while it is known as the Yoshizawa model (Yoshizawa 1986). Yoshizawa proposes $C_S (= C_{uu2}) = 0.16$ and $C_k (= C_{uu2}^4 / C_{uu1}^2) = 0.0886$, where C_{uu1} and C_{uu2} are

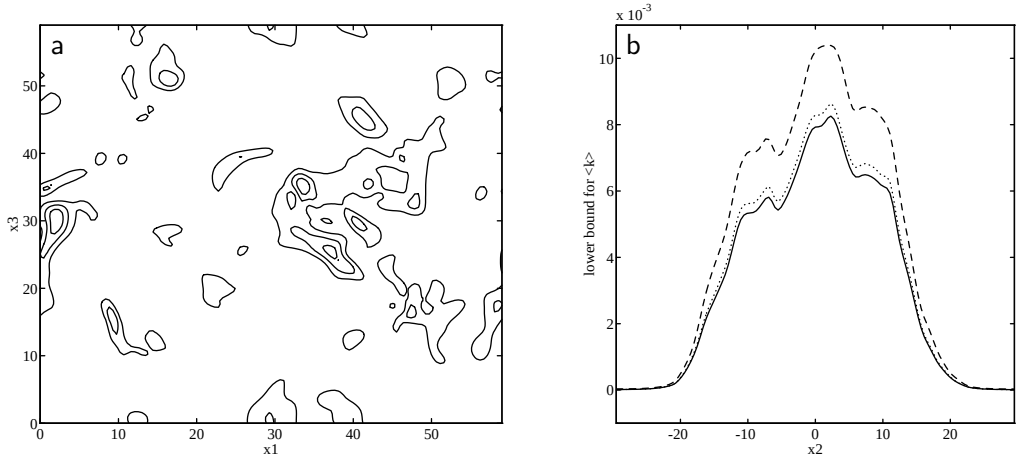

Figure 4.3: Lower bound using the Smagorinsky-eddy viscosity with $C_S = 0.16$ for the mixing layer at $t = 80$. (a) Contours of the lower bound for the top-hat filter in the centre plane . Solid and dotted contours indicate positive and negative values respectively. The contour increment is 0.015. (b) Lower bound averaged in the homogeneous directions as a function of the normal coordinate (x_2). Top-hat filter (solid), Gaussian filter (dotted) and spectral cut-off filter (dashed).

notations which Yoshizawa uses in his presentation of the model. These values clearly satisfy inequality (4.23).

The right-hand side of inequality (4.19) has been evaluated for the Smagorinsky eddy-viscosity using the numerical database described in the previous section. Results for the centre plane are shown in figure 4.3a for the top-hat filter. The agreement with figure 4.1a is reasonable and quantitatively corresponds to a correlation of 0.62. Thus Yoshizawa's model gives a reasonably good prediction of k on the tensor level, which is in agreement with the findings of Erlebacher *et al.* (1987, table 10). The results of averaging the right-hand side of (4.19) in the homogeneous directions are shown in figure 4.3b, which may be compared with figure 4.2. For the positive filters (top-hat and Gaussian) we observe that inequality (4.19) is satisfied and that some global features of $< k >$ are present in the lower bound as well. The lower bound is about twice as small as k. For the non-positive spectral cut-off, inequality (4.19) is clearly not satisfied. Since the Yoshizawa model leads to positive values for k, it is suggested not to use the Yoshizawa model in conjunction with the spectral cut-off filter, for which the exact k does attain negative values. It should be noticed that, on the vector level, i.e. when ∇k is considered, the correlation of the Yoshizawa model is poor

(Erlebacher *et al.* 1987; Speziale *et al.* 1988).

The SEZH-model (Erlebacher *et al.* 1992; Zang *et al.* 1992)) is the sum of the similarity model and Yoshizawa's model. This model was developed using the Gaussian filter, which is positive. The references suggest $C_S(=\sqrt{(C_R/\sqrt{2})}) = 0.092$ and $C_k(=C_I/2) = 0.0033$ or even $C_k = 0$. These values do not satisfy (4.23) and, consequently, the Yoshizawa part of this model is not realizable. However, this does not imply non-realizability of the complete SEZH-model, since the sum of the similarity model and Yoshizawa's model can theoretically still be positive semidefinite. For this reason it is consistent to reformulate the SEZH-model in the following way: rather than modelling the 'positive' tensor $\overline{u_i' u_j'}$, the Yoshizawa model approximates $\tau_{ij} - (\overline{\overline{u}_i \overline{u}_j} - \overline{\overline{u}}_i \overline{\overline{u}}_j)$, which in general is not 'positive'.

An alternative for modelling k is to solve this quantity using an additional partial differential equation for k (Schumann, 1975; Horiuti 1985; Moin & Jimenez 1993). In this formulation the eddy-viscosity equals

$$\nu_e = C\Delta\sqrt{k} \tag{4.24}$$

with model coefficient C, while in the modelled k-equation terms proportional to $\sqrt{k}$ and $k^{3/2}$ occur. This model requires positive values for k and the formulation is such that k remains positive during the simulation, i.e. the model is 'realizable'. As for the gradient and Yoshizawa models, it is consistent to use the k-equation models in conjunction with positive filters only, since the exact k is guaranteed to be positive in this case. To employ these models with e.g. the spectral cut-off filter is less attractive, since in that case the original turbulent kinetic energy attains values of both signs, while the model provides positive values only.

Finally, we discuss the implications for the dynamic eddy-viscosity, the dynamic mixed and the dynamic Clark model, formulated by equation (3.22), (3.26) and (3.30) respectively. The incompressible formulation of these models is obtained with use of the incompressible formulation of the basic models given in the equations (4.13), (4.14) and (4.15).

The dynamic eddy-viscosity model can be supplemented with an isotropic part of the form (4.22) in order to satisfy realizability. The coefficient C_k should satisfy inequality (4.23), where C_S^2 is replaced by the dynamic coefficient C_d,

$$C_k \geq \tfrac{1}{2}\sqrt{3}C_d. \tag{4.25}$$

In actual simulations $C_k = 2C_d$ can be used, which matches figure 4.3b with figure 4.2 for the positive filters.

The dynamic mixed and Clark model are certainly realizable if both the similarity/gradient part and the eddy-viscosity part are realizable. The previous remarks for the SEZH-model are also valid for these dynamic models. Realizability of the eddy-viscosity part requires the inclusion of an isotropic part, e.g. equation (4.22) with $C_k = 2C_d$.

4.4 Conclusions

In this chapter the turbulent stress in Large Eddy Simulation has been shown to satisfy the same realizability conditions as the well-known Reynolds stress in the statistical approach. Positiveness of the filter function is a necessary and sufficient requirement. In particular this implies that the generalised turbulent kinetic energy is positive in all regions of the flow. In view of these considerations, the top-hat and Gaussian filters are fundamentally different from the spectral cut-off filter. The first two filters (and their corresponding Favre filters for compressible flows) are positive, whereas the spectral cut-off is non-positive and, consequently, in the latter case the realizability conditions are not applicable. Indeed, the generalised turbulent kinetic energy k based on spectrally filtered fields obtained from a numerical simulation appeared to be negative in many regions of the flow. For this reason subgrid-models which predict a positive k, e.g. the gradient model, the Yoshizawa model and k-equation models, are preferred to be used in conjunction with a positive filter. Bardina's similarity model satisfies the realizability conditions for positive filters only and, consequently, this model can be used in combination with any filter. Imposing realizability for eddy-viscosity models has led to a lower bound for k. Substitution of the Smagorinsky eddy-viscosity in this inequality leads to the Yoshizawa model for compressible flow with a corresponding inequality for the model constants. This inequality can also be used to suggest a model for the isotropic term in the eddy-viscosity part of the dynamic models.

Chapter 5

Comparison of subgrid-models in LES at low Mach number

In chapter 3 six subgrid-models for the turbulent stress tensor were presented.The question which subgrid-model is most appropriate in actual Large-Eddy Simulations arises naturally. In this chapter[1] we test the models introduced in chapter 3 in LES of the temporal mixing layer at low Mach number, $M = 0.2$. The transition from laminar to developed turbulent flow is monitored and the performance of the subgrid-models is investigated in both the transitional and the turbulent regime.

The filtered Navier-Stokes equations contain subgrid-terms in the momentum and energy equation. In this chapter we focus on the modelling of the turbulent stress tensor τ_{ij} in the momentum equation. The term created by nonlinearities in the viscous stress tensor (R_i in the momentum equation) is neglected and no model for the subgrid-terms in the energy equation is assumed. In chapter 7 we will show that R_i is negligible and that for the mixing layer at low convective Mach numbers the modelling of the subgrid-terms in the energy equation has no significant effect on the Large-Eddy Simulation.

In chapter 1 we have distinguished between *a priori* and *a posteriori* testing of subgrid-models. In this chapter we follow the latter approach. LES-results of the temporal mixing layer using the six subgrid-models are presented and compared with filtered DNS-data. In the following we describe the Direct Numerical Simulation in section 5.1 and the Large Eddy Simulations in section 5.2. LES-results are compared with filtered DNS-results in section 5.3. In section 5.4 we use LES to simulate a mixing layer at high Reynolds number.

[1] This chapter is based on the papers Vreman *et al.* 1994f and 1995e.

5.1 Description of the Direct Numerical Simulation

We simulate the three-dimensional temporal mixing layer described in chapter 1. In this chapter we do not study compressibility effects, hence a low convective Mach number $M = 0.2$ is used. The Reynolds number Re based on upper stream velocity and half the initial vorticity thickness equals 50. It is sufficiently high to allow a mixing transition to small scales as observed in the incompressible simulations by Comte *et al.* (1992) and Moser & Rogers (1993). On the other hand it is sufficiently low to enable an accurate DNS that resolves all relevant turbulent scales on the computational mesh.

The Navier-Stokes equations are solved in a cubic geometry $[\ 0, L_1\ ] \times [-\frac{1}{2}L_2, \frac{1}{2}L_2\ ] \times [\ 0, L_3\ ]$. The length $L = L_1 = L_2 = L_3$ of the domain is set equal to four times the wavelength of the most unstable mode according to linear stability theory, thus allowing two subsequent pairings of two-dimensional rollers. Periodic boundary conditions are imposed in the x_1- and x_3-direction, while in the x_2-direction the boundaries are free-slip walls. The initial condition is formed by the mean profiles described in chapter 1 superimposed with two- and three-dimensional perturbation modes obtained from linear stability theory. A single mode is denoted with (α, β), where α is the streamwise and β the spanwise wavenumber. The two dimensional modes are (4,0), (2,0) and (1,0), where (4,0) is the most unstable mode with wavelength equal to $L/4$. The subharmonic modes (2,0) and (1,0) initiate vortex pairings. Three-dimensionality is introduced by adding the oblique mode disturbances (4,4), (4,-4), (2,2), (2,-2), (1,1) and (1,-1). Furthermore, random phase-shifts in the oblique modes remove the symmetry in the initial conditions. Following Moser & Rogers (1993) the amplitude of the disturbances is large (0.05 for the two-dimensional and 0.15 for the three-dimensional modes).

The DNS is conducted on a rectangular uniform grid with 192^3 cells. We use the numerical method B described in chapter 2.

Visualisation of the DNS demonstrates the roll-up of the fundamental instability and successive pairings (figure 5.1). Four rollers with mainly negative spanwise vorticity are observed at $t = 20$. After the first pairing ($t = 40$) the flow has become highly three-dimensional. Another pairing ($t = 80$), yields a single roller in which the flow exhibits a complex structure, with many regions of positive spanwise vorticity. This structure is an effect of the transition to turbulence which has been triggered by the pairing process at $t = 40$ (Moser & Rogers 1993). Hence, the flow clearly contains a cascade towards small scales and all relevant scales are accurately represented on the fine grid. The simulation is stopped at $t = 100$, since the single roller at $t = 80$ cannot undergo another pairing.

The accuracy of the simulation with 192^3 cells is satisfactory. First, the linear growth rates of the dominant instability modes are captured within one percent.

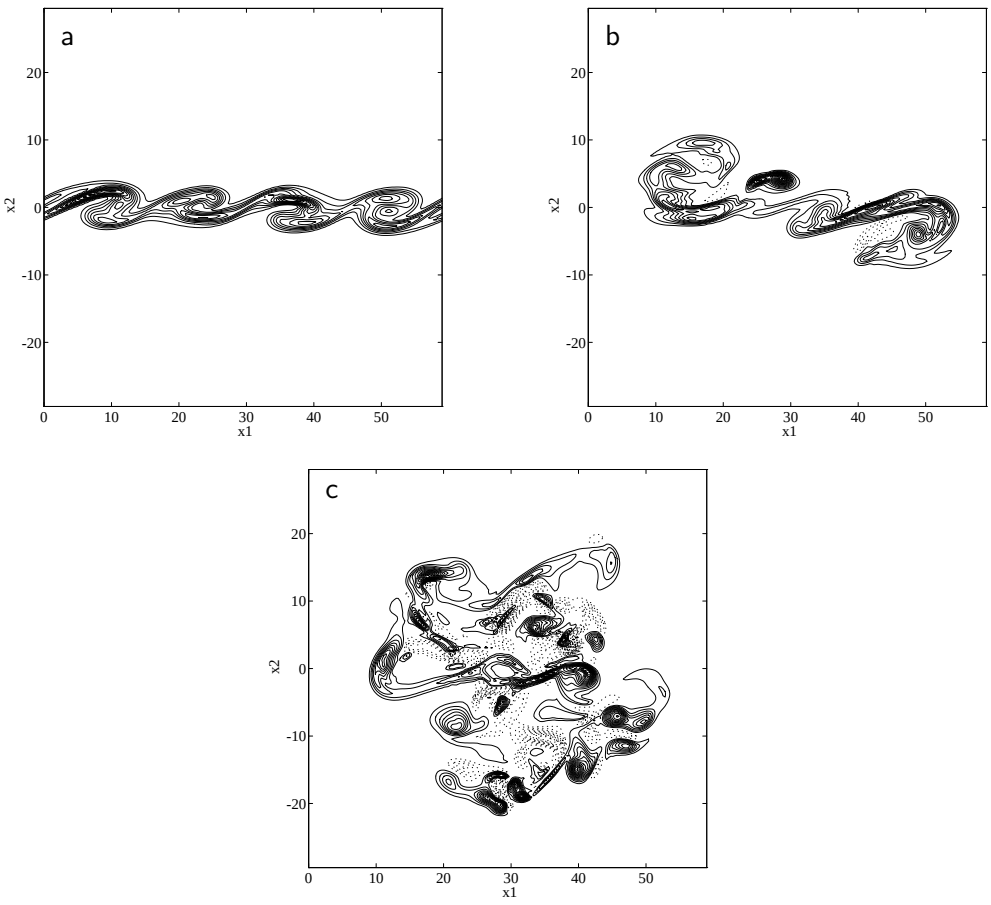

Figure 5.1: Contours of spanwise vorticity for the plane $x_3 = 0.75L$ at (a) $t = 20$, (b) t=40 and (c) t=80. Solid and dotted contours indicate negative and positive vorticity respectively. The contour increment is 0.1.

Furthermore, simulations on coarser grids have been performed, using method B with 64^3 and 128^3 cells respectively. The evolution of the momentum thickness (equation 5.7 for unfiltered variables) and an instantaneous velocity component at the centre of the shear layer are shown in figure 5.2. The resolution of the 64^3-simulation is clearly inadequate, but the results of the 128^3-simulation are quite close to those of the 192^3-simulation.

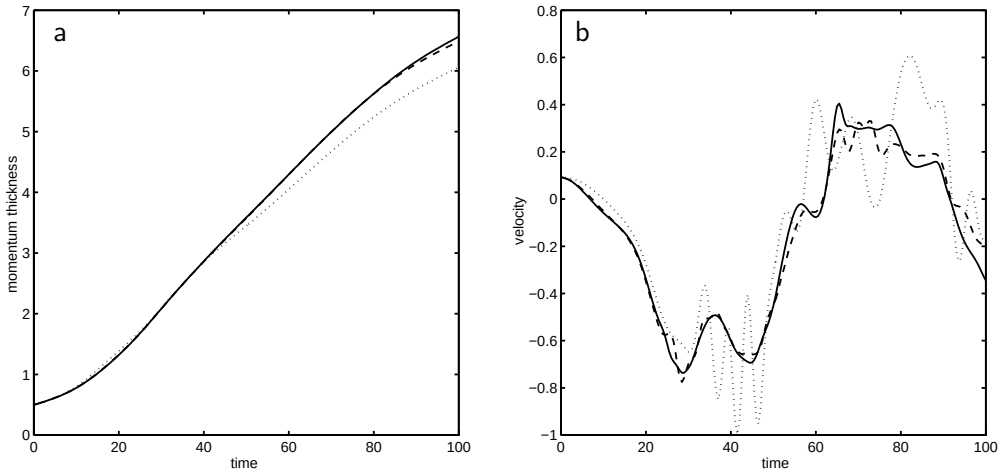

Figure 5.2: Evolution of the momentum thickness (a) and u_3 at $(\frac{1}{4}L_1, 0, \frac{1}{2}L_3)$ (b) obtained from DNS using a sequence of grids: 64^3 (dotted), 128^3 (dashed) and 192^3 (solid).

5.2 Description of the Large-Eddy Simulations

In order to perform Large-Eddy Simulations we solve the filtered Navier-Stokes equations closed with a subgrid-model for the turbulent stress tensor. The boundary conditions for the filtered variables are the same as for their unfiltered counterparts. The initial conditions are obtained by filtering the initial conditions of the DNS described above.

The specific filter adopted in the simulations is the top-hat filter. Some Large-Eddy Simulations have been repeated with the Gaussian filter and only small differences were found. The top-hat filter has appealing algebraic properties, such as positivity the turbulent stress tensor (chapter 4). It is also attractive from a numerical point of view, since the support of the filter function in physical space is relatively small. The integration which appears in the definition of the filter operation is performed with the trapezoidal rule.

The simulations are performed with a filter width $\Delta = L/16$ on a uniform grid with 32^3 cells, which is considerably coarser than the DNS-grid. Thus the filter width Δ equals twice the grid-spacing of the coarse grid, denoted by h: $\Delta = 2h$. Another option is $\Delta = h$, but in the next chapter it will be shown that the total simulation error (arising from both the modelling and the discretization) is lower for $\Delta = 2h$. The numerical scheme employed in the Large-Eddy Simulations in this chapter is method B described in chapter 2. The influence of the numerical

	model for τ_{ij}	curve
M0	0 (no model)	solid
M1	Smagorinsky	marker $*$
M2	similarity	marker $\times$
M3	gradient	marker $+$
M4	dynamic eddy-viscosity	dashed
M5	dynamic mixed	dotted
M6	dynamic Clark	dashed-dotted

Table 5.1: Subgrid-models for the turbulent stress tensor.

scheme on the simulation error will be investigated in detail in the next chapter.

A consistent comparison between LES and DNS-data requires filtering of the solution obtained with DNS. In order to obtain filtered DNS-results, the filter operation is applied to the variables on the fine grid. Next, the filtered data is easily obtained on the coarse LES-grid (being a subset of the fine DNS-grid) through restriction of the filtered fine grid data. Accurate LES-results should be close to the filtered DNS-results. Even if a 'perfect' LES-model is adopted, exact agreement between LES- and filtered DNS-results cannot be expected for all types of quantities. A number of different unfiltered initial conditions defined on a fine grid can correspond to the same filtered initial condition defined on a coarse grid. In general the Direct Numerical Simulations starting from these unfiltered initial conditions will not lead to exactly the same filtered DNS-results. The agreement between LES- and filtered DNS-results for averaged quantities is likely to be higher than for instantaneous quantities. Hence, good agreement between accurate LES- and filtered DNS-results is demanded for averaged quantities and global features, rather than for instantaneous quantities, such as the evolution of the velocity at a specific location.

Large-Eddy Simulations are performed using the six subgrid-models for τ_{ij} formulated in chapter 3. The names of the models with their abbreviations are listed in table 5.1. The abbreviation M0 corresponds to the case that τ_{ij} is simply omitted. In this case the Large-Eddy Simulation is in fact a Direct Numerical Simulation on the coarse LES-grid starting from filtered initial conditions. The case M0 is included in order to provide a point of reference for the other subgrid-models (M1-6). The performance of a specific subgrid-model is considered to be bad if the errors (deviations from the filtered DNS) are comparable to or larger than the errors corresponding to M0. In such a case the incorporation of the subgrid-model does not make sense. For most quantities the discrepancy

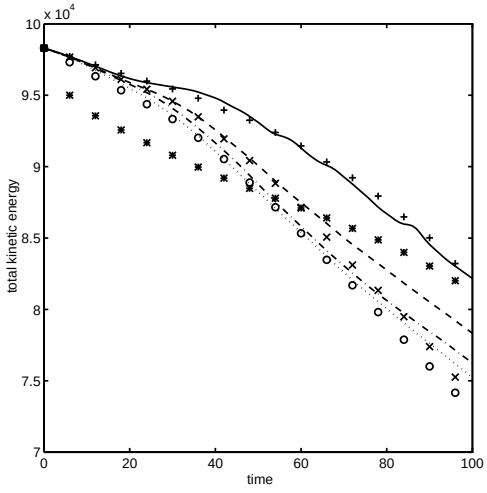

Figure 5.3: Comparison of the total kinetic energy E obtained from the filtered DNS (marker o) and from LES using M0-6 (see table 1 for labels).

between the coarse-grid simulation without subgrid-model and the filtered DNS is quite large, illustrating that there is something to improve upon; the contribution of a subgrid-model should be significant.

5.3 Comparison of results

Various quantities obtained from LES with M0-6 are shown and compared with the filtered DNS-data. We consider several aspects of the kinetic energy in detail: the evolution of total kinetic energy, turbulent and molecular dissipation, backscatter and Fourier energy spectra. The turbulent stress tensor accounts for the transfer of kinetic energy from resolved to subgrid scales. Some of the selected models adopt the eddy-viscosity hypothesis in order to approximate the energy transfer to subgrid scales. In contrast to these models, non-eddy-viscosity models (e.g. similarity) can have mechanisms to produce backscatter of energy from subgrid- to resolved scales. For these models the amount of backscatter will be calculated. Furthermore, as a local quantity the spanwise vorticity in a representative plane serves to monitor the local performance of the six models. We also investigate the evolution of the momentum thickness and various averaged statistics, e.g. Reynolds-stress profiles. In this way a number of essentially different quantities (mean, local, plane averaged) are included in the *a posteriori* tests in order to assess the quality of the models.

5.3.1 Total kinetic energy

A comparison of the subgrid-models with respect to the evolution of the total kinetic energy, based on filtered variables,

$$E = \int_\Omega \frac{1}{2}\bar{\rho}\tilde{u}_i\tilde{u}_i d\mathbf{x}, \tag{5.1}$$

is found in figure 5.3. First we discuss the Smagorinsky model M1, which gives even worse predictions than M0 provides. The total kinetic energy E for M1 is observed to exhibit a characteristic behaviour: in the transitional regime of the simulation the dissipation of energy is far too large, while it is far too low afterwards. M1 gives such an excessive dissipation in the transitional regime that transition to turbulence is hindered. The excessive dissipation caused by this model has also been observed by Piomelli *et al.* (1990a) in their study of turbulent channel flow. The other models (M2-6) are not too dissipative in the transitional regime. The M3-case gives no improvement over M0, but the models M2 and M4-6 do improve the results. In contrast to M3, no limiter is required to stabilise M2. Comparison of the curves of M2 and M0 in figure 5.3 shows that the similarity model M2 dissipates approximately the correct amount of energy. However, Bardina *et al.* (1984) report that the similarity model M2 does not dissipate energy in simulations of homogeneous turbulence with pseudo-spectral methods. We have encountered the same problem if we perform the simulation using the pseudo-spectral method C. As will be shown below, the simulation with M2 and scheme B does not provide sufficient dissipation for small scales, although the total dissipation is reasonably well predicted. The pseudo-spectral method appears to be more sensitive to the presence of small scales on a relatively coarse grid than the finite difference method B. The results for M4, the dynamic eddy-viscosity model by Germano *et al.*, illustrate that the dynamic adjustment of the model coefficient meets the major short-coming of Smagorinsky's model, being the excessive dissipation in the transitional regime. Indeed the results are much better than those of M1. The dynamic mixed model M5 and the dynamic Clark model M6 both accurately predict the evolution of E. Within the group of models considered, M5 most closely approaches the filtered DNS-results.

5.3.2 Turbulent and molecular dissipation

The decay of the total kinetic energy, E, is described by the following partial differential equation:

$$\partial_t E = \int_\Omega (P_d - \epsilon_\mu - \epsilon_{\text{sgs}}) d\mathbf{x}, \tag{5.2}$$

where

$$P_d \;=\; \bar{p}\partial_k\tilde{u}_k, \tag{5.3}$$

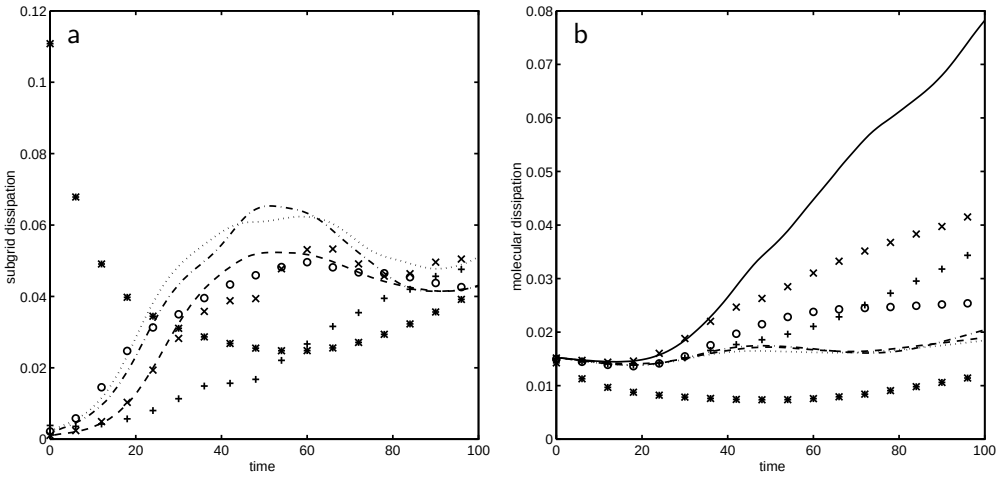

Figure 5.4: Comparison of the subgrid-scale dissipation $\int_\Omega \epsilon_{\text{sgs}} d\mathbf{x}$ (a) and molecular dissipation $\int_\Omega \epsilon_\mu d\mathbf{x}$ (b) obtained from the filtered DNS (marker o) and from LES using M1-6 (see table 1 for labels).

$$\epsilon_\mu = \mu(\tilde{T}) S_{ij}(\tilde{\mathbf{u}}) \partial_j \tilde{u}_i, \tag{5.4}$$

$$\epsilon_{\text{sgs}} = -\bar{\rho} \tau_{ij} \partial_j \tilde{u}_i. \tag{5.5}$$

In our case the contribution of the pressure dilatation P_d can be neglected, since the flow is almost incompressible. The molecular dissipation, ϵ_μ, is always positive due to the equality $S_{ij}(\tilde{\mathbf{u}})\partial_j \tilde{u}_i = \frac{1}{2} S^2_{ij}(\tilde{\mathbf{u}})$. The subgrid dissipation, ϵ_{sgs}, represents the amount of energy transferred from resolved to subgrid scales, which is positive if an eddy-viscosity model is adopted for τ_{ij}. For non-eddy-viscosity models, however, this term can be positive or negative, referring to forward or backscatter of subgrid-scale kinetic energy respectively. Backscatter produced by subgrid-models is sometimes hard to control within a simulation and can lead to numerical instability. From the models we consider, the gradient model (M3), as formulated in equation (3.12) leads to instabilities and, for this reason, backscatter in M3 is artificially prevented, with the use of a limiter (see chapter 3).

Thus, the decay of total kinetic energy is caused by both subgrid-scale and molecular dissipation. The subgrid-scale dissipation and molecular dissipation integrated over the domain are shown in figure 5.4. Simulation M0 is not found in figure 5.4a; it has no subgrid-scale dissipation, since no subgrid-model is adopted. Figure 5.4a clearly reveals the excessive dissipation of M1 in the transitional regime. For the other models the subgrid-scale dissipation is initially small, whereas it grows when the flow undergoes the transition to turbulence. Fur-

thermore, M2 (without limiter) and M3 (with limiter) are observed to dissipate energy, although these models do not employ an eddy-viscosity. Compared to the filtered DNS-results, the subgrid dissipation is reasonably well predicted by M2 and M4-6.

The simulations that employ an eddy-viscosity (M1, M4-6) produce an almost constant level of molecular dissipation, whereas the molecular dissipation increases and becomes too large for M0, M2 and M3. The presence of too many small scales leads to the over-predicted molecular dissipation in the latter cases. Obviously, the simulation with M0 contains too many small scales, since there is no energy transfer to subgrid scales by a model. As will be shown in section 5.3.4, the simulations with M2-3 also contain too many small scales. The amount of small-scale energy dissipated by the subgrid-model is insufficient in cases M2 and M3.

The molecular dissipation takes over part of the work that should be performed by the subgrid-models M2 and M3. This further explains features of the behaviour of M2 and M3 in figure 5.3. In figure 5.3 the evolution of E for M3 is approximately the same as for M0, although, according to figure 5.4a, M3 provides some dissipation. However, the molecular dissipation for M0 is higher than for M3 (figure 5.4b); consequently both simulations are almost equally dissipative. Furthermore, the subgrid dissipation is comparable for M2 and M4, although the total energy decay is stronger for M2. The molecular dissipation explains this behaviour; it is much higher for M2, due to the presence of more small scales.

With respect to the dynamic models M4-6 the subgrid dissipation in the turbulent regime is best approximated by M4. The molecular dissipation is for all three models somewhat too small. The subgrid dissipation for M5-6 is somewhat too large. Consequently, the total energy decay for M5-6 is approximately correct and better than for M4. These cancelling of errors in subgrid and molecular dissipation will not occur in flows at very high Reynolds number, since in such flows the molecular dissipation is negligible compared to the subgrid dissipation. From the curves in figures 5.4 for the filtered DNS-results and M4-6, it is inferred that in the turbulent regime of this flow the ratio between subgrid-scale dissipation and molecular dissipation is about two to three, which is comparable to ratios reported in Piomelli *et al.* (1990b). Although this mixing layer contains a mixing transition to small-scale turbulence, the Reynolds number is relatively low. The molecular dissipation of resolved scales (ϵ_μ) will decrease if the Reynolds number is increased. A larger part of the dissipation will occur at subgrid scales since dissipation essentially is a small-scale phenomenon. Thus in high Reynolds number LES the somewhat over-predicted subgrid dissipation of M5-6 will not be compensated by the under-predicted molecular dissipation. Hence, in high

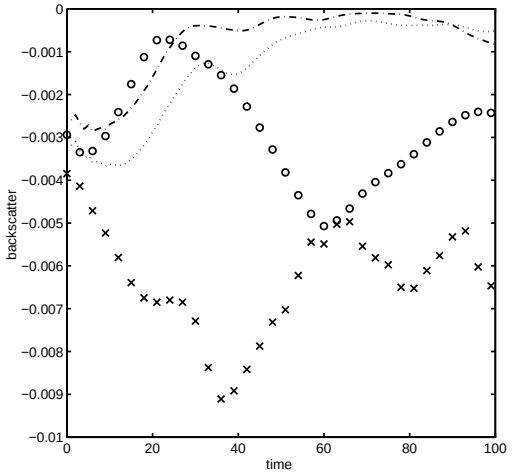

Figure 5.5: Comparison of the amount of backscatter obtained from the filtered DNS (marker o) and from LES using M2, M5 and M6 (see table 1 for labels).

Reynolds number LES the total dissipation process in the turbulent regime is possibly best predicted by M4 (see section 5.4).

5.3.3 Backscatter

The amount of backscatter produced by several subgrid-models is addressed next. The eddy-viscosity models M1 and M4 do not produce backscatter since the model coefficient in M1 is a positive constant by definition and the dynamic model coefficient in M4 is restricted to positive values in order to ensure numerical stability. Moreover, the limiter concept in M3 artificially removes the backscatter from this model. Therefore, the only models which produce backscatter are M2, M5 and M6. For these two models the total amount of backscatter, defined as

$$\int_{\Omega} \min(\epsilon_{\text{sgs}}, 0) d\mathbf{x}, \tag{5.6}$$

is plotted in figure 5.5. Since M5-6 incorporate an eddy-viscosity, these models produce less backscatter than M2. The amount of backscatter for M5-6 is relatively low in the turbulent regime, where the eddy-viscosity part of the model is more important than in the transitional regime. A comparison with the filtered DNS-results shows that M2 produces too much backscatter, whereas M5-6 do not produce enough backscatter. Except in the early stages of the simulation, the amount of backscatter is only a small fraction of the forward scatter (about 10

percent for the filtered DNS-results). *A priori* tests of transitional and turbulent channel flow show comparable back- and forward scatter for the spectral cut-off filter, but smaller back- than forward scatter for the top-hat and Gaussian filters (Piomelli *et al.* 1990b). Here *a posteriori* tests of the mixing layer demonstrate that in the filtered DNS on a coarse grid and in actual LES with the top-hat filter the structure of the turbulent flow is such that the amount of backscatter is relatively small. In a recent study on dynamic LES of isotropic turbulence, taking backscatter into account did not significantly influence the results either (Carati *et al.* 1995).

Others decompose the subgrid dissipation ϵ_{sgs} into a mean and a fluctuating part (Jiménez-Härtel 1994, Horiuti 1995) and find that the amount of backscatter in the fluctuating part is relatively large. In this subsection we focussed on the importance of backscatter relative to the full dissipation of energy to subgrid scales.

5.3.4 Energy spectrum

We mentioned that the increase in molecular dissipation observed for M0, M2 and M3 was due to the presence of small scales. This is further clarified by examination of the energy spectrum at a certain time and the time evolution of specific small- and large-scale components of the spectrum. Figure 5.6 contains the streamwise kinetic energy spectrum in the turbulent regime at $t = 80$, denoted by $A(k)$, where k is the streamwise wavenumber. The spanwise energy spectrum exhibits similar features. The filtered DNS-result does not contain an inertial range displaying the -5/3-law, because the spectrum is based on the filtered velocity and the Reynolds number is relatively low in order to enable DNS. The spectrum of the filtered DNS is in good agreement with those of the dynamic models M4 and M5, with a slight preference for M5. The spectrum for the third dynamic model (M6) is too large for the highest wavenumbers. Furthermore, we observe that the simulation with M1 is not able to generate the desired amount of small scales. On the other hand, the contributions of high wavenumbers are too high for M0, M2 and M3 and, consequently, these simulations contain too many small-scale contributions. This had to be expected for M0, having no subgrid-model, whereas this result indicates insufficient energy dissipation of small scales for the models M2 and M3.

The time evolution of a specific small-scale contribution, $A(10)$, has been plotted in figure 5.7a. This figure reflects that the previous remarks about small-scale generation are valid for other times as well. The immediate occurrence of small scales for model M3 has been analytically explained in chapter 3.

In figure 5.7b a specific large-scale contribution, $A(1)$, is shown. The dynamic mixed model M5 is the best approximation of the DNS-result (note that the

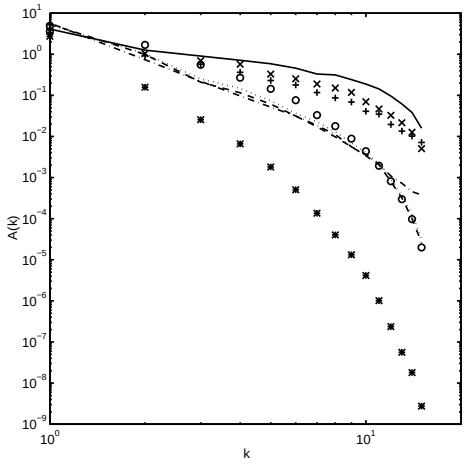

Figure 5.6: Comparison of the streamwise energy spectrum $A(k)$ at $t = 80$ obtained from the filtered DNS (marker o) and from LES using M0-6 (see table 1 for labels).

logarithm has been plotted). This figure further illustrates the behaviour of the similarity model M2. On the one hand too many small scales are present due to insufficient dissipation of these scales. On the other hand, the amount of large scales is too low, indicating too much dissipation for large-scale structures. Thus it can be explained that the dissipation of total energy, which contains large and small-scale contributions is reasonable for M2 (figures 5.3-4).

5.3.5 Spanwise vorticity in a plane

The spanwise vorticity component is often used to visualise the large-scale roller structure in mixing layers at low Mach number. In figure 5.1 we have visualised the scenario of the DNS: four rollers of spanwise vorticity at $t = 20$, two at $t = 40$ and one at $t = 80$. During these pairing processes the mixing layer undergoes a transition to turbulence and many small regions of spanwise vorticity of both signs occur. In the Large-Eddy Simulations this scenario is reproduced in nearly all cases (M0, M2-6). Only the simulation with the Smagorinsky model M1 is an exception; instead of four rollers at $t = 20$ only two rollers form, indicating that the linear instability process is highly affected by the excessive dissipation caused by M1. Figures 5.8-9 display the spanwise vorticity at $t = 80$ in the plane $x_3 = 0.75L_3$ for the filtered DNS restricted to the coarse grid and for M0-6. First, we compare the filtered DNS-result in figure 5.8a with the unfiltered DNS-result in figure 1c, which corresponds to the same time and plane and has

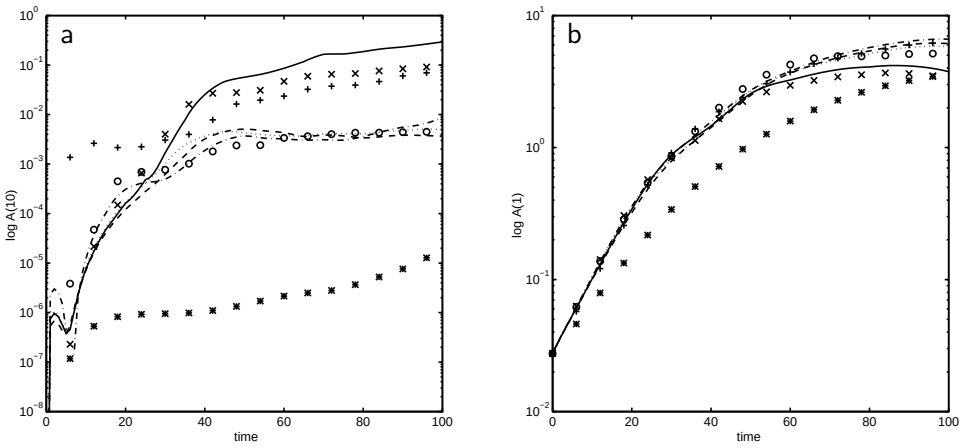

Figure 5.7: Comparison of the evolution of the $A(10)$-component (a) and the $A(1)$-component of the energy spectrum obtained from the filtered DNS (marker o) and from LES using M0-6 (see table 1 for labels).

the same contour increment. Obviously, the smallest structures are removed by the filtering and the peak values of the vorticity are considerably reduced. The vorticity field of the filtered variables can successfully be represented on the coarse grid. Furthermore, the amount of positive spanwise vorticity in the filtered case is smaller than in the unfiltered result. We conclude that most structures of positive spanwise vorticity in the DNS are smaller than the filter width Δ, thus being subgrid scales on the LES-grid.

In the following, we turn to the LES-predictions M0-6 in figures 5.8b-d and 5.9, which ideally should resemble the filtered DNS-result in figure 5.8a. The simulation with no subgrid-model (figure 5.8b), contains too many small-scale structures and the peak intensities are too large. The physical dynamics of such small-scale structures clearly cannot be correctly captured on the coarse 32^3-grid. On the other hand the result in figure 5.8c, corresponding to the Smagorinsky model M1, is too smooth; it contains mainly large-scale structures. The two rollers produced at $t = 20$ (instead of four) have slowly started to pair at $t = 80$, but no transition to smaller scales occurs and the mixing layer is much too thin. Like M0, the similarity model (M2; figure 5.8d) and gradient model (M3; figure 5.9a) give rise to an excessive number of small structures and regions of positive spanwise vorticity. This is in agreement with the energy spectra in figure 5.6, in which the contributions at high wavenumbers are too large. Furthermore, the vorticity distribution of M2 is quite similar to M0, only the peak intensities for

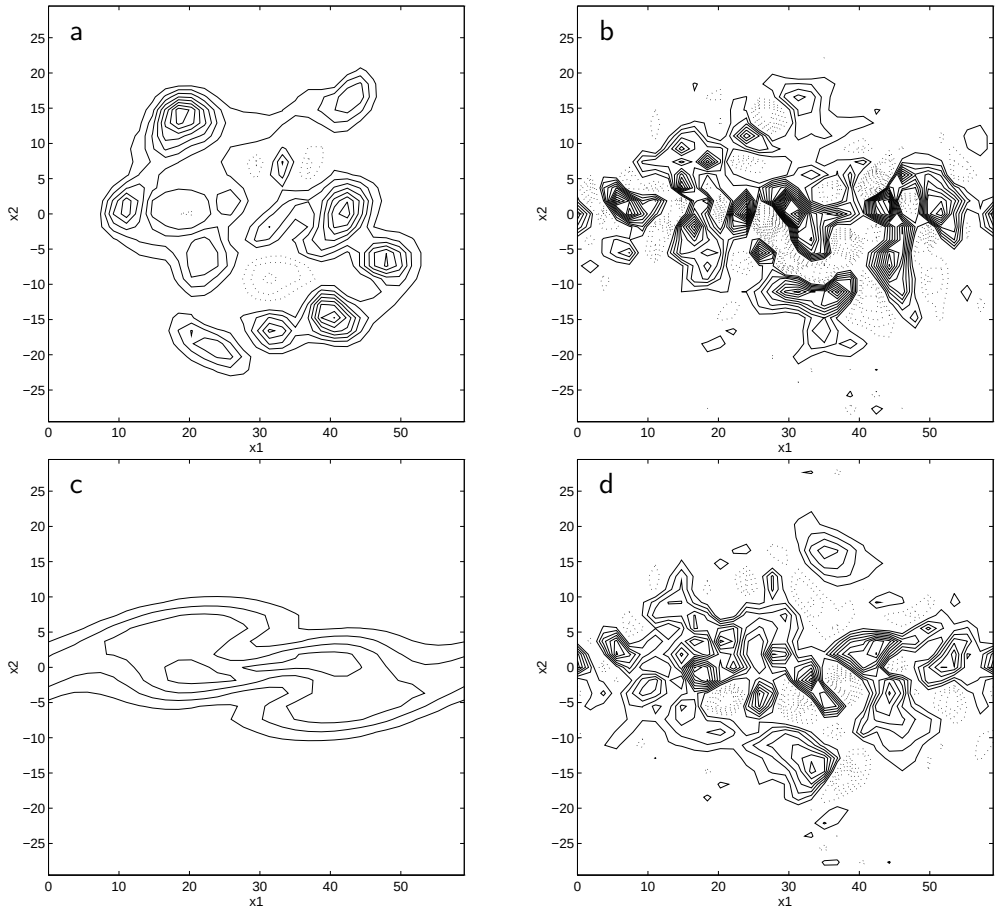

Figure 5.8: Contours of spanwise vorticity for the plane $x_3 = 0.75L$ at t=80 obtained from (a) the filtered DNS, restricted to the 32^3-grid, and from LES using (b) M0, (c) M1 and (d) M2. Solid and dotted contours indicate negative and positive vorticity respectively. The contour increment is 0.05.

M2 are weaker. Figure 5.9a clearly shows that M3 under-predicts the thickness of the layer.

The vorticity obtained with the dynamic models (M4-6 in figure 5.9b-d) is qualitatively in better agreement with the filtered DNS-results than the previous plots. The peak values of the vorticity are quite well predicted and almost the correct amount of small structures is present. With respect to the dynamic models, M5 is preferred over M4 and M6. The thickness of the mixing layer is better predicted than by M4. Furthermore, compared to M4 and M6, more regions of positive spanwise vorticity are present and the negative regions are less connected, which is in agreement with figure 5.8a. Hence, M5 yields the best

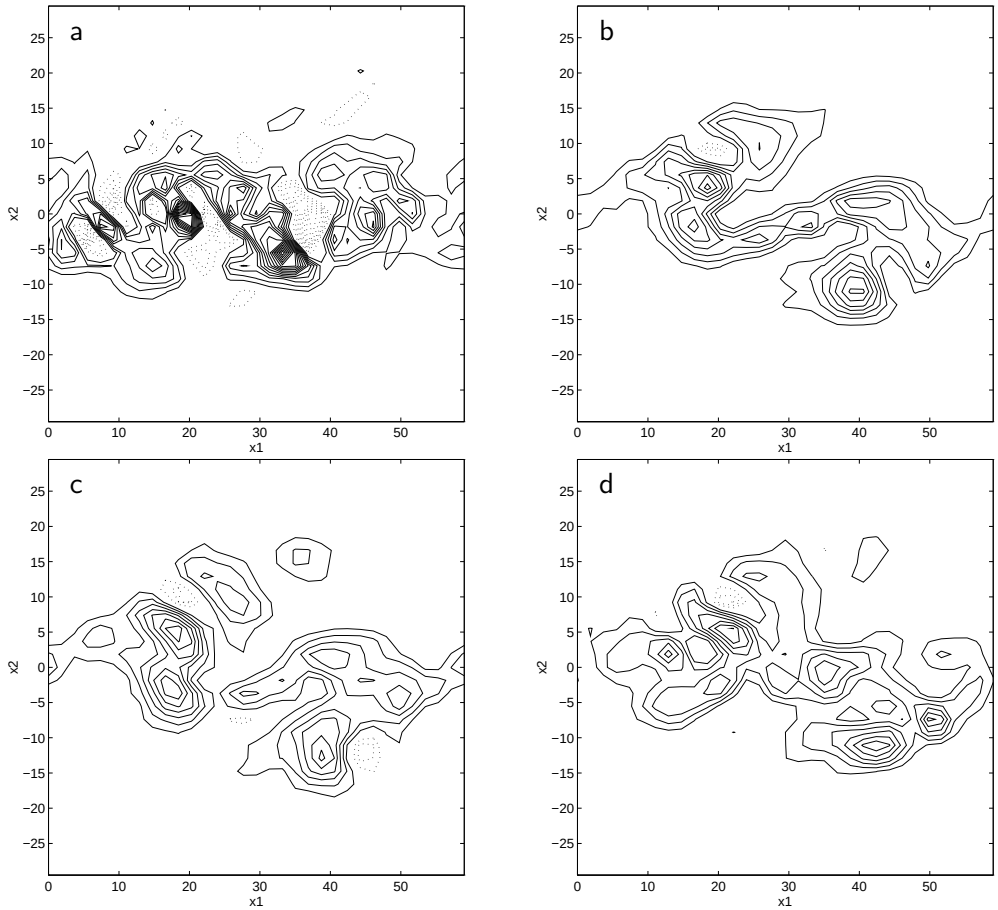

Figure 5.9: Contours of spanwise vorticity for the plane $x_3 = 0.75L$ at t=80 obtained from LES using (a) M3, (b) M4, (c) M5 and (d) M6. Solid and dotted contours indicate negative and positive vorticity respectively. The contour increment is 0.05.

qualitative agreement with the filtered DNS. As explained in section 5.2 detailed agreement between LES and filtered DNS on a local instantaneous level is not required.

5.3.6 Positive spanwise vorticity

The occurrence of positive spanwise vorticity in the mixing layer is related to the transition to turbulence. Due to the mean profile, the spanwise vorticity is initially negative in the whole domain. In the two-dimensional case such an initial condition implies that the (spanwise) vorticity remains negative throughout the simulation. Apart from compressibility effects, only the 'vortex-stretching' term in the vorticity equation can increase the global maximum of a vorticity

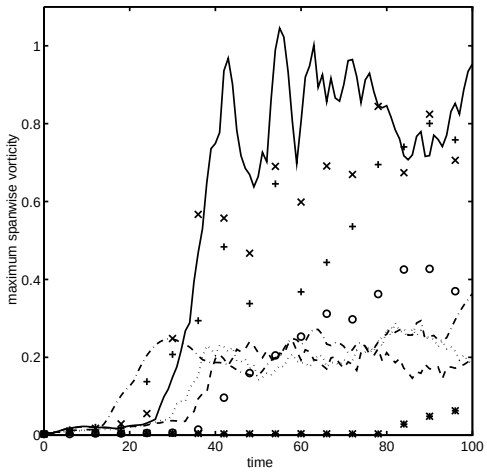

Figure 5.10: Comparison of the spatial maximum of positive spanwise vorticity as a function of time obtained from the filtered DNS (marker o) and from LES using M0-6 (see table 1 for labels).

component. Vortex-stretching is essential in the generation of turbulence. From examining the evolution of the maxima (or minima) of vorticity components it can be inferred whether this mechanism is present in the flow.

In figure 5.10 the evolution of the maximum of the spanwise vorticity is shown for the various simulations considered. The filtering strongly reduces the DNS-values for this quantity, as is observed from a comparison of figures 5.1c and 5.8a, but figure 5.10 shows that the sudden increase of positive spanwise vorticity is also present in the filtered DNS. The models M0, M2 and M3 over-predict this quantity, since in these simulations there are too many small-scale contributions. On the other hand, in the simulation with M1 no positive spanwise vorticity is generated for a long time, corresponding to the absence of strong vortex-stretching. This result again illustrates that the Smagorinsky model hinders the transition to turbulence. The dynamic models M4 and M5 both give predictions which are relatively close to the filtered DNS-results, whereas the increase of positive spanwise vorticity starts too early for M6.

5.3.7 Momentum thickness

From figures 5.8-9 we have already observed that the thickness of the mixing layer depends on the subgrid-model. This dependence is further clarified in figure 5.11,

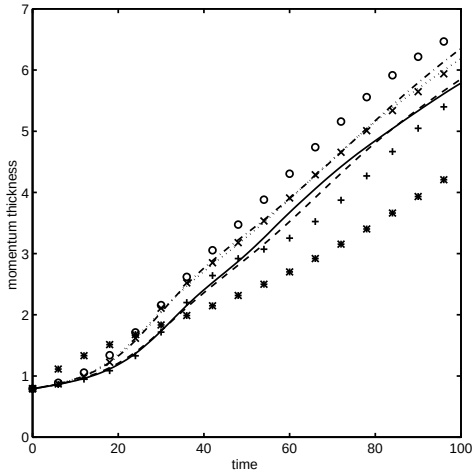

Figure 5.11: Comparison of the momentum thickness obtained from the filtered DNS (marker o) and from LES using M0-6 (see table 1 for labels).

in which the evolution of the momentum thickness, based on filtered variables,

$$\delta = \frac{1}{4}\int_{-L/2}^{L/2} < \bar{\rho} > (1 - \frac{< \bar{\rho}\tilde{u}_1 >}{< \bar{\rho} >})(\frac{< \bar{\rho}\tilde{u}_1 >}{< \bar{\rho} >} + 1)dx_2, \tag{5.7}$$

is shown. The operator $< . >$ represents an averaging over the homogeneous directions x_1 and x_3. Since the definition of the momentum thickness employs the mean velocity profile, tests for the momentum thickness quantify the spreading of the mean velocity profile. Figure 5.11 displays a short period of laminar growth (until $t = 20$), followed by a period in which the mixing layer grows considerably faster, visualising the increased mixing caused by turbulence.

The models M1 and M3 lead to worse predictions for the momentum thickness than M0, indicating that with respect to this quantity LES without a subgrid-model is preferred over adopting M1 or M3. The slow growth of the momentum thickness for M1 further establishes the observation that this model hinders the transition to turbulence. The results for M4 are quite similar to M0, whereas the models M2, M5 and M6 clearly yield improvement over M0 and are relatively close to the filtered DNS-result. It is remarkable that the evolution of the momentum thickness is almost identical for M2 and M5. This indicates that for the momentum thickness the improvement over M0 is mainly due to the similarity model, since the eddy-viscosity part of M5 does not seem to affect this quantity. Other evidence for the small effect of the dynamic eddy-viscosity on the momentum thickness is that the curves for M0 and M4 almost coincide. However, the

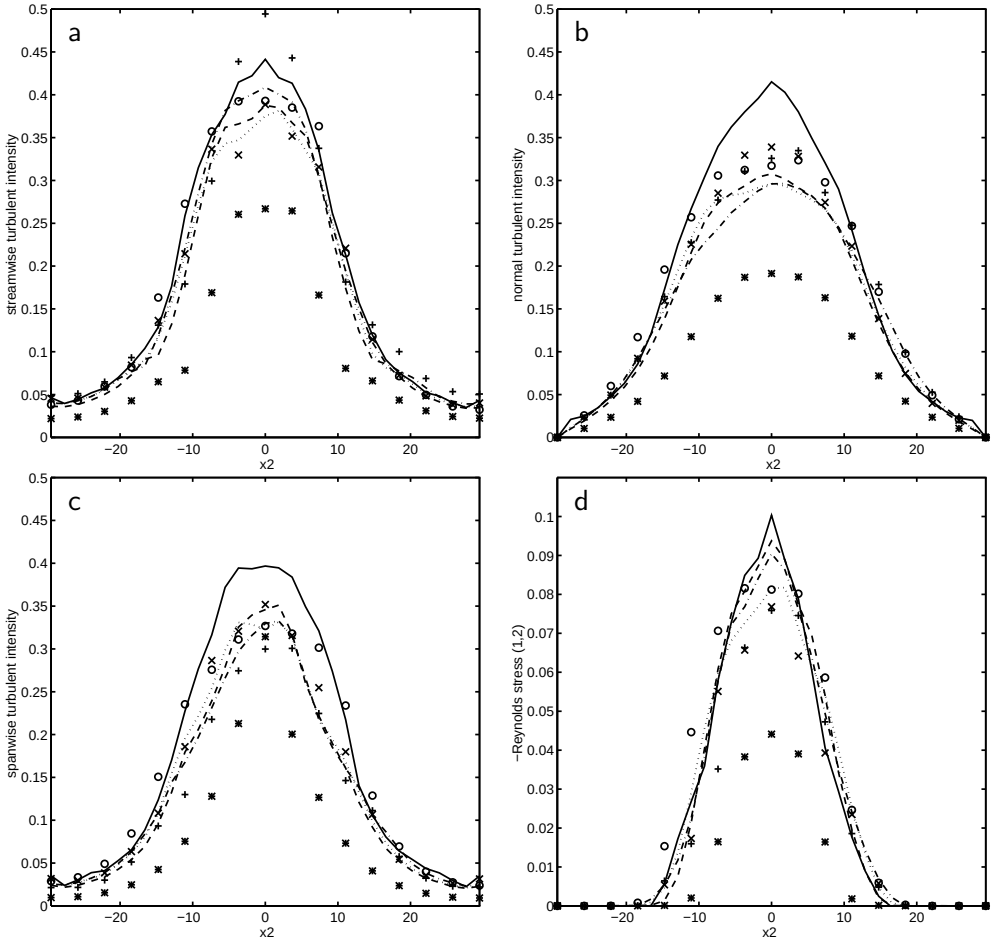

Figure 5.12: Comparison of the profiles of the turbulent intensities $< \bar{\rho} v_i^2 >^{1/2}$ for $i = 1, 2, 3$ (a,b,c) and the Reynolds stress $- < \bar{\rho} v_1 v_2 >$ (d) at $t = 70$ obtained from the filtered DNS (marker o) and from LES using M0-6 (see table 1 for labels).

similarity model already plays a role in the early stages of transition. The time at which the increased mixing starts is relatively early compared to M0. This behaviour is confirmed by the finding that growth rates of linear instability waves are increased by the similarity model and are also closer to the correct values.

5.3.8 Profiles of averaged statistics

Finally, we will compare x_2-profiles of various statistics averaged in the homogeneous directions. These profiles will be calculated at $t = 70$, which is

	figure	M1	M2	M3	M4	M5	M6
total kinetic energy	5.3	−	+	−	0	++	+
subgrid dissipation	5.4a	−	+	−	++	+	+
molecular dissipation	5.4b	−	+	+	+	+	+
backscatter	5.5	−	0	−	−	0	0
energy spectrum $A(k)$	5.6	−	−	−	+	++	0
component $A(10)$	5.7a	−	−	−	+	+	+
component $A(1)$	5.7b	−	−	+	+	+	0
vorticity in a plane	5.8-9	−	−	−	+	++	+
maximum vorticity	5.10	−	−	−	+	+	0
momentum thickness	5.11	−	+	−	−	+	++
$< v_1 v_1 >^{1/2}$	5.12a	−	+	−	+	+	++
$< v_2 v_2 >^{1/2}$	5.12b	−	+	+	+	+	+
$< v_3 v_3 >^{1/2}$	5.12c	−	+	0	+	+	+
$-< v_1 v_2 >$	5.12d	−	−	−	0	++	+

Table 5.2: Summary of the results for M1-6. The symbols −,0 and + refer to bad, reasonable and good results, respectively. Furthermore, ++ is better than +.

well beyond the starting point of the mixing transition process, but just before the final pairing has been accomplished. In the definition of these profiles, $v_i = \tilde{u}_i - < \bar{\rho}\tilde{u}_i > / < \bar{\rho} >$ denotes a fluctuating velocity field. In figure 5.12a-c the turbulent intensities $< \bar{\rho} v_i^2 >^{1/2}$ are shown for $i = 1, 2, 3$. The filtered DNS-results demonstrate that the streamwise intensity is somewhat larger than the normal and spanwise intensities. The turbulent intensities are too large for M0, while they are under-predicted by M1. The model M3 gives reasonable predictions for $i = 2$, but the peak for $i = 1$ is much too high, whereas the spreading for $i = 3$ is too low. The remaining three models (M2, M4-6) are equally accurate; the global discrepancies with the filtered DNS-results are approximately the same, although for $i = 1$ M6 is slightly better than the other models. With respect to the Reynolds stress profile $-< \bar{\rho} v_1 v_2 >$, shown in figure 5.12d, the dynamic mixed model M5 has to be preferred, since it provides the most accurate approximation of the filtered DNS-profile.

5.3.9 Summary

Table 5.2 summarises the results for the subgrid-models M1-6. The discrepancy with the filtered DNS determines the quality of the result. In general, a result

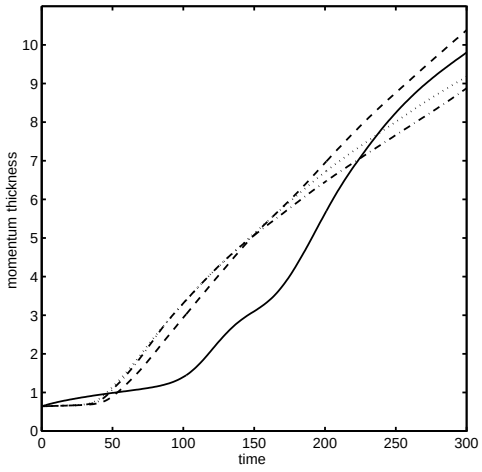

Figure 5.13: Evolution of the momentum thickness $\delta(t)$ obtained from using M1 (solid), M4 (dashed), M5 (dotted) and M6 (dashed-dotted).

for a given subgrid-model is considered to be bad if its discrepancy with the filtered DNS is larger than the discrepancy between the filtered DNS and M0. If within a group of models that provide good results denoted by '+', one model performs even better than the other models, this model is labelled with '++'. Simulations with M2 and M4-6 do give considerable improvements over M0; the incorporation of these models is useful in LES of the mixing layer. Within the group of these four models, the dynamic mixed model provides the most accurate results, compared to the filtered DNS results. Table 5.2 further shows that with respect to overall accuracy M6 is next to M5, then M4 and then M2.

The resolution of 32 grid-points in the normal direction on a uniform grid might seem too coarse for the representation of the mean profile. However, it has to be noticed that according to the definition of the initial conditions in LES, *filtered* mean profiles are used, which are smoother than the original mean profiles. The instability resulting from this profile is essentially the same as in the filtered DNS, since for all models considered (except for M1) LES was observed to reproduce the four-roller structure that results from the primary instability. Furthermore, the flow structure in the turbulent regime (e.g. figures 5.1c, 5.8-9) suggests the choice of equal grid-sizes in all three directions. The results in this chapter show that LES on the 32^3-grid is in satisfactory agreement with the filtered DNS, provided an appropriate subgrid-model is used.

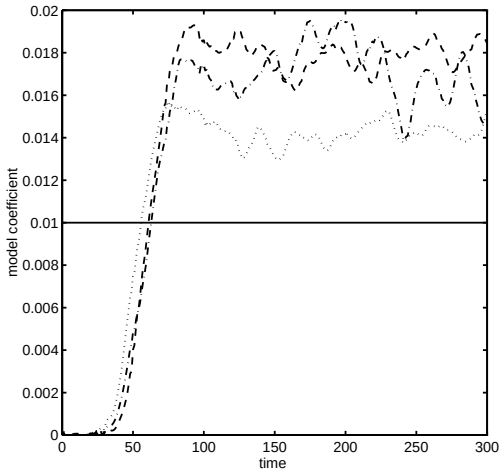

Figure 5.14: The dynamic model coefficient C_d at $x_2 = 0$ in LES with M4 (dashed), M5 (dotted) and M6 (dashed-dotted), and the value of C_S^2 in M1 (solid).

5.4 LES at high Reynolds number

In this section we perform LES of the temporal mixing layer at high Reynolds number using the subgrid-models M0-6 and investigate whether the flow becomes self-similar. Although the simulation described in section 5.1 contained a transition to small scales, the size of the domain allowed two successive pairings only and the Reynolds number was relatively low (50) in order to enable DNS. Compared to DNS, LES should be able to simulate flows in a larger domain and at higher Reynolds number at the same computational cost.

The temporal mixing layer in this section is simulated at $M = 0.2$ and $Re = 500$, based on the reference values defined in section 1.2. The calculation is performed on a grid with 120^3 cells and the computational domain is large, $L_1 = L_2 = L_3 = 120$. This size is equal to eight times the wave length of the fundamental linear instability. Hence, the flow allows three successive pairings before it saturates. Uniform noise is used to perturb the initial mean flow (amplitude 0.05 and multiplied with $e^{-x_2^2/4}$), in contrast to section 5.1 where an eigenfunction perturbation was used. The Large-Eddy Simulations employ the top-hat filter with the basic filter width equal to twice the grid-spacing.

At this Reynolds number there are no DNS-results to compare with, but we can verify whether the flow is self-similar. A temporal mixing layer is self-similar if the development of the shear layer thickness is linear in time and profiles of normalised statistical quantities at different times coincide (Rogers & Moser

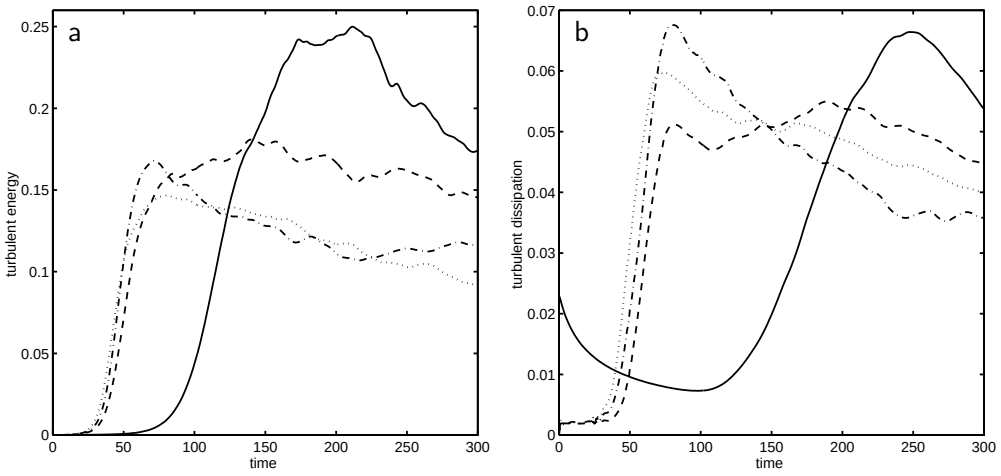

Figure 5.15: Evolution of the turbulent energy $\frac{1}{2}R_{qq}$ at $x_2 = 0$ (a) and dissipation $\int < \epsilon > dx_2$ (b) obtained from LES with M1 (solid), M4 (dashed), M5 (dotted) and M6 (dashed-dotted).

1994). The common opinion is that mixing layers should display self-similar behaviour, provided the Reynolds number is high, the computational domain is large and the simulation is performed sufficiently far in time.

The evolution of the momentum thickness is shown in figure 5.13 for the subgrid-models M1 and M4-M6. None of the simulations is fully self-similar, since in each case the momentum thickness curve is not perfectly straight in the turbulent regime. The most self-similar case is obtained with the dynamic eddy-viscosity model M4, where $\delta(t)$ is approximately linear between $t = 100$ and 250. The other two dynamic models, M5 and M6 lead to a faster growth than M4 between $t = 40$ and 130, but to a lower growth afterwards.

The results for M1 in the previous section were obtained using a Smagorinsky constant of 0.17 (Lilly 1967, Schumann 1991). Since the model was observed to be too dissipative and to hinder the transition to turbulence, the M1-simulation in this section uses a lower coefficient, $C_S = 0.10$. This value was proposed by Deardorff (1970) in LES of turbulent channel flow, whereas Moin & Kim (1982) used an even lower value. Compared to the dynamic models, M1 with $C_S = 0.10$ is still too dissipative in the first part of the simulation. The shear layer displays a strong growth in the laminar regime, indicating that $C_S = 0.10$ is too large in the laminar regime. Although the model does not prevent the transition to turbulent flow, the transition is delayed and the sudden growth of the momentum thickness starts relatively late (at $t = 100$). After transition has occurred, the

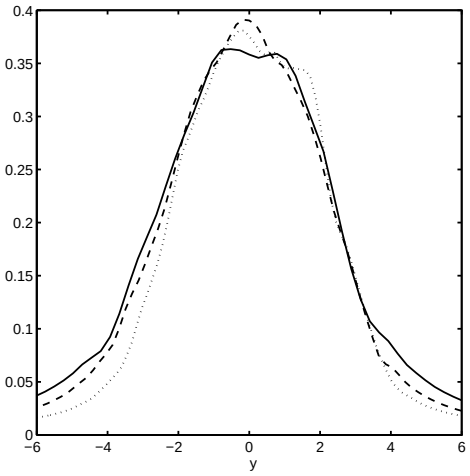

Figure 5.16: Profiles of the streamwise r.m.s. velocity fluctuation versus $y = x_2/\delta(t)$ at $t = 120$ (solid), $t = 160$ (dashed) and $t = 200$ (dotted).

shear layer growth is too strong compared to the dynamic models, indicating that the value $C = 0.10$ in the turbulent regime is too small. Furthermore, the momentum thickness predicted by M1 does not increase linearly in the turbulent regime, showing that the mixing layer is not self-similar.

Results for M0, M2 and M3 are not shown, because the simulations with these models become unstable before $t = 100$ and, therefore, cannot be completed. The reason is the insufficient dissipation from resolved to subgrid scales. We have noticed too much energy in the small scales in the simulations at lower Reynolds number (section 5.3.4) and this leads to unstable simulations at high Reynolds number.

The evolution of the dynamic model coefficients at $x_2 = 0$ is shown in figure 5.14 together with the value of C_S^2 in M1. Indeed, $C_S = 0.1$ is initially too high, but too low in the turbulent regime. The Smagorinsky coefficient corresponding to the average value of the dynamic coefficient of M4 in the turbulent regime would be $C_S = 0.13$. The eddy-viscosities in M5-6 model a part of the turbulent stress tensor only and therefore the dynamic coefficients in M5-6 are lower than in M4. However, in this case the differences between the model coefficients of M4-6 are smaller than at low Reynolds number (Vreman *et al.* 1994b), which implies that incorporation of a similarity or gradient part is less useful in the prediction of the subgrid dissipation if the Reynolds number is high.

Statistical quantities are self-similar if profiles at different times coincide after the appropriate normalisation. In the following we consider the Reynolds stress

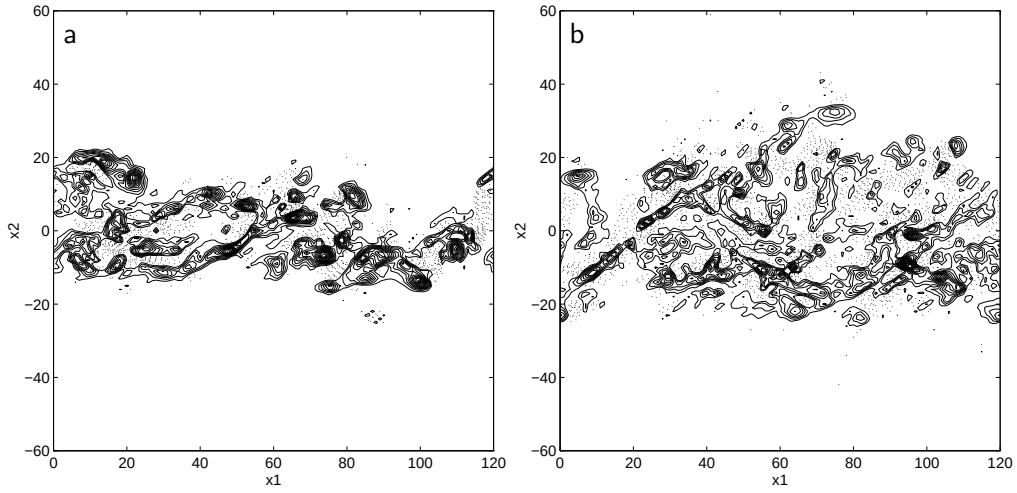

Figure 5.17: Positive (dotted) and negative (solid) contours of spanwise vorticity in the plane $x_3 = 90$ at $t = 160$ (a) and $t = 240$ (b). The contour increment equals 0.05.

profiles, $R_{ij} =< \bar{\rho} v_i v_j >$, with v_i defined as in subsection 5.3.8, and the dissipation profile $< \epsilon >=< \epsilon_{\rm sgs} + \epsilon_\mu >$, with $\epsilon_{\rm sgs}$ and ϵ_μ defined as in subsection 5.3.2. These profiles are functions of time and the normal direction x_2, which scales with $\delta(t)$. The Reynolds stress tensor and the dissipation can be scaled by $\rho_1(\Delta U)^2$ and $\rho_1(\Delta U)^2/\delta(t)$ respectively, where ρ_1 is the upper free stream and ΔU is the velocity difference between the free streams.

The turbulent kinetic energy $\frac{1}{2}R_{qq}$ at $x_2 = 0$ and the integrated dissipation $\int < \epsilon > dx_2$ are shown in figure 5.15. In self-similar flow these quantities should not depend on time. From these figures it appears that an approximate self-similar state is best reached by M4. Due to the finite size of the computational domain the statistics are expected to decay after some time, but compared to M4 the decay starts relatively early for M5-6. The somewhat over-predicted subgrid dissipation by M5-6 noticed in subsection 5.3.2 is a possible reason for the relatively early decay. In these Large-Eddy Simulations at high Reynolds number, the fraction of the dissipation due to molecular viscosity is low (less than 10% in the turbulent regime).

Figure 5.16 displays the profile of the streamwise r.m.s. velocity fluctuation $(R_{11}/ < \bar{\rho} >)^{1/2}$ obtained with M4 at three distinct times, where $y = x_2/\delta(t)$. The curves approximately coincide, confirming that the simulation is reasonably self-similar during this period of time.

Finally, the spanwise vorticity in a planar cut of the domain at two distinct

times in the M4-simulation is shown in figure 5.17. The large-scale roller structures in this simulation starting from uniform noise appear to be less prominent than in the simulations starting from an eigenfunction perturbation.

5.5 Conclusions

In this chapter we have presented *a posteriori* tests of Large-Eddy Simulations of the temporal mixing layer using six subgrid-models: Smagorinsky (M1), similarity (M2), gradient (M3), dynamic eddy-viscosity (M4), dynamic mixed (M5) and dynamic Clark (M6). The first three subgrid-models form the basis for the latter three dynamic models. Two sets of simulations have been performed, at low and high Reynolds number respectively. The Large-Eddy Simulations in the first set have been compared with DNS-data, whereas in the analysis of the second set of simulations we focussed on other aspects, such as self-similarity. The conclusions drawn from the first set of simulations are presented first.

In the first set of simulations the quality of a model is determined by the discrepancy of its results with the filtered DNS-results. Furthermore, in order to determine whether the inclusion of the subgrid-model is useful, comparisons with a coarse grid simulation without any subgrid-model (M0) have been performed. A summary of the results is found in table 5.2. When the models are arranged with respect to the overall accuracy of their results, the following sequence appears: M5, M6, M4, M2, M3, M1. The results of the latter two models are in general worse than the M0-results; incorporation of these subgrid-models in LES of the mixing layer is not useful. The other models in general give better results than M0. The overall results indicate that the dynamic mixed model displayed the best performance in these *a posteriori* tests. The dynamic mixed model was also observed to yield the most accurate results in comparitive tests of subgrid-models in LES of a driven cavity (Zang *et al.* 1993) and a rotating boundary layer (Wu & Squires 1995).

The Smagorinsky model was found to be excessively dissipative in the transitional regime. Comparison with the filtered DNS demonstrated that M1 strongly influences the linear evolution of disturbances, since the four-roller structure is not reproduced. Furthermore, M1 hindered the transition to turbulence. No positive spanwise vorticity was generated, the sudden growth of the momentum thickness did not occur and turbulent intensities and Reynolds stress profiles were under-predicted.

Although from the *a priori* point of view M2 and M3 are very similar and both provide highly accurate representations of the turbulent stress tensor (Vreman *et al.* 1995a) they behave very differently in actual simulations: M2 yields reasonable results, whereas M3 leads to instabilities if no limiter is used (see also

chapter 3). However, even with the incorporation of a limiter, M3 produces too many small scales and leads to inaccurate results for integral quantities and e.g. the streamwise turbulent intensity. In order to stabilise the gradient model, the inclusion of a dynamic eddy-viscosity as in M6 is preferred over a limiter (M3), since the first case leads to more accurate results.

Examination of the energy spectra demonstrates that only the models which contain a dynamic eddy-viscosity (M4-6), provide the correct amount of small scales. Due to insufficient dissipation of small scales by the subgrid-model, the flow simulated with M0, M2 and M3 contains too many small structures. This gives rise to a higher molecular dissipation, which supplements the insufficient small-scale dissipation of the model. Although the dissipation for small scales is insufficient, the total energy dissipation provided by M2 was observed to be reasonable, since too much energy was subtracted from the large scales. The models M2 and M5-6 have mechanisms to mimic the backscatter of energy from subgrid scales to resolved scales, but do not accurately predict it. However, actual LES of the mixing layer seems to require only a small amount of backscatter. The same is observed from the filtered DNS-results, in which the backscatter is about 10 percent of the subgrid dissipation. Hence, a poor representation of the backscatter by the subgrid-models is not too much a problem.

The second set of Large-Eddy Simulations with M0-6 concern a mixing layer at a much higher Reynolds number in a larger computational domain (section 5.4). No DNS-results are available to compare with, since the Reynolds number is too high to accurately resolve all scales with the present super computers.

Since the amount of subgrid dissipation obviously depends on the value of the Smagorinsky constant C_S, the dissipative behaviour of the Smagorinsky model could be better using a lower value for C_S. Therefore, in this case we used the lower $C_S = 0.10$ in the simulation with M1. The model is still too dissipative in the laminar regime; the transition occurs, but too late and in the turbulent regime the model is not sufficiently dissipative. Hence, a varying model coefficient that attains the appropriate value in transitional and turbulent regimes is required. The dynamic models meet this requirement.

The simulations with M0, M2 and M3 become unstable in the turbulent regime. M0 has no subgrid dissipation and the dissipation of M2 and M3 is insufficient to prevent an excessive amount of small scales.

The three dynamic models M4-6 adequately suppress the generation of small scales, but there are differences between the results of the three simulations. Within this group of models the dynamic eddy-viscosity model yields the most self-similar turbulent statistics. Self-similarity is presumably sensitive to the precise amount of subgrid dissipation in the turbulent regime, which is best predicted by this model (section 5.3.2).

The results in this chapter apply to the mixing layer at low Mach number. Details of the comparison may be valid only for this case, but the global features are expected to be more generally applicable. Examples of such global features are: the excessive dissipation of the Smagorinsky model, the insufficient dissipation of small scales by the similarity and gradient model and the relatively adequate small-scale predictions by the dynamic models. At higher Mach numbers, subgrid-modelling of the energy equation has to be taken into account (chapter 7) and, possibly, the subgrid-model has to model the interaction of turbulence with shocks.

Chapter 6

Comparison of numerical schemes in LES at low Mach number

The discrepancies between the results of LES and corresponding DNS or experiments have two sources: short-comings of the model (modelling errors) and inaccuracies resulting from the numerical approximation of derivatives on a relatively coarse grid (discretization errors). For LES not only a variety of subgrid-models is available, but also various numerical methods can be adopted. In the previous chapter we presented *a posteriori* tests of LES using different subgrid-models. In this chapter[1] we consider such tests using different numerical schemes in order to appreciate the role of discretization errors in LES.

The discretization error does not only depend on the numerical method, but also on the ratio between filter width (Δ) and grid-spacing (h). This ratio represents the number of grid points available for the smallest relevant scale in LES (Δ). If the ratio Δ/h is small, rapidly fluctuating fields have to be represented on a few grid points only. Consequently, the discretization error will be large and the results will be sensitive to the specific numerical method. At larger Δ/h ratios the discretization errors will be smaller. However, these cases either require more computational effort due to finer grids (fixed Δ) or imply larger modelling errors due to larger subgrid-scale contributions (fixed h). The best choice is the Δ/h ratio that minimises the total simulation error (arising from the modelling and the discretization) in simulations with comparable computational costs.

In practice LES is usually performed with $\Delta = h$ (e.g. Deardorff 1971 and Normand & Lesieur 1992) or $\Delta = 2h$ (e.g. Zang *et al.* 1992). In most current research the former option is selected, although Kwak *et al.* (1975) and Love

[1] This chapter is based on the paper Vreman *et al.* 1995d.

(1980) found that the total simulation error was minimal for $\Delta = 2h$. The work by Kwak *et al.* and Love is only applicable to schemes that are second order accurate in space. In this chapter we revisit this issue and establish the appropriateness of $\Delta = 2h$ for fourth-order and spectral schemes as well.

In *a priori* tests the modelling and discretization error can be separately calculated (Vreman *et al.* 1994c, 1995a). However, to distinguish between these errors in *a posteriori* tests is difficult (Meneveau 1994). Modelling and discretization errors act simultaneously in actual LES and the discrepancy with the filtered DNS gives information about the total error only. In this chapter we propose a procedure to separate the effects effects of modelling and discretization error in *a posteriori* tests. This procedure incorporates Large-Eddy Simulations with the same filter width at a higher resolution.

We conduct the *a posteriori* tests for the temporal mixing layer using the DNS described in chapter 5. The description of the Large-Eddy Simulations for five numerical schemes and two Δ/h ratios is found in section 6.1. Results are compared with filtered DNS-results in section 6.2 and the effects of modelling and discretization errors are separated in section 6.3.

6.1 Description of the Large-Eddy Simulations

The Large-Eddy Simulations use the dynamic mixed subgrid-model in combination with several numerical methods. Compared to the other subgrid-models the dynamic mixed model was found to give the most accurate results in the *a posteriori* tests in the previous chapter. The five numerical methods are the weighted (A) and standard (A') second-order central difference scheme, the weighted (B) and standard (B') fourth-order central difference scheme and the spectral scheme C. These methods have been defined in chapter 2.

The Large-Eddy Simulations are performed at the same Mach and Reynolds number, in the same cubic domain with length L and with the same boundary conditions as in the previous chapter. The uniform grid contains 32^3 cells with grid-spacing h. Since the numerical errors depend on the Δ/h ratio, we use two filter widths: $\Delta = L/16$ and $\Delta = L/32$. Thus we perform the simulations for $\Delta = 2h$ and $\Delta = h$ respectively. We employ the top-hat filter and the initial conditions are obtained by filtering the initial conditions of the DNS using the appropriate filter width.

The discrepancy between the LES and filtered DNS-results determines the quality of the LES. As in the previous chapter we include coarse-grid simulations without subgrid-model (LES with the zero model) as a further point of reference. These simulations are performed with scheme B for both $\Delta = 2h$ and $\Delta = h$.

The simulations with schemes A, B and C appear to be stable, but the stan-

dard central differencing methods A' and B' give rise to instabilities. The latter methods lead to an excessive small-scale generation ('π-waves'), which is not sufficiently suppressed by the molecular and subgrid dissipation. The transverse weighting introduced in schemes A and B is able to prevent the excessive generation of π-waves. Hence, LES-calculations on coarse grids using central differences can only be performed if the weighting procedure is incorporated. Hence, the results in the next sections only concern the simulations using A, B or C.

6.2 Comparison of results

Various quantities obtained from LES with schemes A, B and C are shown and compared with filtered DNS-data. We distinguish between the cases $\Delta = 2h$ and $\Delta = h$. In each case we consider the time evolution of the total kinetic energy E and momentum thickness δ defined in equation (5.1) and (5.7) respectively. In addition to these two global quantities we compare profiles of the turbulent kinetic energy calculated at $t = 70$ (compare section 5.3.8),

$$k(x_2) = \tfrac{1}{2} < \bar{\rho}(\tilde{u}_i - \frac{<\bar{\rho}\tilde{u}_i>}{<\bar{\rho}>})(\tilde{u}_i - \frac{<\bar{\rho}\tilde{u}_i>}{<\bar{\rho}>}) >, \tag{6.1}$$

where $< . >$ represents averaging over the homogeneous directions x_1 and x_3.

Figure 6.1 shows the results for the $\Delta = 2h$ case obtained with A, B and C, together with the results of the filtered DNS and the coarse grid simulation without subgrid-model. For the latter simulation scheme B has been used; scheme A gives comparable results, while the spectral scheme C results in an unstable coarse-grid simulation. Figure 6.1 shows that for all three methods the results of the dynamic mixed model are better than those corresponding to the coarse-grid simulation without subgrid-model. The differences caused by changing the numerical method are considerable, although smaller than the effect caused by the subgrid-model, which is represented by the difference between LES with the dynamic mixed model and the coarse-grid simulation without subgrid-model.

If we compare the results with the filtered DNS, B gives the best predictions for E, then C and finally A. For the evolution of the momentum thickness, C clearly gives the best results, then B and then A. With respect to the k-profile the three methods provide comparable accuracy. We conclude that for the $\Delta = 2h$ case, LES with a second-order method (A) gives worse results than LES with a higher order method (B or C). For the evolution of the momentum thickness, method C is better than B, but the reverse is true for the total kinetic energy.

Furthermore, with respect to computational effort, method C is about five times as expensive as method B and seven times as expensive as method A. One of the reasons that method C is more expensive is that for numerical stability method C requires a convective time step limit which is about three times

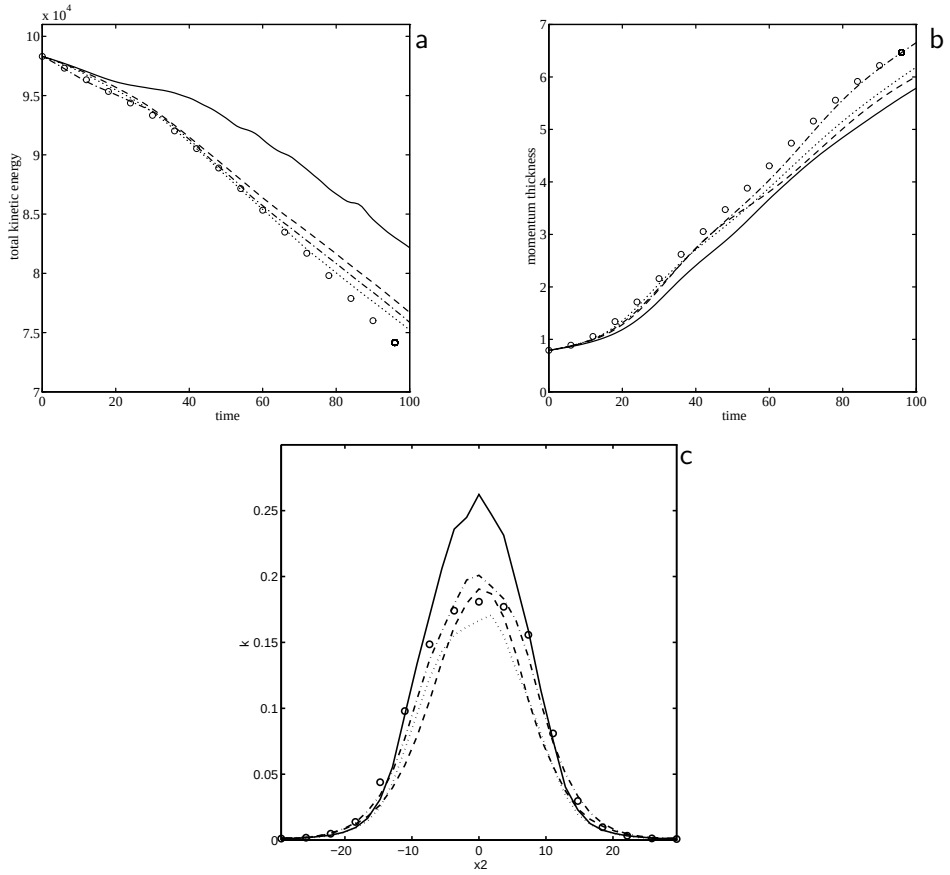

Figure 6.1: Comparison of numerical methods for the $\Delta = 2h$ case: the evolution of the total kinetic energy (a), the evolution of the momentum thickness (b) and the profile of the turbulent kinetic energy at $t = 70$ (c). Filtered DNS (marker o), LES with the zero model (solid), LES with the dynamic mixed model using the numerical methods A (dashed), B (dotted) and C (dashed-dotted).

smaller than required with method A. Therefore, if we take both accuracy and computational cost into account, scheme B is recommended.

So far we have presented results for the $\Delta = 2h$ case. Next, we alter the Δ/h ratio, keeping the grid-size h and thus the number of grid points constant, in order to compare results which are obtained with a comparable amount of work. As explained above, for smaller Δ with h kept constant, the discretization error becomes larger and the modelling error becomes smaller. We investigate how the sum of these two errors, the total error, behaves if the Δ/h ratio is altered.

The results for the $\Delta = h$ case are presented in figure 6.2, using the same

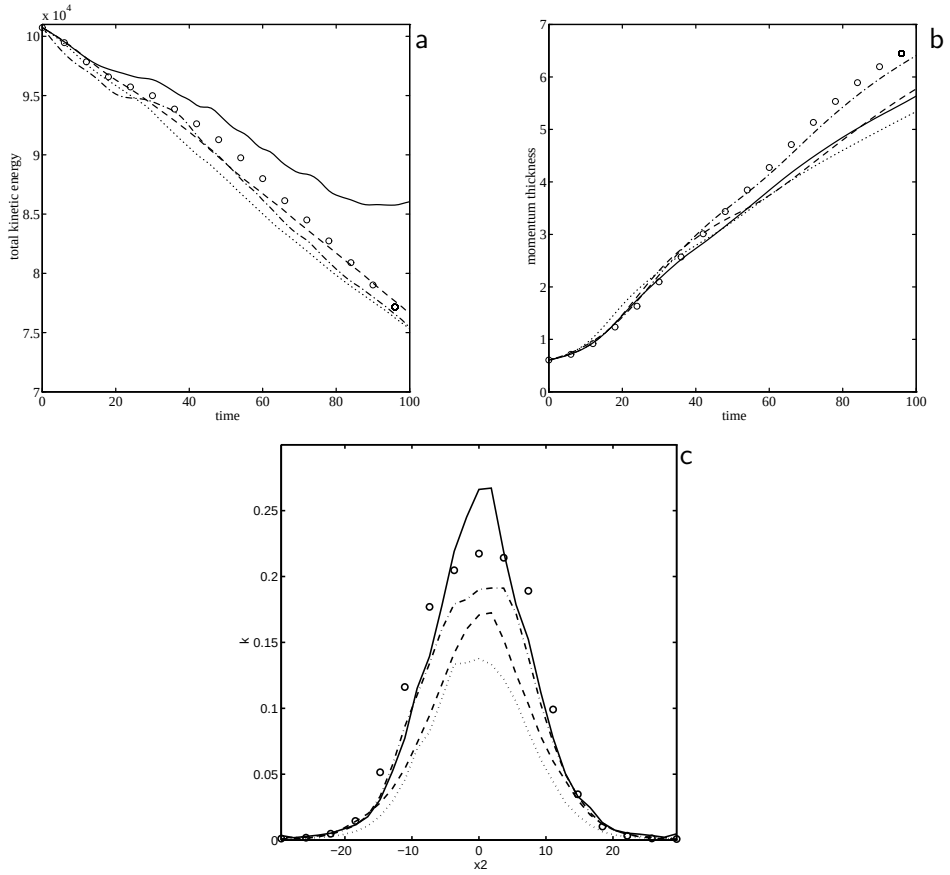

Figure 6.2: Comparison of numerical methods for the $\Delta = h$ case: the evolution of the total kinetic energy (a), the evolution of the momentum thickness (b) and the profile of the turbulent kinetic energy at $t = 70$ (c). Filtered DNS (marker o), LES with the zero model (solid) and LES with the dynamic mixed model using the numerical methods A (dashed), B (dotted) and C (dashed-dotted).

32^3-grid. The differences caused by changing the numerical method are quite large, and in several instances the discrepancy with the filtered DNS is larger than the difference between the coarse-grid simulation without subgrid-model and the filtered DNS. Comparing the differences with the filtered DNS, scheme A gives the best predictions for the evolution of E, then scheme C and finally scheme B. As far as the momentum thickness d and the k-profile are concerned, C gives the most acceptable results, then A and then B. Hence, for the $\Delta = h$ case the best results are obtained with (the most expensive) method C. If we have to choose between the cheaper methods A and B, the lowest order method

A is recommended. This example illustrates that in the $\Delta = h$ case, a second-order method can be preferred over a higher-order method in the class of finite difference methods.

Comparing the $\Delta = h$ (figure 6.2) to the $\Delta = 2h$ case (figure 6.1), we observe that for each numerical method, the curves in figure 6.2 are further from the filtered DNS than in figure 6.1. Hence, the $\Delta = 2h$ case is to be preferred over the $\Delta = h$ case, since it predicts the filtered DNS-results more accurately.

6.3 Separation between modelling and discretization errors

In the previous section we considered differences between LES and the filtered DNS. These differences we refer to as total errors. They are the sum of two effects: the effect of the modelling error, caused by short-comings in the subgrid-model, and the effect of the discretization error, caused by inaccuracies of the numerical method. In the following we approximately separate these effects.

The discretization error in a LES will become smaller if the resolution is increased (h is decreased), while the filter width Δ is kept constant. The discretization error in such a 'fine-grid LES' will be considerably smaller than in the original LES. The aim of performing such a fine-grid LES is to obtain a LES in which the discretization error effects are small compared to the discretization error effects in the original LES. The difference between those two Large-Eddy Simulations gives an indication of the effect of the discretization error. For the total kinetic energy E, we denote the discretization error effect as:

$$\epsilon_d(E) = E_{\text{LES}} - E_{\text{fine-grid LES}}. \tag{6.2}$$

We stress that the only difference between the fine-grid LES and the original LES is a different grid-spacing h; the filter width Δ is the same. Furthermore, since discretization error effects in the fine-grid LES are small, the difference between the fine-grid LES and the filtered DNS measures the effect of the modelling error:

$$\epsilon_m(E) = E_{\text{fine-grid LES}} - E_{\text{filtered DNS}}. \tag{6.3}$$

The total error is the sum of these two contributions:

$$\epsilon_t(E) = \epsilon_d(E) + \epsilon_m(E) = E_{\text{LES}} - E_{\text{filtered DNS}}. \tag{6.4}$$

Using equations (6.2) to (6.4) allows for an approximate separation of the different sources of error, provided the discretization error in the fine-grid LES is considerably smaller than the discretization error in the original LES and the modelling error in the fine-grid LES is about the same as in in the original LES.

Note that $\epsilon_d(E)$ and $\epsilon_m(E)$ are not identical to the discretization error and the modelling error; they only represent the effect of the discretization or modelling error in E. A small effect of an error in E for example, does not necessarily imply that the error itself, as it appears on the tensor or vector level in the filtered Navier-Stokes equations, is small.

We have calculated these errors for the original LES on the 32^3-grid with $\Delta = 2h = L/16$. The corresponding fine-grid LES has been performed on a grid with 64^3 using method B. The ratio between Δ and the grid-spacing in the fine-grid LES hence equals 4. This ratio is quite large, which implies that the fields are quite smooth on the grid-scale. Thus the discretization error in such a LES will be considerably smaller than in the original LES.

Figure 6.3 shows ϵ_d and ϵ_m for the three quantities E, δ and k. With respect to the evolution of E (figure 6.3a), the discretization error effects are smaller than the modelling error. The second-order scheme A is observed to give the smallest discretization error effect. For scheme B and C the discretization error and modelling error effect have opposite signs, which implies that the discretization error assists the subgrid-model in the representation of this quantity: the total error is smaller than the modelling error.

For the momentum thickness (figure 6.3b), the discretization error effects of the methods A, B and C and the modelling error effect are of the same order of magnitude. The reason for the good results produced by the spectral scheme is that the discretization error effect is opposite to the modelling error effect during the whole simulation and, consequently, the total error is considerably lower than the modelling error. Schemes A and B assist the subgrid-model only until $t = 50$. After $t = 50$ both schemes increase the total error, but scheme A yields a larger error than the higher-order scheme B. These observations suggest that for the spectral scheme, improvement of the subgrid-model (decrease of the modelling error) is expected to give worse results, since the total error will increase, while for schemes A and B, improvement of the model will provide better results after $t = 50$.

With respect to the k-profile (figure 6.3c) the discretization error for scheme C gives rise to smaller differences than for scheme A and B. Thus we have observed that the effects of the discretization error are often comparable to the effects of the modelling error. In some instances the discretization error partially cancels the modelling error, which implies that grid-refinement will not necessarily give rise to smaller total errors.

In this section we have presented results for the $\Delta = 2h$ case. A similar separation of error-effects for the $\Delta = h$ case, showed that the discretization error effects were larger than in the $\Delta = 2h$ case, while the modelling error effects were smaller. This behaviour was to be expected, since a decrease of Δ, with h

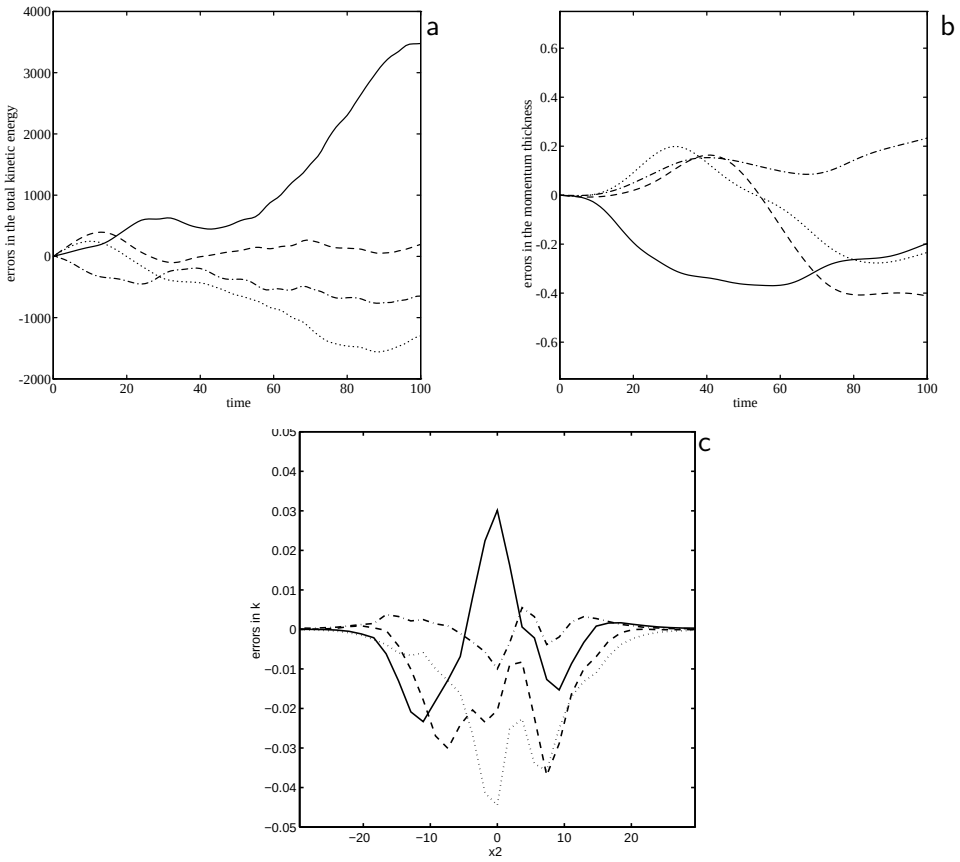

Figure 6.3: The modelling error effects (solid) and the discretization error effects for the numerical methods A (dashed), B (dotted) and C (dashed-dotted) for LES with $\Delta = 2h$. Errors in the evolution of the total kinetic energy (a), the evolution of the momentum thickness (b) and the profile of the turbulent kinetic energy at $t = 70$ (c).

kept constant, gives a more rapidly fluctuating field leading to less accurate approximations of derivatives, whereas on the other hand the subgrid contributions become smaller, leading to a smaller modelling error. In fact discretization errors were observed to dominate over the modelling errors in the $\Delta = h$ case and, consequently, further effort to improve the subgrid-model does not necessarily lead to improved predictions. *A priori* tests have predicted a similar behaviour (Vreman *et al.* 1994c, 1995a).

6.4 Conclusions

In this chapter we have presented *a posteriori* tests of Large-Eddy Simulations of the temporal mixing layer using the dynamic mixed subgrid-model in combination with several numerical methods. The numerical methods used were second-order central differences (A weighted and A' standard), fourth-order central differences (B weighted and B' standard) and a spectral method (C). Simulations with A' and B' turned out to be unstable due to excessive small-scale generation. The weighting in A and B thus proved to be essential in order to obtain stable calculations.

Employing methods A, B and C, we have compared the cases $\Delta = 2h$ and $\Delta = h$ respectively. In the $\Delta = 2h$ case the use of a high-order finite difference or a spectral scheme is suggested, while in the $\Delta = h$ case a lower-order finite difference or spectral scheme has to be preferred. In both cases the spectral scheme gives somewhat better results than the finite difference schemes, but it is also considerably more expensive with respect to computational effort. Taking this into account, scheme B is most efficient. From the comparison of the $\Delta = 2h$ and $\Delta = h$ cases with respect to total errors (differences with the filtered DNS), we conclude that the former case has to be preferred. It should be noticed that $\Delta = 2h$ does not imply an increased computational cost compared to $\Delta = h$, because only Δ is varied, while h is the same in both cases. Hence, the resolved variables in the $\Delta = 2h$ case are more accurate, but those in the $\Delta = h$ case contain more small-scale information, since Δ and thus the amount of energy in the subgrid scales is smaller.

Finally we have proposed a procedure to separate the effects of discretization and modelling error in the Large-Eddy Simulations. For the $\Delta = 2h$ case discretization error effects are smaller than or comparable to the modelling error. Furthermore, the discretization error does not always decrease the accuracy; sometimes it assists the subgrid-model and thus reduces the total error.

Chapter 7

Subgrid-modelling in the energy equation

The filtered equations for compressible flow have subgrid-terms in the momentum and energy equations. In the previous chapters we focussed on the modelling of the dominant subgrid-term in the momentum equation, the turbulent stress tensor. The subgrid-terms in the energy equation (energy subgrid-terms) are the subject of this chapter.[1]

Compared to incompressible LES, much less research has been conducted on compressible LES. The first compressible subgrid-model has been formulated by Yoshizawa (1986), who generalised the Smagorinsky formulation by incorporating a model for the isotropic part of the turbulent stress tensor. Erlebacher *et al.* (1992) have extended the standard mixed model to compressible isotropic turbulence. Moin *et al.* (1991) formulated the dynamic model for compressible LES, with the dynamic eddy-viscosity model in the momentum equation and a dynamic eddy-diffusivity model in the energy equation. This model has been applied to compressible isotropic turbulence (Moin *et al.* 1991) and to high-speed transitional boundary layers (El-Hady *et al.* 1993).

The filtered energy equation contains six subgrid-terms α_1 to α_6 (equations (2.24) to (2.29). In this thesis we use the evolution equation for the total energy, whereas Erlebacher *et al.* and Moin *et al.* employ the internal energy equation. As indicated in chapter 2 the differences between the two formulations are not large. The filtered internal energy equation contains the subgrid-terms α_2, α_3, α_4 and α_6. It does not contain α_1, whereas α_5 has a different form.

The question arises whether all energy subgrid-terms are equally important. Erlebacher *et al.* and Moin *et al.* use a model for α_2 only, but they do not give satisfactory arguments why the other subgrid-terms can be neglected. For this

[1] This chapter is partially based on the papers Vreman *et al.* 1994d and 1995be.

subgrid-term	$M = 0.2$	$M = 0.6$	$M = 1.2$
α_1	7.8	5.2	4.2
α_2	3.3	2.9	3.0
α_3	3.6	2.2	1.7
α_4	2.4	1.8	0.76
α_5	0.012	0.071	0.10
α_6	0.0074	0.044	0.082

Table 7.1: L_2-norms $(\cdot 10^3)$ of the energy subgrid-terms at three different Mach numbers: $M = 0.2$ $(t = 70)$, $M = 0.6$ $(t = 90)$ and $M = 1.2$ $(t = 200)$.

reason we calculate the magnitude of all energy subgrid-terms using DNS-data of the mixing layer at $M = 0.2$, 0.6 and 1.2 (section 7.1). These *a priori* estimates provide a first indication for each subgrid-term whether it can be neglected or has to be modelled. In section 7.2 we present new dynamic models for the relevant energy subgrid-terms. Actual Large Eddy Simulations with these models are performed in section 7.3.

7.1 A priori estimates of the energy subgrid-terms

The energy subgrid-terms are calculated from the DNS-data at three different Mach numbers: $M = 0.2$, 0.6 and 1.2. The set-up of the DNS at $M = 0.6$ is very similar to the $M = 0.2$ case, described in section 5.1. The stream- and spanwise sizes of the computational box at $M = 0.6$ equal $L_1 = L_3 = 68$, which corresponds to four times the wavelength of the most unstable linear mode. The other parameters are chosen equal to the values at $M = 0.2$. Visualization of the vorticity shows the formation of four two-dimensional rollers, which undergo subsequent pairings. However, the two-dimensional rollers cannot be discerned as clearly as in the $M = 0.2$ case and the pairing processes are somewhat slower in dimensionless time units. These observations are in agreement with linear stability theory, which predicts that two-dimensional waves become relatively less important than three-dimensional waves if the Mach number is increased. The DNS at $M = 1.2$ is described in detail in chapter 8.

The energy subgrid-terms are calculated according to their definitions where the derivatives and filtering integrations are taken on the fine grid. The values of the filter width are about the same in each case: $\Delta_1 = \Delta_2 = \Delta_3 = 3.7$ at $M = 0.2$, $\Delta_1 = \Delta_3 = 4.2$, $\Delta_2 = 3.7$ at $M = 0.6$ and $\Delta_1 = 4.0$, $\Delta_2 = \Delta_3 = 3.7$ at $M = 1.2$. The energy subgrid-terms are evaluated at representative times in

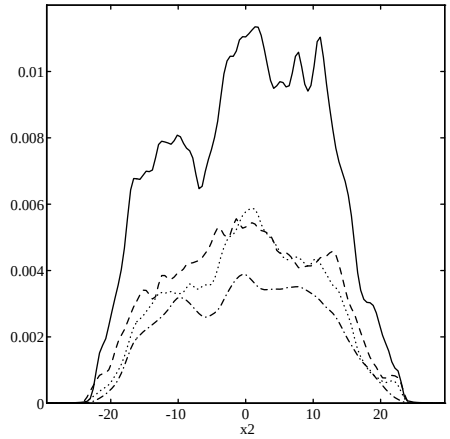

Figure 7.1: L_2-norms in x_1-x_3 planes for the energy subgrid-terms at $M = 0.2$ at $t = 80$: α_1 (solid), α_2 (dashed), α_3 (dotted) and α_4 (dashed-dotted).

the turbulent regimes of the simulations. These times are $t = 70$, 90 and 200 for $M = 0.2$, 0.6 and 1.2 respectively and correspond to the same value of the momentum thickness. Table 7.1 shows the L_2-norms of the energy subgrid-terms at these three times.

The table shows that the subgrid-terms α_1 to α_4 have the same order of magnitude. These terms are an order of magnitude larger than α_5 and α_6. These observations are valid for all three Mach numbers, although the difference between α_{1-4} and $\alpha_{5,6}$ is less pronounced if the Mach number is increased. The terms $\alpha_{5,6}$ are due to the nonlinearities in the viscous stress tensor and heat flux. From an *a priori* point of view these terms can be neglected compared to the other energy subgrid-terms for a reasonably wide range of Mach numbers. Furthermore, the difference between α_1 (the turbulent stress on scalar level) and α_5 indicates that the viscous subgrid-term in the momentum equation, $\partial_j(\bar{\sigma}_{ij} - \breve{\sigma}_{ij})$, can be neglected, being much smaller than $\partial_j(\bar{\rho}\tau_{ij})$.

In order to demonstrate the spatial structure of the energy subgrid-terms α_{1-4}, we show L_2-norms at $M = 0.2$ in figure 7.1. The norms have been calculated for each x_2 by integration over the homogeneous directions. The curves for the higher Mach number cases have similar shapes and the respective levels correspond to the global norms in table 7.1.

These *a priori* estimates suggest that a subgrid-model for the energy equation should take the four subgrid-terms α_{1-4} into account. The compressible models found in literature (Erlebacher *et al.* 1992, Moin *et al.* 1991) do model the

subgrid-term α_2 (and implicitly α_1 as well), but neglect the subgrid pressure dilatation α_3 and the subgrid turbulent dissipation rate α_4. In the next section we formulate subgrid-models for the energy equation, which also take α_3 and α_4 into account.

7.2 Dynamic modelling of the energy subgrid-terms

In this section we present two new dynamic subgrid-models which incorporate the four energy subgrid-terms α_{1-4}. The first formulation models the energy subgrid-terms starting from the dynamic eddy-viscosity model for τ_{ij}, whereas the second formulation models these terms using the dynamic mixed model for τ_{ij}. The models are called the full dynamic eddy-viscosity model (M4E1) and the full dynamic mixed model (M5E1) respectively. The notation M4E1/M5E1 denotes that the dynamic models M4/M5 (see chapter 5) are extended to the energy equation incorporating α_{1-4}.

7.2.1 The full dynamic eddy-viscosity model

The turbulent stress tensor τ_{ij} in M4E1 is modelled with the dynamic eddy-viscosity model (M4) given in chapter 3. This expression substituted in the definition of α_1 provides the subgrid-model for α_1.

Moin *et al.* (1991) introduced a dynamic eddy-diffusivity concept to model the pressure velocity subgrid-term α_2. The dynamic eddy-diffusivity model employed in M4E1 is slightly different. The dynamic procedure is applied such that the model represents the sum $\alpha_2 + \alpha_3$ instead of α_2 only, in order to model the effect of α_3. Hence, the following expression is proposed for these subgrid-terms:

$$\alpha_2 + \alpha_3 = -\partial_j\left(\frac{\bar{\rho} C_d \Delta^2 S(\tilde{\mathbf{u}})}{(\gamma - 1) Pr_t M^2} \partial_j \tilde{T}\right), \tag{7.1}$$

where the numerator in the fraction denotes the eddy-viscosity on the F-level and Pr_t is the dynamic turbulent Prandtl number. This eddy-diffusivity model is similar to the molecular heat flux term (equation (2.8)), but the molecular viscosity and Prandtl number have been replaced by the dynamic eddy-viscosity in equation (3.22) and the turbulent Prandtl number. The non-dynamic formulation was first introduced by Eidson (1985) in LES of the Rayleigh-Bénard problem. Here the turbulent Prandtl number is a dynamic coefficient.

To expose the dynamic procedure for Pr_t, it is convenient to write the subgrid-terms $\alpha_2 + \alpha_3$ as follows:

$$\alpha_2 + \alpha_3 = \tau_f = \overline{f(\mathbf{w})} - f(\overline{\mathbf{w}}), \tag{7.2}$$

where

$$f(\mathbf{w}) = \frac{\partial_j(pu_j)}{\gamma - 1} + p\partial_j u_j \qquad \text{with} \qquad \mathbf{w} = (\rho, \rho\mathbf{u}, p). \tag{7.3}$$

Substitution of the eddy-diffusivity model (7.1) in the generalised Germano identity (3.16) yields:

$$\frac{1}{Pr_t} M_f = L_f, \tag{7.4}$$

where L_f is defined by (3.17) and

$$M_f = -\partial_j(\frac{\hat{\widehat{\rho}} C_d (\kappa\Delta)^2 S(\mathbf{v})}{(\gamma-1)M^2} \partial_j G(\widehat{\widehat{\rho}}, \widehat{\widehat{p}})) + (\partial_j(\frac{\bar{\rho} C_d \Delta^2 S(\tilde{\mathbf{u}})}{(\gamma-1)M^2} \partial_j \tilde{T}))\widehat{\ }. \tag{7.5}$$

The symbol $\mathbf{v}$ represents the Favre-filtered velocity on the FG-level ($v_i = \widehat{\overline{\rho u}_i}/\widehat{\overline{\rho}}$) and $G(\widehat{\widehat{\rho}}, \widehat{\widehat{p}})$ represents the Favre-filtered temperature on the FG-level (see definition (2.9)).

The dynamic Prandtl number Pr_t in this work is assumed to be a function of time only. Hence, it can consistently be taken out of the spatial derivatives and filterings. The following least square approach is used to calculate Pr_t:

$$1/Pr_t = \frac{\int L_f M_f d\mathbf{x}}{\int M_f^2 d\mathbf{x}}, \tag{7.6}$$

where the integrations are performed over the whole domain. The dynamic Prandtl number is artificially set to infinity at times where the right-hand side of (7.6) returns negative values.

In order to complete M4E1 we incorporate a model for the turbulent dissipation rate α_4. It is a positive quantity, provided a positive filter is used (chapter 4). The term also occurs in the k-equation model of incompressible LES studied by Horiuti (1985) and Ghosal *et al.* (1995). Following these references we model the term by:

$$\alpha_4 = c_\epsilon \bar{\rho} \frac{k^{3/2}}{\Delta}, \tag{7.7}$$

where $k = \frac{1}{2}\tau_{ii}$ is the subgrid turbulent kinetic energy and c_ϵ is a dynamic coefficient which is assumed to be a function of time only. Note that the filter function has to be positive in order to guarantee the positivity of k. The model is ill-defined if the spectral cut-off filter is used. In the following we present a new procedure to obtain the dynamic coefficient c_ϵ.

Ghosal *et al.* (1995) remark that for high Reynolds number flows the coefficient cannot be determined using the standard dynamic procedure, since the turbulent dissipation is essentially a small-scale phenomenon. Turbulent energy is generated by the large scales and after it has been transferred to small scales

it is dissipated by molecular viscosity. The magnitude of the turbulent dissipation rate is therefore set by the large scales, but the dissipation takes place at the smallest scales. This implies that α_4 will not be small in fully developed high Reynolds number flows. It also implies that there is no dissipation left in the resolved scales if the Reynolds number is high. Consequently, the Germano identity for α_4 is zero in the limit of infinite Reynolds number and cannot be used to determine c_ϵ. Therefore, Ghosal *et al.* (1995) do not use the Germano identity for the turbulent dissipation rate, but determine c_ϵ with a complicated procedure, using a local balance of the terms in the k-equation.

We present a much simpler procedure to determine c_ϵ, using a global balance of the terms in the integrated k-equation. In this approach c_ϵ is necessarily a function of time only, in contrast to the approach by Ghosal *et al.*, where c_ϵ depends on time and space. The k-equation in compressible flow can be written as:

$$\partial_t(\bar{\rho}k) = \alpha_1 + \alpha_3 - \alpha_4 + \partial_j R_j, \tag{7.8}$$

where the last term represents all contributions which can be written in divergence form. Integrating this equation over the computational domain and assuming that R_2 is negligible at the free-slip walls gives

$$\partial_t \int (\bar{\rho}k) = \int (\alpha_1 + \alpha_3 - \alpha_4) d\mathbf{x}. \tag{7.9}$$

Substitution of the dissipation model (7.7) in this equation provides an expression for the model coefficient:

$$c_\epsilon = \frac{\int (\alpha_1 + \alpha_3 - \partial_t(\bar{\rho}k)) d\mathbf{x}}{\int (\bar{\rho}k^{3/2}/\Delta) d\mathbf{x}}. \tag{7.10}$$

The quantities α_1 and k can be calculated from the resolved variables and the model for the turbulent stress tensor τ_{ij}. The integral $\int \alpha_3 d\mathbf{x}$ is obtained by integrating the model for $\alpha_2 + \alpha_3$, since $\int \alpha_2 d\mathbf{x} = 0$. The model for $\alpha_2 + \alpha_3$ in equation (7.1) is in divergence form, hence it does not contribute to the global integral. *A priori* calculations of the integrals from the DNS-data show that the integrated α_3 is very small indeed. Furthermore, in the turbulent regime the total amount of subgrid energy is approximately constant, because the energy spectrum has filled up. In that case the integrated $\partial_t(\bar{\rho}k)$ is small, leading to a balance between α_1 and α_4:

$$\int \alpha_1 d\mathbf{x} \approx \int \alpha_4 d\mathbf{x}. \tag{7.11}$$

This does not necessarily imply equal L_2-norms for α_1 and α_4 in table 1, since α_4 is positive everywhere, but α_1 can change sign.

The left-hand side of equation (7.11) is equal to the energy transfer from resolved to subgrid scales by the subgrid-model. This term acts as a dissipation term in the resolved kinetic energy equation, but occurs as a production term in the subgrid kinetic energy equation. Equation (7.11) expresses a state of global equilibrium in fully developed turbulence at high Reynolds numbers in which the energy transfer from resolved to subgrid scales is equal to the molecular dissipation occurring at the smallest scales.

7.2.2 The full dynamic mixed model

Whereas M4E1 employs the dynamic eddy-viscosity model (M4), the full dynamic mixed model M5E1 adopts the dynamic mixed model (M5) for the turbulent stress tensor τ_{ij}. As in the previous model, the quantities α_1 and k can be calculated once τ_{ij} is known.

Erlebacher *et al.* (1992) have introduced the mixed model for α_2, proposing a linear combination of the similarity model and an eddy-diffusivity model. We propose a dynamic version of this model. Furthermore, we incorporate the pressure-dilatation subgrid-term α_3. Hence, these two terms are modelled together as:

$$\alpha_2 + \alpha_3 = \overline{f(\overline{\mathbf{w}})} - f(\overline{\overline{\mathbf{w}}}) - \partial_j\left(\frac{\bar{\rho} C_d \Delta^2 S(\tilde{\mathbf{u}})}{(\gamma-1) Pr_t M^2} \partial_j \tilde{T}\right), \tag{7.12}$$

where f and $\mathbf{w}$ are defined in (7.3). The expression represents the similarity model for $\alpha_2 + \alpha_3$ supplemented with a dynamic eddy-diffusivity term. The eddy-diffusivity is the fraction of the eddy-viscosity in the dynamic mixed model (equation (3.26)) and the dynamic turbulent Prandtl number Pr_t.

The model is substituted in the generalised Germano identity to obtain the coefficient Pr_t, which results in

$$H_f + \frac{1}{Pr_t} M_f = L_f, \tag{7.13}$$

where L_f is defined in (3.17), M_f in (7.5) and

$$H_f = \widehat{\overline{f(\hat{\overline{\mathbf{w}}})}} - f(\hat{\overline{\overline{\mathbf{w}}}}) - \left(\overline{f(\overline{\mathbf{w}})} - f(\overline{\overline{\mathbf{w}}})\right)\widehat{\ }. \tag{7.14}$$

Like in M4E1, Pr_t is a function of time only and is obtained with the least square approach

$$1/Pr_t = \frac{\int (L_f - H_f) M_f \, d\mathbf{x}}{\int M_f^2 \, d\mathbf{x}}, \tag{7.15}$$

where the integrations are performed over the whole domain. A theoretical advantage of the mixed model over the eddy-diffusivity model is that it does not

model	turbulent stress tensor τ_{ij}	the energy subgrid-terms α_{1-4}
M0	0	0
M4E0	dynamic eddy-viscosity	0
M4E1	dynamic eddy-viscosity	see section 7.2.1
M4E2	dynamic eddy-viscosity	as in M4E1, but with $\alpha_3 = \alpha_4 = 0$
M5E0	dynamic mixed	0
M5E1	dynamic mixed	see section 7.2.2

Table 7.2: Subgrid-models in the momentum and energy equation.

force $\int \alpha_3 d\mathbf{x}$ to be zero, since the similarity part of the mixed model is not in divergence form. However, this integral appears to be relatively small in *a priori* and *a posteriori* tests.

The expressions for the model for α_4 are the same as in the previous subsection, but evaluated for the dynamic mixed models: equation (7.7) for α_4 and (7.10) for the coefficient c_ϵ. To incorporate a similarity model for the dissipation is not very useful, since such a model extracts its information from the resolved scales. As explained in the previous subsection, the resolved scales do not contribute to α_4 if the Reynolds number is high. Indeed, *a priori* tests at $M = 0.2$ for the filter width given in section 7.1 show that the magnitude of the similarity model for α_4 is only 12% of the actual magnitude of α_4 (Vreman *et al.* 1995b).

7.3 Results of Large-Eddy Simulations

Several calculations are performed to test the models for the energy subgrid-terms α_1 to α_4 for three convective Mach numbers: $M = 0.2$, $M = 0.6$ and $M = 1.2$. The Large Eddy Simulations use a grid with $32 \times 33 \times 32$ points in the $M = 0.2$ and 0.6 cases and $40 \times 65 \times 24$ points in the $M = 1.2$ case. The basic filter is in each case is the top-hat filter with $\Delta = 2h$, the initial conditions are obtained by filtering the corresponding initial DNS-data and the equations are numerically solved using scheme B (chapter 2).

The purpose is to test the full dynamic eddy-viscosity model (M4E1) and the full dynamic mixed model (M5E1) for the three convective Mach numbers. As in the *a posteriori* tests presented in chapters 5 and 6, the LES-results are compared with filtered DNS-results and the results of a coarse grid simulation without a subgrid-model (M0). In order to measure the effect of modelling the energy subgrid-terms, additional simulations are performed which only omit the energy subgrid-terms. These simulations are labelled M4E0 and M5E0 and are

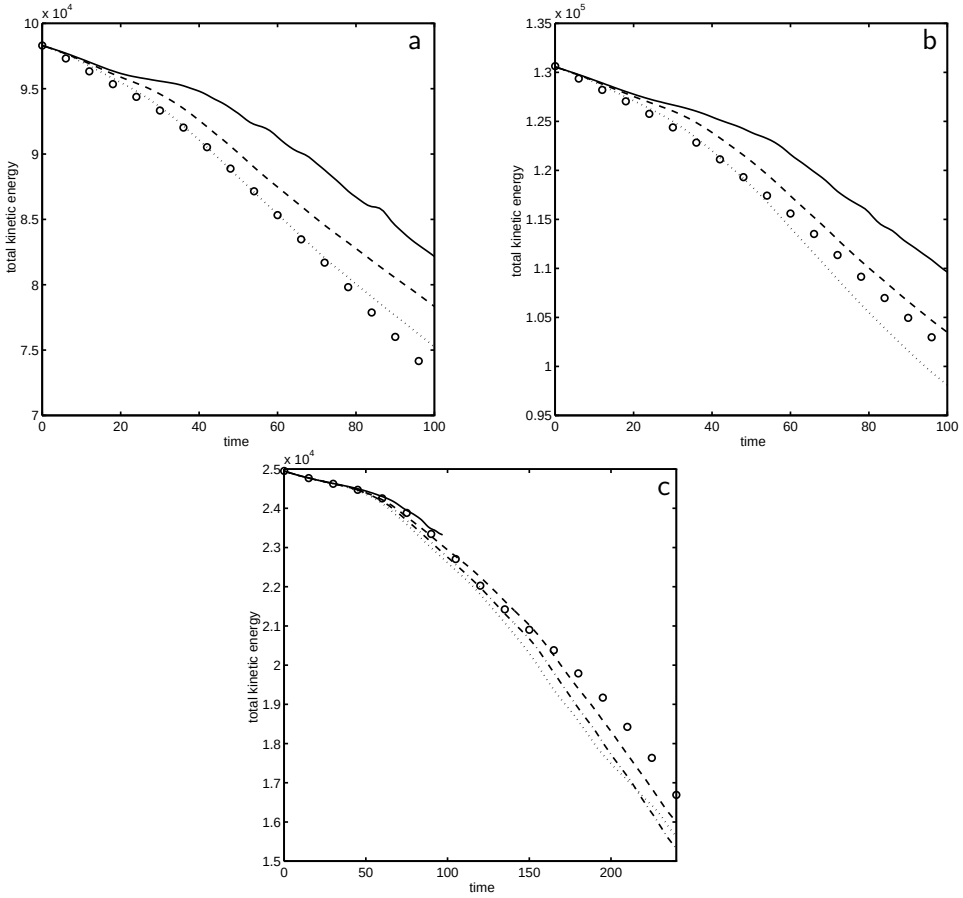

Figure 7.2: Total kinetic energy E for $M = 0.2$ (a), $M = 0.6$ (b) and $M = 1.2$ (c) obtained from the filtered DNS (marker o) and from LES using M0 (solid), M4E0 (dashed), M4E1 (also the dashed line), M5E0 (dotted), M5E1 (dotted in (a,b) and dashed-dotted in (c)).

compared with M4E1 and M5E1, respectively. As noticed before, the subgrid-terms α_3 and α_4 have been neglected in other work on LES incorporating the energy equation (Erlebacher *et al.* 1992; Moin *et al.* 1991). For this reason we also consider simulation M4E2, in which α_1 and α_2 are modelled, but α_3 and α_4 are neglected. These terms are neglected when the pressure-dilatation part in equation (7.3) is omitted and c_ϵ is put to zero. Table 7.2 contains a list of the models used in this section.

The evolution of the total kinetic energy E defined in (5.1) is shown in figure 7.2 for the three Mach numbers. With respect to the models in the energy equation, we observe no difference between M4E0 and M4E1 for all Mach numbers

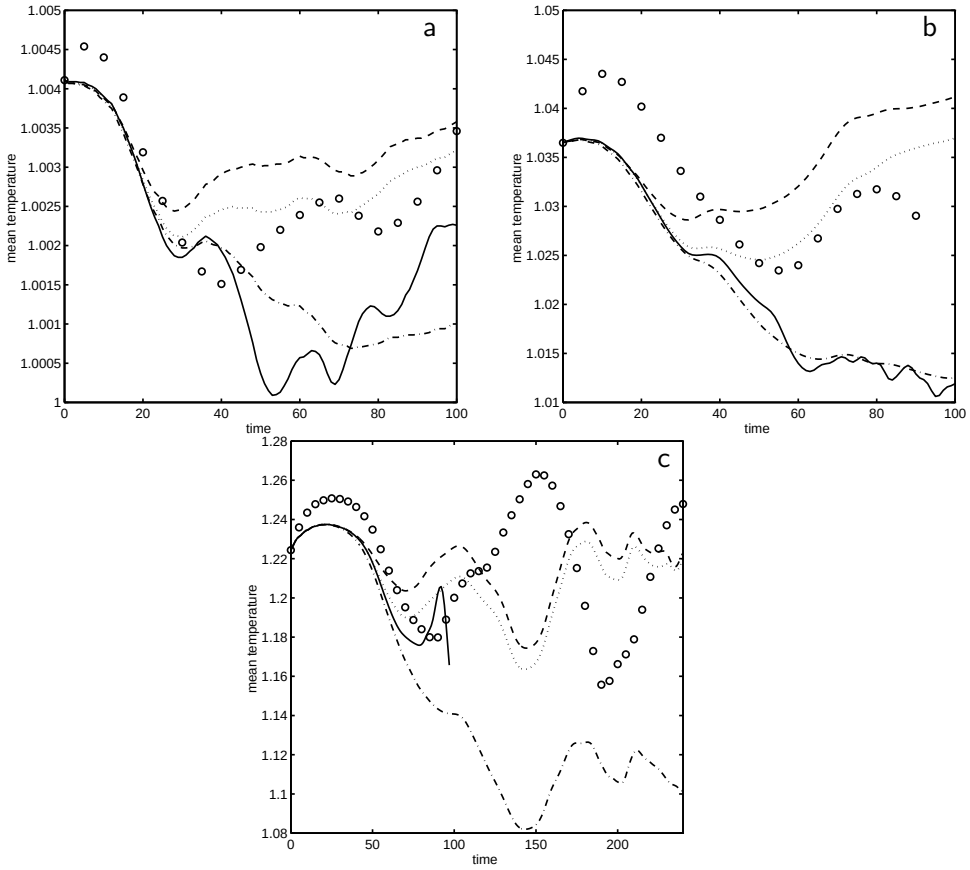

Figure 7.3: Mean temperature at $x_2 = 0$ for $M = 0.2$ (a), $M = 0.6$ (b) and $M = 1.2$ (c) obtained from the filtered DNS (marker o) and from LES using M0 (solid), M4E0 (dashed), M4E1 (dotted) and M4E2 (dashed-dotted).

and between M5E0 and M5E1 for $M = 0.2$ and 0.6. Hence, it appears that modelling of the energy subgrid-terms at $M = 0.2$ and $M = 0.6$ has a negligible effect on the total kinetic energy. The effect at $M = 1.2$ is larger, but still small compared to the effect of modelling τ_{ij} in the momentum equation (comparison with M0).

With respect to the momentum equation, the dynamic mixed model for τ_{ij} yields the best results in the lowest Mach number case, but at higher Mach numbers (0.6 and 1.2) the dynamic eddy-viscosity model turns out to be more accurate. Inclusion of a subgrid-model for τ_{ij} is found to be absolutely necessary at $M = 1.2$, since without subgrid-model the coarse-grid simulation cannot be completed. In the remaining part of this section we only consider the dynamic

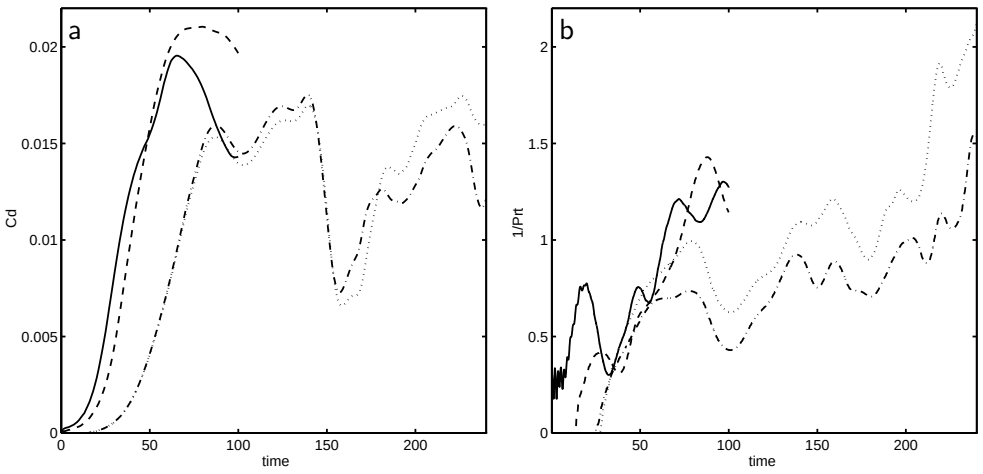

Figure 7.4: Model coefficient C_d at $x_2 = 0$ (a) and $1/Pr_t$ (b) using model M4E1 at $M = 0.2$ (solid), $M = 0.6$ (dashed) and $M = 1.2$ (dotted), and model M4E2 at $M = 1.2$ (dashed-dotted).

eddy-viscosity model for τ_{ij}.

The total kinetic energy and the other quantities discussed in chapter 5 (e.g. energy spectrum, momentum thickness and vorticity) are directly related to the momentum equation. Incorporation of the energy subgrid-terms appears to alter such quantities only slightly. Thermodynamic quantities are likely to be more affected by the energy subgrid-terms. As an example we consider the mean temperature.

Figure 7.3 shows the mean temperature, $< \rho T > / < \rho >$, in the centre plane. The mean temperature profile in this flow attains its maximum at this location. The figure shows that the mean temperature and its temporal fluctuations increase if the Mach number is increased. The absolute temperature variations at high Mach number are much larger than at low Mach number. These variations are also influenced by the initial mean temperature profile, prescribed by the Crocco-Busemann law (section 1.3), which depends on Mach number. With respect to the centre mean temperature, M4E0 and M4E1 give different results for each Mach number, indicating that this quantity is influenced by the energy subgrid-terms. The role of temperature and its change by the energy subgrid-terms clearly become more important at higher Mach numbers.

Inclusion of the energy subgrid-terms is useful for this quantity, since with energy subgrid-terms (M4E1) the prediction is closer to the filtered DNS-result than without (M4E0). More specifically, the energy subgrid-terms in M4E1 de-

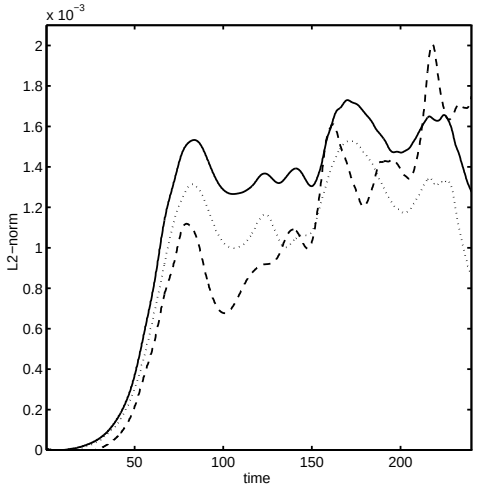

Figure 7.5: L_2-norms of the terms α_1 (solid), $\alpha_2 + \alpha_3$ (dashed) and α_4 (dotted) in LES using model M4E1 at $M = 1.2$.

crease the mean temperature at each Mach number. The mean temperature is strongly under-predicted by M4E2 (and by M0). Modelling the subgrid-terms α_{1-2}, but neglecting α_{3-4} is thus worse than neglecting all energy subgrid-terms. This is mainly due to α_1 and α_4, since these terms after integration are much more important than the other energy subgrid-terms. These terms occur with opposite signs in the energy equation and appear to have opposite effects. The subgrid-term α_1 decreases, but the dissipation α_4 increases the temperature. The dissipation α_4 represents the conversion of subgrid kinetic energy into internal energy and, obviously, this process increases the temperature. Since the global effects of α_1 and α_4 approximately cancel each other (equation (7.11)), these subgrid-terms should both be modelled or both be neglected.

The effect of Mach number on the dynamic model coefficients that occur in the eddy-viscosity and eddy-diffusivity is not large (figure 7.4). The values for C_d and $1/Pr_t$ are low in the transitional stage, giving rise to a relatively small eddy-viscosity and diffusivity. The coefficient C_d in the dynamic eddy-viscosity model in the turbulent regime can be compared with the square of the constant in the Smagorinsky model, i.e. $C_d = 0.2$ corresponds to a Smagorinsky constant of 0.14. The turbulent Prandtl number Pr_t ($1/Pr_t$ has been plotted) fluctuates around 1 in the turbulent regime. The difference between M4E1 and M4E2 at $M = 1.2$ in figure 7.4b demonstrates that the usually neglected pressure-dilatation subgrid-term α_3 is smaller than α_2, in agreement with the *a priori* tests. However, it has a significant contribution to the eddy-diffusion of about 25% and, hence, is

preferred to be taken into account.

Finally, the global L_2-norms of the modelled quantities, α_1, $\alpha_2 + \alpha_3$ and α_4 in M4E1 are shown in figure 7.5. These energy subgrid-terms thus appear to be of the same order of magnitude, which was also indicated by the *a priori* tests in section 7.2.

7.4 Conclusions

In this chapter we have addressed the modelling of the energy subgrid-terms and performed *a priori* and *a posteriori* tests at low (0.2), moderate (0.6) and high (1.2) convective Mach number. The *a priori* tests indicate that four of the six energy subgrid-terms, α_{1-4} are of the same order of magnitude. The other two subgrid-terms, due to nonlinearities in the viscous and heat flux term, are much smaller. To model the relevant energy subgrid-terms we have presented two new models: the full dynamic eddy-viscosity (M4E1) and the full dynamic mixed model (M5E1). Both models incorporate the usually neglected pressure-dilatation and dissipation subgrid-terms, α_3 and α_4 respectively.

These models have been used in actual LES at $M = 0.2$, 0.6 and 1.2 and the results have been compared with filtered DNS-data and LES without energy subgrid-terms. Several conclusions can be drawn. In contrast to the lowest Mach number case, the dynamic eddy-viscosity model for τ_{ij} gives more accurate results than the dynamic mixed model at high Mach numbers. A satisfactory explanation of the different accuracy of the dynamic mixed model at different Mach numbers is not yet available. Using the dynamic mixed model in LES at high Mach numbers, however, is still much better than using no subgrid-model at all.

The energy subgrid-terms appear to have a very small effect upon quantities extracted from the momentum variables, even at high Mach number. Thermodynamic quantities, however, are more affected by the energy subgrid-terms. In particular, the maximum mean temperature was found to be better predicted if the energy subgrid-terms were included. The actual Large-Eddy Simulations confirmed the *a priori* finding that the energy subgrid-terms α_{1-4} are of comparable size.

The mixing layer investigated in this thesis has equal free-stream thermodynamic variables. The role of the energy subgrid-terms may become more important in flows with larger temperature gradients, for example in a mixing layer with a large difference between the upper and lower free-stream temperatures.

Chapter 8

Shocks in DNS at high Mach number

Numerical simulations of the two-dimensional compressible mixing layer have shown that shocks appear when the convective Mach number M is higher than 0.7 (Lele 1989, Sandham & Yee 1989). Furthermore, the occurrence of shocks in homogeneous isotropic turbulence has been investigated for the two- and three-dimensional cases (Passot & Pouquet 1987, Lee *et al.* 1991). In this chapter[1] we describe a Direct Numerical Simulation of the three-dimensional turbulent mixing layer at $M = 1.2$ (section 1) and describe the shocks that occur in this flow (section 2). In simulations of the three-dimensional compressible mixing layer shocks have not been observed before (Sandham & Reynolds 1991, Lele 1994). The Direct Numerical Simulation in this chapter is different from those described in the latter references. It has been calculated at a higher convective Mach number and further into the nonlinear regime in order to obtain a mixing transition to small scales.

8.1 Description of the DNS

The temporal mixing layer is simulated at convective Mach number $M = 1.2$. The Reynolds number based on the upper stream velocity and half the initial vorticity thickness equals 100. The initial condition is formed by the mean profiles described in chapter 1 superimposed with a disturbance consisting of one pair of equal and opposite oblique modes. Such a disturbance has intensively been studied for somewhat lower Mach numbers (Sandham & Reynolds 1991) and was found to initiate mixing transition in compressible mixing layers (Luo & Sandham

[1] This chapter is based on the papers Vreman *et al.* 1995fg.

1994). The two modes are denoted by (1,1) and (1,-1) and correspond to the most amplified waves in the linear stability problem. The amplitude of the initial disturbance is 0.1 for each mode. The stream- and spanwise wavelengths of these modes determine the sizes of the computational domain in the homogeneous directions, given by $L_1 = 39.9$ and $L_3 = 22.1$ respectively. The length of the domain in the normal direction is $L_2 = 59$, the same as in the lower Mach number cases described in the previous chapters.

An alternating numerical scheme, built out of the ingredients listed in chapter 2, has been constructed to solve the Navier-Stokes equations. The time marching scheme is the second-order accurate Runge-Kutta method. The numerical discretization for the spatial derivatives is alternating in the sense that scheme D is used in the directions where steep gradients occur at times when shocks are present, whereas scheme B is used otherwise. Scheme D employs a third-order accurate MUSCL-scheme for the convective terms (Van der Burg 1993), which is able to capture shocks. The convective terms in scheme B are discretized with weighted fourth-order accurate central differences. It is well-known that a central differencing method for the convective terms is unable to treat shocks, unless the steep gradients within the shocks can be fully represented on the grid. Therefore, the alternating scheme is preferred over a permanent application of the fourth-order central scheme. It is also preferred over a permanent application of the MUSCL-scheme for the following two reasons. First, the MUSCL-scheme is less accurate than the fourth-order central scheme when no shocks are present or when the shocks can be fully represented on the grid. In fact a permanent application of the MUSCL-scheme would require an even finer grid than the grids used in this chapter or it would seriously affect the accuracy of the transition to turbulence. Furthermore, the MUSCL-scheme is computationally considerably more expensive than the fourth-order central scheme (about a factor of two).

Since shocks can be identified by strong pressure gradients, the MUSCL-scheme is applied when the pressure gradient exceeds a threshold value. More specifically, when

$$s_i = \max \left| \frac{\partial p}{\partial x_i} \right| \frac{\Delta x_i}{p_0} > c \tag{8.1}$$

at a certain time t (the summation convention is not used), all convective fluxes in the x_i-direction are calculated with the MUSCL-scheme; otherwise the fourth-order central discretization is used. In expression (8.1) s_i is called the shock-sensor in the x_i-direction, whereas Δx_i and p_0 denote the grid-spacing and the initial mean pressure respectively and have been incorporated in order to make s_i independent of the scaling of the equations. The case $c = 0$ corresponds to a permanent application of the MUSCL-scheme and $c = \infty$ to a permanent application of the fourth-order central scheme. An alternating scheme is obtained

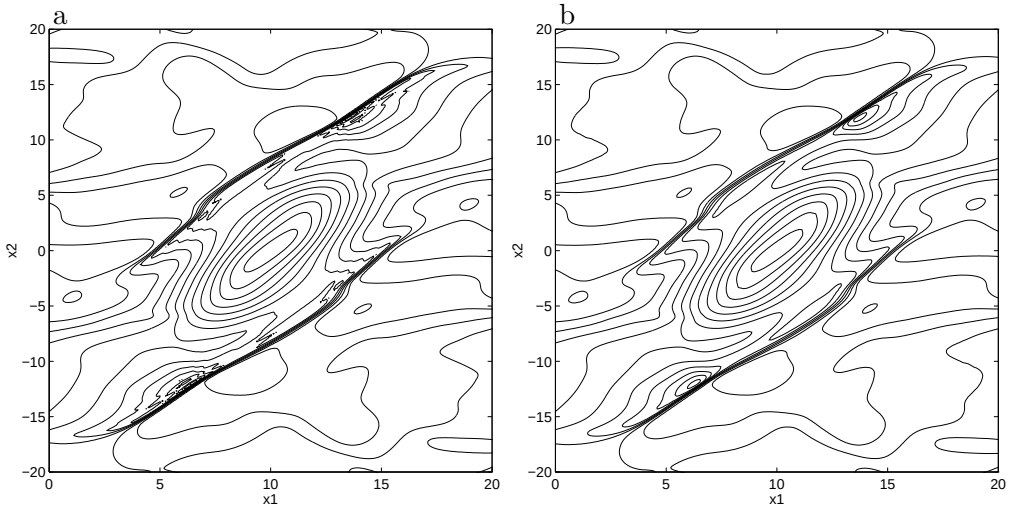

Figure 8.1: Contours of the pressure in the plane $x_3 = 3.9$ at $t = 204$ for $c = \infty$ (a) and $c = 0.2$ (b). The contour increment is 0.05.

if c is given an appropriate intermediate value.

For the flow simulated in this chapter $c = 0.2$ appears to give satisfactory results. Figure 8.1 shows contour plots of the pressure at $t = 204$ for two simulations with $c = \infty$ and $c = 0.2$, respectively. At this time the pressure gradient attains its maximum in the plane shown. The spurious oscillations around the shock in figure 8.1a demonstrate that the fourth-order central difference ($c = \infty$) is not able to capture the shock, whereas the alternating scheme ($c = 0.2$) provides a smooth representation of the shock without reducing the accuracy in other parts of the domain (figure 8.1b). Except in the vicinity of shocks, the results obtained in the two cases were observed to be identical. Thus, the fourth-order central difference ($c = \infty$) gives rise to spurious oscillations near shocks, but does not destroy the flow structure away from the shock nor the evolution of the flow afterwards. On the other hand the MUSCL-scheme in the $c = 0.2$ case apparently maintains sufficient accuracy in locations far away from the shock.

The flow is simulated on a uniform grid. From $t = 0$ to 80 it contains $240 \times 385 \times 144$ points, whereas from $t = 80$ until $t = 240$ the simulation is performed on a grid with $320 \times 513 \times 192$ points. A fourth-order accurate interpolation method is used to transfer the field at $t = 80$ to the finer grid. The accuracy in the linear regime has been checked by comparison with linear stability theory. Furthermore, calculations were also performed on coarser grids ($\frac{4}{3}$ times fewer points in each direction) and from $t = 160$ the simulation was also performed on a finer grid ($\frac{3}{2}$ times more points in the x_1-direction). These additional calculations established

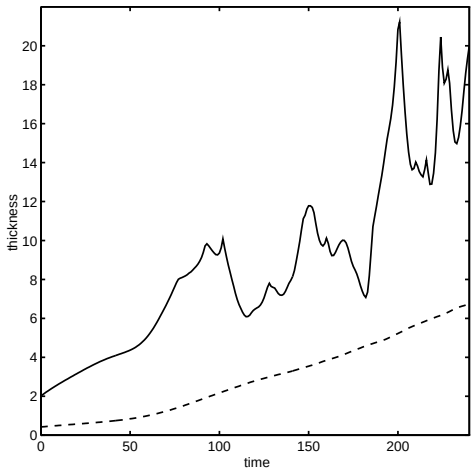

Figure 8.2: Evolution of vorticity thickness (solid) and momentum thickness (dashed).

the accuracy of the results presented in this paper. The demand for computer resources could substantially be reduced by exploiting the symmetries in the flow. Symmetries in the initial conditions are known to persist in time even after mixing transition (Moser & Rogers 1993; Luo & Sandham 1994) and we have verified this for the coarser grid simulations.

In the flow a transition to small scales is observed. At $t = 80$ the growth of the initial perturbation has saturated, nonlinear effects have set in and a Λ-vortex structure has developed. When time proceeds additional vortices are formed away from the central layer. These vortices break down into smaller vortices, and thus the flow undergoes a transition to small scale turbulence, similar to the flow at a convective Mach number of 0.8 (Luo & Sandham 1994). During this process the momentum thickness rapidly grows and is approximately linear in time (figure 8.2). At several times shock-waves are observed. The simulation is stopped at $t = 240$, since not far beyond this time the growth of the layer will slow down when the layer reaches the free-slip walls.

The Reynolds number (100) used in the simulation should not be much lower for shocks to occur. In a simulation with a lower Reynolds number (50) the mixing transition to small scales did not occur and no shocks were formed either. Thus the occurrence of shock-waves in the three-dimensional mixing layer appears to require a mixing transition to small scales. The flow is well-resolved, since the fall-off in the two-dimensional energy spectrum was about twelve orders of magnitude at most times throughout the simulation. Only at times when shocks

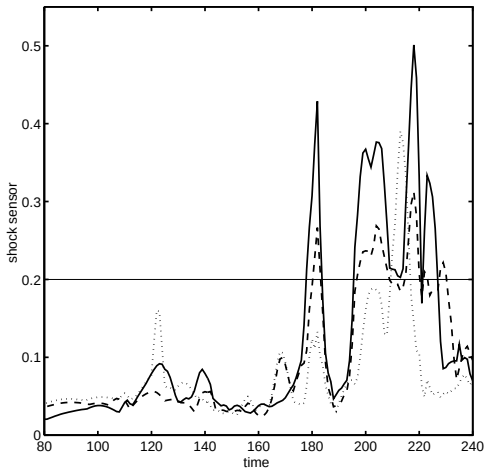

Figure 8.3: Evolution of the shock sensor s_i for $i = 1$ (solid), $i = 2$ (dashed) and $i = 3$ (dotted). The thin horizontal line corresponds to the threshold value c.

were present a fall-off of eight orders of magnitude was observed. Although these observations confirm that the resolution is sufficient, the calculations should not be performed on much coarser grids. For example, most of the shocks were not observed in a calculation performed on a $160 \times 257 \times 96$ grid.

8.2 Visualisation of shocks

The flow contains shock-waves in three distinct periods: t =121-123, t =181-183 and t =199-225. Since a shock corresponds to a large pressure difference in the direction perpendicular to the shock, it can be detected by examining the flow field at times where at least one of the components of ∇p shows a high peak. Furthermore, since shocks lead to a strong compression of the fluid, the dilatation $\nabla \cdot \mathbf{u}$ attains large negative values within a shock. We have identified the three periods using the shock-sensor s_i, based on the pressure gradient (figure 8.3). The shocks occurring in each period will be discussed in more detail below.

First, we investigate the shocks in the first period (t =121-123) and determine their origin. Maximum values of one of the components of the pressure gradient occur in the centre plane $x_2 = 0$. Figure 8.4a shows contour lines of the pressure in this plane at $t = 122$ and four shocks are observed. Since there are two symmetries in the centre plane, it is sufficient to consider the shock at the point (10.0,0.0,6.0). Because the shock contains strong gradients in the x_3-direction,

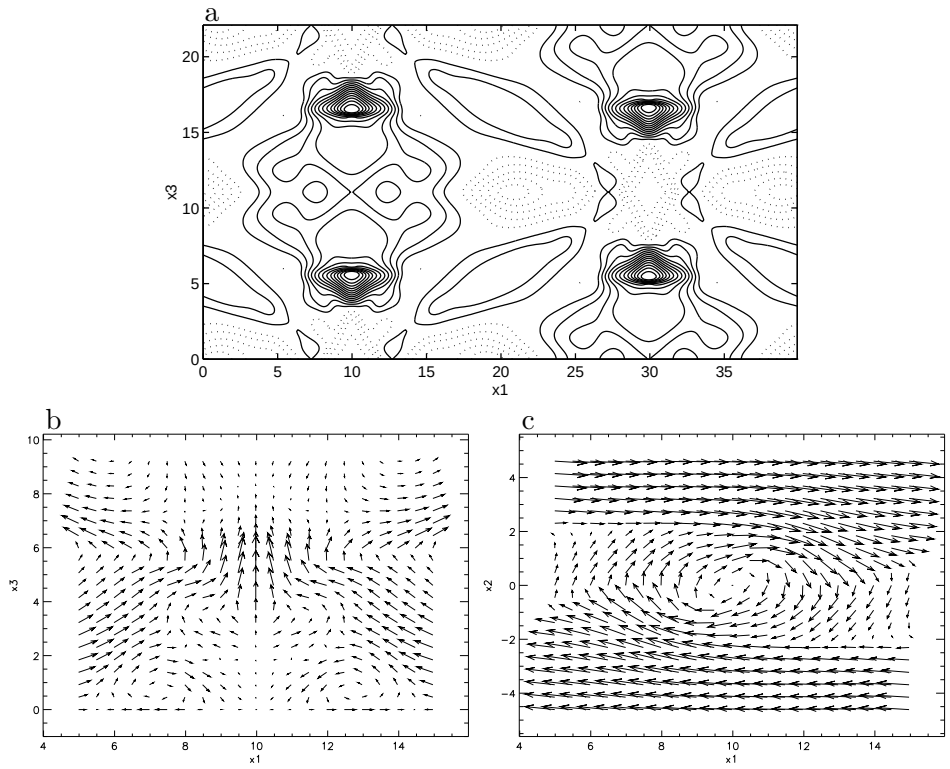

Figure 8.4: Contours of the pressure at $t = 122$ in the plane $x_2 = 0$ with $p < p_\infty$ (solid) and $p > p_\infty$ (dashed) with contour increment 0.025 (a). Velocity vectors at $t = 122$ in the plane $x_2 = 0$ (b) and in the plane $x_3 = 5.5$ (c). In order to reduce the density of the arrows, an arrow is plotted for only one in four grid-points in each direction.

we say that its orientation is in the x_3-direction. If the fluid passes through a shock the pressure jumps from a low to a high value. In general, low pressure regions correspond to the cores of vortices, whereas high pressure regions are associated with stagnation points. Figure 8.4b shows the velocity vectors in the plane $x_2 = 0$. The velocity vectors in figure 8.4c display a spanwise vortex in the plane $x_3 = 5.5$, which is in front of the shock. The axis of the vortex is at $x_1 = 10.0$. The spanwise vortex in front of the shock accelerates fluid along its axis in the x_3-direction. The acceleration is so strong that the velocity attains supersonic values and, hence, a shock is formed through which the fluid passes in order to reach the stagnation point. Therefore, this shock is created by a sucking vortex which accelerates the fluid along its axis. The shock exists for only a short

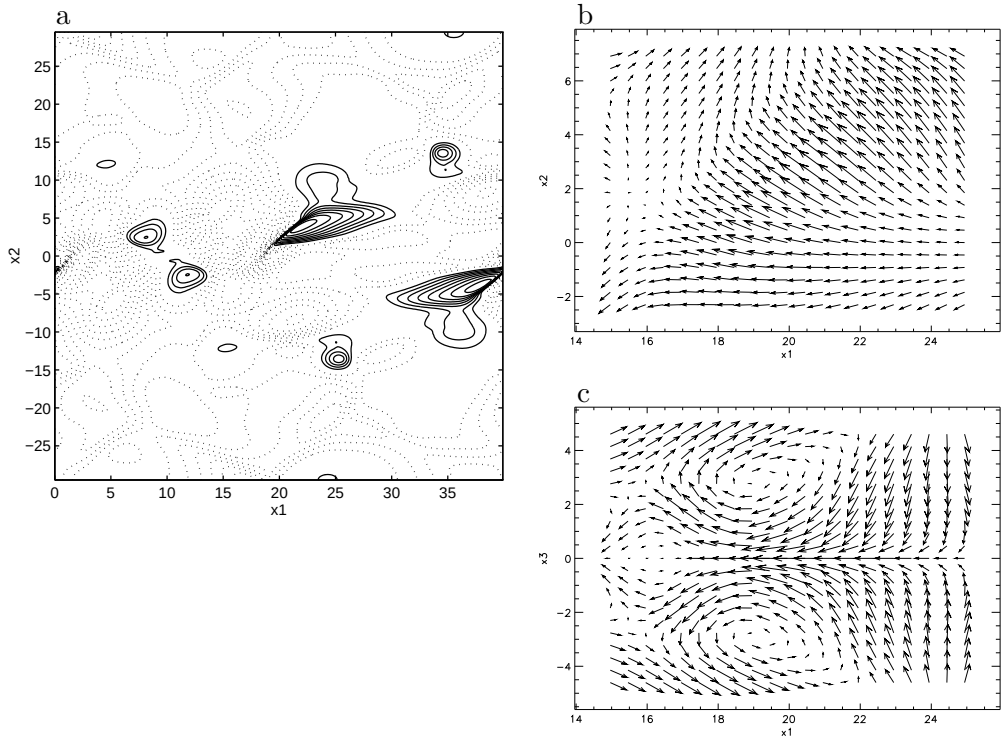

Figure 8.5: Pressure at $t = 182$ in the plane $x_3 = 0$ with $p < p_\infty$ (solid) and $p > p_\infty$ (dashed) with contour increment 0.025 (a). Velocity vectors at $t = 182$ in the plane $x_3 = 0$ (b) and in the plane $x_2 = 1.6$ (c).

time, since the turbulent flow structure changes rapidly.

Next, we verify the shock jump relations for stationary inviscid flow. The flow is instationary, but the speed of the shock is approximately zero during the period in which the shock exists. The simulation data for this shock yields an upstream Mach number $M_1 = 1.40$ and the ratios $p_2/p_1 = 2.10$ and $\rho_2/\rho_1 = 1.67$, where the subscripts 1 and 2 refer to the up- and downstream values respectively. The standard tables for normal shock-waves give 2.12 and 1.69 for the pressure and density ratios corresponding to $M_1 = 1.40$. The actual values are very close to these values, although the shock is viscous. In viscous flow shocks have a finite thickness and in our case the shock thickness is approximately 0.35, equal to three times the grid spacing.

The orientation, shape and related vortex structure of the shocks at $t = 182$ is different from $t = 122$. Figure 8.5a shows the pressure in the plane $x_3 = 0$,

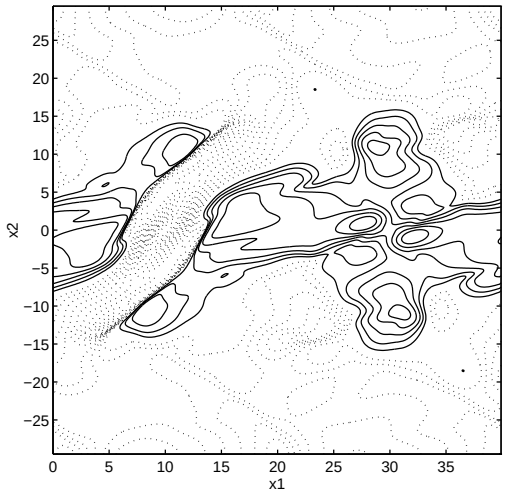

Figure 8.6: Pressure at $t = 200$ in the plane $x_3 = 3.9$ with $p < p_\infty$ (solid) and $p > p_\infty$ (dashed) with contour increment 0.025.

which contains the maximum pressure gradient at this time. The two shocks in this plane are symmetric and a similar pattern is found in the plane $x_3 = 11.05$. From the structures considered, the shock at this time is most similar to the recent experimental visualisation of a shock in a mixing layer (Papamoschou 1995). In order to study the flow structure around (18.5,1.6,0.0) in more detail, we turn to the velocity vector plots in the planes $x_3 = 0$ (figure 8.5b) and $x_2 = 1.6$ (figure 8.5c). Figure 8.5b shows that the streamwise velocity component through the shock is opposite to the upper free stream velocity. Two counter rotating vortices are observed in figure 8.5c. Not surprisingly, the velocity attains relatively high values in the region between these two vortices and becomes supersonic. A shock-wave occurs, since the velocity of the fluid has to be reduced in order to reach the stagnation point further downstream. Hence, the mechanism which creates shocks is not unique; at $t = 122$ the supersonic flow along the axis of a vortex creates a shock, whereas at $t = 182$ the supersonic flow between a pair of counter rotating vortices gives rise to a shock.

Shocks appear for the third time at $t = 200$ and this time the size is considerably larger than at the previous two periods. Figure 8.6 shows the pressure in the plane with maximum pressure gradient, $x_3 = 3.9$. The region enclosed by the pair of shocks is a high pressure region and contains a stagnation point. In this case the shocks fill a relatively large part of the domain and it is difficult to identify separate vortex structures which create the shocks.

The three-dimensional shape of the shocks at the three times is shown in

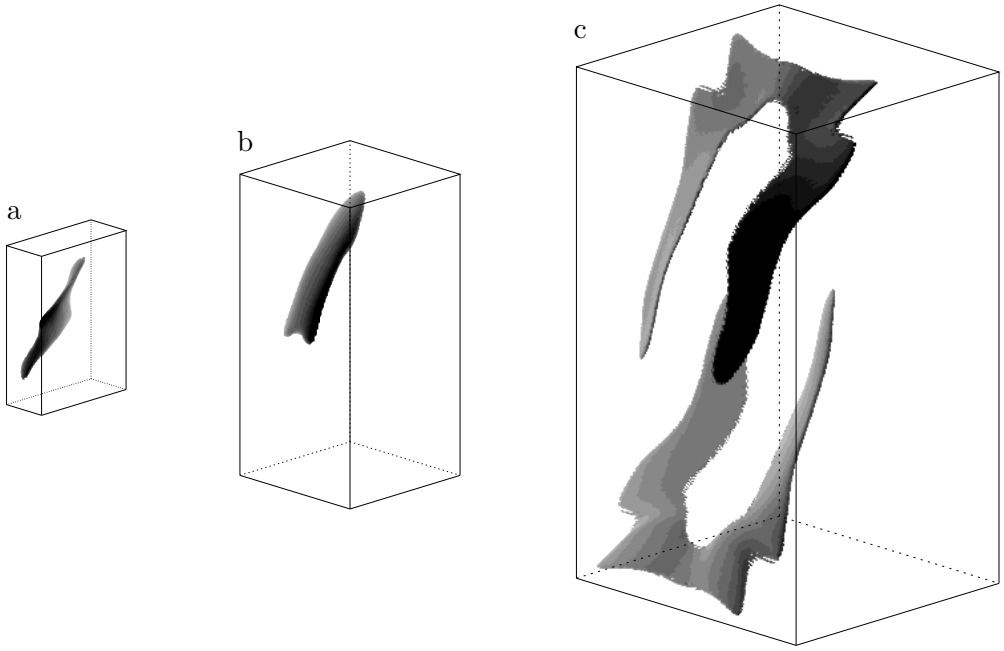

Figure 8.7: Surface $\nabla \cdot \mathbf{u} = -0.5$ showing the three-dimensional shape of the shocks at $t = 122$ (a), $t = 182$ (b) and $t = 200$ (c) in parts of the domain given by $[7.5, 12.5] \times [-3.7, 3.7] \times [4.6, 6.4]$ in (a), $[17.0, 22.9] \times [-6.5, 6.5] \times [-2.8, 2.8]$ in (b) and $[2.5, 17.5] \times [-14.8, 14.8] \times [-7.5, 7.5]$ in (c).

figure 8.7. The boxes are only parts of the computational domain and are centred around (10,0,5.5), (20,0,0) and (10,0,0), respectively. Due to the symmetries in the flow, these structures also appear at other locations. The structures at $t = 122$ and $t = 182$ appear at four locations and the pair of large shocks with a horse-shoe shape at $t = 200$ is also found centred around (30,0,11). The shocks at $t = 122$ and $t = 182$ persist only for a relatively short time. However, from $t = 200$ the flow contains shocks for a much longer time, until $t = 225$. During this period the structure shown in figure 8.7c changes and breaks down into several parts, while also new shocks appear with stronger gradients in the spanwise direction.

Finally, we consider the effect of shocks on the turbulent dissipation rate in the Reynolds-averaged approach. The turbulent dissipation rate is defined as $\epsilon = \overline{\sigma_{ij}\ \partial u_i''/\partial x_j}$, where σ_{ij} is the viscous stress tensor in compressible flow and the overbar and double prime denote the Reynolds average and Favre fluctuations respectively (see chapter 9). Sarkar *et al.* (1991) and Zeman (1990) separate the

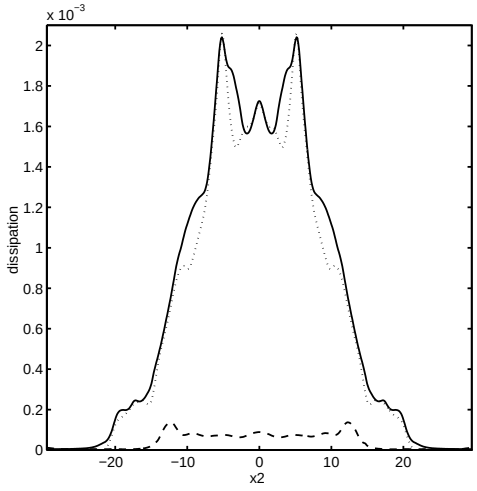

Figure 8.8: Profiles of the turbulent dissipation rate ϵ (solid), ϵ_s (dotted) and ϵ_d (dashed) at $t = 200$.

turbulent dissipation rate ϵ in a solenoidal part $\epsilon_s = \mu\overline{\omega_i''\omega_i''}/Re$, where ω_i'' denotes the fluctuating vorticity vector, and a dilatational part $\epsilon_d = \frac{4}{3}\mu\overline{(\nabla \cdot \mathbf{u}'')^2}/Re$. For convenience of notation we assume the viscosity μ to be constant. The decomposition $\epsilon = \epsilon_s + \epsilon_d$ is only valid in homogeneous turbulence, whereas in flows with one inhomogeneous direction (x_2),

$$\int \epsilon dx_2 = \int \epsilon_s dx_2 + \int \epsilon_d dx_2. \tag{8.2}$$

The dilatation dissipation is a pure compressibility effect. The contribution of ϵ_d is mainly due to shocks, since shocks can be identified with large negative values of the velocity divergence. Figure 8.8 shows the profiles of ϵ, ϵ_s and ϵ_d at $t = 200$, when the largest shocks occur. The locations $x_2 = \pm 12$, where the peaks the ϵ_d-profile occur, correspond to the planes in which the shocks are most pronounced. The dilatational fraction of the dissipation is less than 10 percent at $t = 200$ and even smaller at all other times. When shocks are absent the fraction is even less than 1 percent. Thus, the dilatation dissipation is increased by shocks, but it remains small compared to the total turbulent dissipation rate. The effects of compressibility on the turbulent statistics in the Reynolds average approach will be investigated in detail in the next chapter.

8.3 Conclusions

The compressible mixing layer at convective Mach number 1.2 has been simulated using DNS. With an initial perturbation of two equal and opposite oblique modes, the flow undergoes a transition to small scales. The turbulent flow contains instantaneous shocks at several times. A combined fourth-order central difference/ third-order upwind method has been introduced in order to accurately represent both the turbulence and the shocks. The numerical database has been analysed in detail at the times when shocks appear. Different types of turbulent vortices that generate the shocks have been identified: a vortex which accelerates fluid along its axis and a pair of counter rotating vortices. Furthermore, the solenoidal and dilatational part of the turbulent dissipation have been calculated. The dilatation dissipation, which is mainly due to shocks, is always less than 10 percent of the total turbulent dissipation.

Chapter 9

Compressible mixing layer growth rate and turbulence characteristics

An early experimental observation of the effect of Mach number on turbulence was the reduction in growth rate of the plane mixing layer (Birch & Eggars 1973). In this thesis mixing layers with equal free-stream densities are considered, but many experimental results in literature apply to mixing layers with a different density ratio (the ratio between upper and lower free-stream density). It has been established that intrinsic compressibility rather than density ratio effects are responsible for the growth rate reduction (Brown & Roshko 1974, Bradshaw 1977, Papamoschou & Roshko 1988). In recent years there have been several experimental, numerical and theoretical studies of compressible turbulence which have added considerably to knowledge in this area (see Lele 1994 for a review), but a convincing explanation of the reduced growth rate effect has been elusive. In this chapter[1] Direct Numerical Simulation databases are used to study the effect of compressibility on mixing layers.

A single compressibility parameter, the convective Mach number M (Bogdanoff *et al.* 1983, see also section 1.2), is sufficient to represent the experimental growth rate data to a reasonable accuracy with a single curve. A collection of the experimental results can be found in Lele (1994). In order to represent the experimental growth rate data with a single curve the growth rates are normalised by the incompressible growth rate at the same density ratio. One problem with the

[1]The work presented in this chapter was performed at the Department of Aeronautical Engineering, Queen Mary and Westfield College, London, in collaboration with dr. N.D. Sandham and dr. K.H. Luo, who also significantly contributed to the resulting paper Vreman *et al.* 1995h, which is the basis of this chapter.

growth rate normalisation is the lack of an accurate model for the incompressible growth rate as a function of density ratio, which leads to quite a large scatter in the normalised growth rates (Sandham & Reynolds 1989, Lu & Lele 1993). However, all the data show a large reduction in growth rate between $M = 0.4$ and $M = 0.8$. There is also evidence that the turbulence structure changes as M increases. Flow visualisations (Clemens & Mungal 1992, 1995) at high Reynolds numbers show how the low-Mach-number organised structure is lost as compressibility becomes important. Experiments by Elliot & Samimy (1990) show that turbulence fluctuations and Reynolds stresses decrease as M is increased.

In recent years, several explanations of compressibility effects have been offered. Zeman (1990, 1991) proposed that the dilatational part of the total dissipation becomes progressively important as the turbulent Mach number increases due to the appearance of eddy-shocklets (shock-waves). He modelled dilatation dissipation as proportional to the solenoidal dissipation and a function of the turbulent Mach number M_t and the kurtosis of the velocity field. By incorporating the model for dilatation dissipation into a second-moment closure formulation, he was able to obtain the growth rate reduction as M increased. However, eddy-shocklets have not been observed in experiment or Direct Numerical Simulation below a convective Mach number of one (we exclude two-dimensional simulations, which have shown shocks above $M = 0.7$) and thus there is no physical basis for dilatation dissipation being important in the key region of M where the growth rate is reduced. Furthermore, at a higher convective Mach numbers ($M = 1.2$), eddy-shocklets were found (chapter 8), but the dilatation dissipation was small even at times when eddy-shocklets were present. Sarkar *et al.* (1991) and El Baz & Launder (1993) have also used models for dilatation dissipation to get the growth rate reduction. However, more recently, Sarkar (1995) has commented that there has been no direct validation of the concept for the mixing layer.

It has been observed that results for the growth rate of small disturbances in laminar compressible shear flow match the reduction in growth rate of the fully-developed turbulent flow (see e.g. Sandham & Reynolds 1990). This is a remarkable result and suggests that in some way the physical mechanisms in the turbulent flow are echoed in the linear regime. One would want an explanation of the reduced growth rate of mixing layers to be applicable to small disturbances as well as to the turbulent flow. This is certainly not the case for any theories based on changes in dissipation, as the linear results are obtained from inviscid stability theory, where the dissipation is zero.

Breidenthal (1990) proposed a sonic-eddy model for compressible turbulence based on the assumption that only eddies whose eddy Mach number M_e is unity are efficient in mixing. The eddy Mach number is based on the velocity difference across an eddy. The Kolmogorov spectrum of eddy scales would exist for all

subsonic eddies ($M_e < 1$). According to this model, the normalised shear layer mixing rate (growth rate) is a function of the global Mach number $M_\delta = \delta/\lambda = \Delta U/c$, where λ is a sonic-eddy size, δ the largest eddy scale, ΔU the characteristic global eddy speed and c the speed of sound. A sudden drop in growth rate is predicted at $M_\delta = 1$ when the largest eddies become sonic. Further transitions occur at very high Mach numbers when the turbulence micro-scale becomes equal to the mean free path and when the shear layer width becomes comparable with the mean free path. The model is conceptually important, but does not give quantitative information on growth rate or turbulence structure.

Up until very recently Direct Numerical Simulation (DNS) of the compressible mixing layer had been limited to the early stages of vortex formation (Sandham & Reynolds 1991). These revealed changes in typical eddy structure but did not contain small scales of turbulence. Recent work (Luo & Sandham 1994, 1995; Vreman *et al.* 1994f, 1995bfg (chapters 5,7 and 8)) has succeeded in simulating compressible flows through a mixing transition to small-scale turbulence. In this chapter we analyse turbulence data from these simulations to address the influence of compressibility on this building-block inhomogeneous flow problem. In section 9.1 we describe the DNS-databases that were used in the study. The averaging procedure and statistical equations are given in section 9.2, and used to explain the growth rate reduction and anisotropy effects in section 9.3. The results are discussed in section 9.4.

9.1 Direct Numerical Simulations

The temporal mixing layer with equal and opposite free-stream velocities has been simulated by Direct Numerical Simulation (DNS) of the compressible Navier-Stokes equations. The database covers four different convective Mach numbers: $M = 0.2$, 0.6, 0.8 and 1.2. Details of the $M = 0.2$, 0.6 and 1.2 cases are given in chapter 5,7 and 8 respectively and those of $M = 0.8$ in Luo & Sandham (1994, 1995). Characteristic numbers are given in table 9.1. In all cases the flow is simulated in a rectangular domain $[0, L_1] \times [-\frac{1}{2}L_2, \frac{1}{2}L_2] \times [0, L_3]$. The boundary conditions in the homogeneous directions (x_1 and x_3) are periodic, whereas the boundaries in the normal direction (x_2) are treated with characteristic non-reflecting conditions in the $M = 0.8$ case and as free-slip walls in the other cases. The non-dimensionalisation procedure and initial mean profile have been described in chapters 1 and 2. Perturbations obtained from linear stability theory are superimposed on the mean profile. The most unstable mode is two-dimensional for M up to 0.6, but three-dimensional for higher M. Therefore the $M = 0.2$ and 0.6 cases contain two- and three-dimensional initial disturbances as described in section 5.1. For $M = 0.8$ and 1.2 the primary instability is three-

M	Re	L_1	L_2	L_3	grid	scheme
0.2	50	59.0	59.0	59.0	$192 \times 193 \times 192$	finite difference
0.6	50	68.0	59.0	68.0	$192 \times 193 \times 192$	finite difference
0.8	140	26.7	60.0	26.7	$144 \times 221 \times 160$	Fourier/Padé
1.2	100	39.9	59.0	22.1	$320 \times 513 \times 192$	finite difference/upwind

Table 9.1: Specification of the DNS-databases: Mach number, Reynolds number, computational box size, grid and spatial discretization.

dimensional, so only a single pair of equal and opposite oblique modes is used (section 8.1). In these cases the symmetry in the initial conditions is used to reduce computing time and storage requirements. The initial amplitude of the instability waves is small for $M = 0.8$ (0.025), whereas the other simulations use large-amplitude disturbances (typically 0.1). If the initial amplitude is small, the Reynolds number has to be relatively high to trigger the transition to turbulence.

Numerical details are summarised in table 9.1. In each case the numerical method is fully explicit with Runge-Kutta integration in time. With respect to spatial derivatives, the $M = 0.2$ and 0.6 cases use scheme B, the $M = 1.2$ case uses a combination of scheme B and D (section 8.1) and the $M = 0.8$ case employs a Fourier collocation scheme in the periodic directions and a Padé scheme in the normal direction (Sandham & Reynolds 1991; Luo & Sandham 1994). The accuracy of the simulations has been verified by running simulations on coarser grids. Furthermore, coarser grid simulations without exploitation of the symmetry conditions demonstrated that the initial symmetry was preserved throughout the whole simulation in the $M = 0.8$ and 1.2 cases. Therefore, the symmetry conditions can be exploited to decrease the computational cost without affecting the results.

The evolution of the momentum thickness δ (defined in the next section) for the cases considered is shown in figure 9.1. The later stages of the simulations are characterized by a strong growth of the momentum thickness, which is approximately linear with time. The growth rate δ' equals the slope of the curve in this regime. The momentum thickness will only display exact linear growth if the mixing layer is self-similar. Self-similarity is hard to achieve with DNS since the computational domain in the homogeneous directions is finite. This reduces the statistical sample size and eventually restricts the growth of large scale structures. Approximate values for the growth rate δ' have been obtained from figure 9.1 for δ between 2 and 5, giving growth rate of 0.072, 0.058, 0.038 and 0.030 at $M = 0.2$, 0.6, 0.8 and 1.2 respectively. The growth rate at $M = 1.2$ is about 40% of its value at $M = 0.2$ which is in broad agreement with the reduction found experimentally.

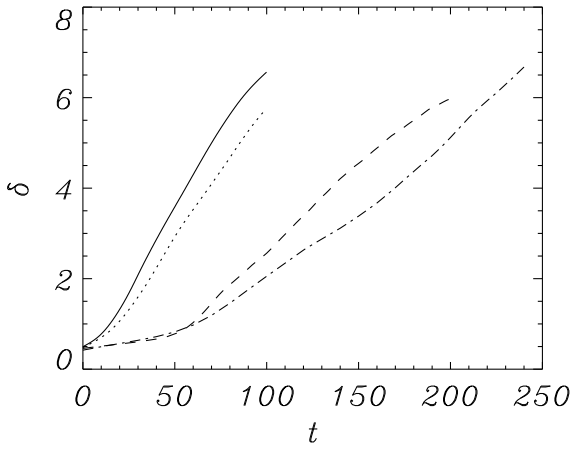

Figure 9.1: Graph of momentum thickness against time for Mach numbers $M = 0.2$ (solid line), 0.6 (dotted), 0.8 (dashed), 1.2 (chain dotted).

In each simulation a transition to small scales is observed. The scenario of the transition at $M = 0.2$ is very close to that of the incompressible mixing layer. The two-dimensional instability leads to the formation of four rollers with spanwise vorticity. These rollers undergo pairing processes until finally one roller structure containing many small-scale structures fills the domain (see chapter 5). The three-dimensional waves also grow and form Λ-shaped vortices and break down into small-scale motions. For the $M = 0.6$ case the scenario is roughly the same, but the two-dimensional roller structure is less pronounced and can hardly be recognised anymore in the turbulent regime. In the $M = 0.8$ case the primary three-dimensional instability forms Λ-shaped vortices, which initiate the mixing transition towards small scales. More details about the vortex structures in this simulation are given by Luo & Sandham (1994). The structures in the simulation at $M = 1.2$ are similar to those at $M = 0.8$, but in addition eddy-shocklets form (see chapter 8). Although we do not have exactly self-similar data, we do have a cascade to small scales and resolve the dissipation at the smallest scales. When turbulent quantities are averaged over a number of samples corresponding to different times we have a reasonable approximation to the statistics of a self-similar mixing layer.

In the simulation at $M = 1.2$ shocks were found at three times: $t = 122$, $t = 182$ and $t = 200$ (chapter 8). Near $t = 122$ and $t = 182$ the shocks exist for only a few time units, but from $t = 200$ to $t = 225$ the flow is never free from shocks. As shocks had not been observed before in three-dimensional

computations, the $M = 1.2$ calculation was repeated with the compact finite difference/characteristic boundary condition code until approximately $t = 160$. Although the differences in the boundary conditions led to slightly different results, shock waves were still observed in the simulation.

9.2 Data reduction and analysis

In this section we use an analysis of integrated equations for the Reynolds stresses to study the changes in turbulence characteristics as the Mach number is increased. In subsection 9.2.1 we derive a new mathematical relation between growth rate and integrated turbulent production starting from the Reynolds-Averaged Navier-Stokes equations. The integrated Reynolds stress transport equations are presented in subsection 9.2.2. We calculate the magnitude of each term from the DNS-databases and establish that the so-called dilatational terms are not important.

9.2.1 The relation between growth rate and turbulent production

The statistical description of turbulence is based on the Reynolds-Averaged Navier-Stokes equations (Tennekes & Lumley 1972). The differences between the statistical approach and LES are determined by the averaging operator, which is the ensemble average in the statistical approach and a local filter in LES (chapter 1). In compressible flow the flow variables in the Reynolds-Averaged Navier-Stokes equations are written as

$$\rho = \overline{\rho} + \rho', \tag{9.1}$$
$$p = \overline{p} + p', \tag{9.2}$$
$$u_i = \widetilde{u}_i + u_i''. \tag{9.3}$$

In this notation $\overline{\rho}$, $\overline{p}$ and $\widetilde{u}_i$ represent the mean flow, whereas ρ', p' and u_i'' are the corresponding fluctuations. The bar denotes the ensemble average. The tilde refers to Favre averaging, defined by $\widetilde{u}_i = \overline{\rho u}_i/\overline{\rho}$. The Reynolds-averaged continuity and momentum equations have the following form:

$$\partial_t \overline{\rho} = -\partial_j(\overline{\rho}\widetilde{u}_j), \tag{9.4}$$
$$\partial_t(\overline{\rho}\widetilde{u}_i) = -\partial_j(\overline{\rho}\widetilde{u}_i\widetilde{u}_j) - \partial_i\overline{p} + \partial_j\overline{\sigma}_{ij} - \partial_j\overline{\rho u_i'' u_j''}. \tag{9.5}$$

The last term in the momentum equation contains the Reynolds stress tensor, which results from averaging the nonlinear convective term. Reynolds-averaged variables in a temporal shear layer are functions of t and the normal coordinate

x_2 only, and are obtained by averaging the original variables in the homogeneous streamwise and spanwise directions.

The momentum thickness in a temporal compressible mixing layer is defined as:

$$\delta(t) = \frac{1}{\rho_1(\Delta U)^2} \int \overline{\rho}(U_1 - \widetilde{u}_1)(\widetilde{u}_1 - U_2)dx_2, \tag{9.6}$$

where ρ_1 is the upper free-stream density, U_1 and U_2 are the upper and lower free-stream velocities respectively and $\Delta U = U_1 - U_2$. (In our simulations $U_1 = 1$, $U_2 = -1$ and $\rho_1 = 1$). Equation (9.6) expresses the definition for general compressible mixing layers, whereas the definition in section 5.3.7 is for a specific case. The integration in equation (9.6) is between the free-slip walls for the confined case, while it extends from minus to plus infinity for the unconfined case. There is no unique way to define the thickness of a shear layer, but the thickness defined by equation (9.6) is generally regarded as an appropriate measure and has been widely used (Brownand & Latigo 1979; Ragab & Sheen 1992; Rogers & Moser 1994). An expression for the growth rate of the shear layer is obtained by differentiating equation (9.6):

$$\delta' = \frac{d\delta}{dt} = \frac{U_1 + U_2}{\rho_1(\Delta U)^2} \int \partial_t(\overline{\rho}\widetilde{u}_1)dx_2 - \frac{1}{\rho_1(\Delta U)^2} \int \partial_t(\overline{\rho}\widetilde{u}_1\widetilde{u}_1)dx_2. \tag{9.7}$$

The first term at the right-hand side is zero as can be observed from the x_2-integrated mean momentum equation (9.5) for the streamwise direction. Since equation (9.5) is in conservative form, the right-hand side vanishes after integration in the x_2-direction if $\tilde{u}_2 = 0$ and $\partial_2\tilde{u}_1 = 0$ at the boundaries in the normal direction. With respect to the last term in equation (9.7), we consider the evolution of twice the mean flow kinetic energy, given by

$$\begin{aligned} \partial_t(\overline{\rho}\widetilde{u}_1\widetilde{u}_1) &= \partial_2(-\overline{\rho}\widetilde{u}_1\widetilde{u}_1\widetilde{u}_2 + 2\overline{\sigma}_{12}\widetilde{u}_1 - 2\overline{\rho u_1'' u_2''}\widetilde{u}_1) \\ &\quad +2\overline{\rho u_1'' u_2''}\partial_2\widetilde{u}_1 - 2\overline{\sigma}_{12}\partial_2\widetilde{u}_1, \end{aligned} \tag{9.8}$$

where $\overline{\sigma}_{12}$ is the viscous stress tensor. After integration the conservative terms vanish and hence the growth rate satisfies

$$\delta' = \frac{2}{\rho_1(\Delta U)^2}[\int(-\overline{\rho u_1'' u_2''}\partial_2\widetilde{u}_1)dx_2 + \int(\overline{\sigma}_{12}\partial_2\widetilde{u}_1)dx_2]. \tag{9.9}$$

The first integral is the integrated turbulent production term, whereas the second integral represents the molecular dissipation of the mean flow. In the turbulent regime the latter can be neglected compared to the former and, consequently, the expression for the growth rate reduces to

$$\delta' = -\frac{2}{\rho_1(\Delta U)^2} \int(\overline{\rho u_1'' u_2''}\partial_2\widetilde{u}_1)dx_2. \tag{9.10}$$

Thus, the growth rate of time-developing turbulent mixing layers is proportional to the integrated turbulent production.

The relation between growth rate and production can be extended to spatial mixing layers under certain conditions. The convection speed in a spatial mixing layer is defined as $U_c = \frac{1}{2}(U_1 + U_2)$. We apply the following transformation: $x_1^* = x_1 - U_c t$, $x_2^* = x_2$, $x_3^* = x_3$ and $t^* = t$. The Navier-Stokes equations are invariant under such a Galilean transformation. In this new frame of reference the spatial momentum thickness $\delta(x_1)$ can be written as $\delta^*(U_c t^*)$ and, consequently, the spatial growth rate satisfies:

$$\frac{d\delta}{dx_1} = \frac{1}{U_c}\frac{d\delta^*}{dt^*}. \tag{9.11}$$

Equation (9.10) can be used for $d\delta^*/dt^*$ if we assume that terms with $\partial/\partial x_1^*$ are much smaller than terms with $\partial/\partial x_2^*$. This provides a relation between growth rate and integrated turbulent production for self-similar spatial mixing layers.

9.2.2 The integrated Reynolds stress transport equations

To exploit the connection between growth rate and integrated production we consider the x_2-integrated Reynolds stress transport equations. The Reynolds stress equations for compressible flow in their general form are given by Blaisdell *et al.* (1991). The terms in divergence form vanish after integration, hence the equation for the (ij)-component of the integrated Reynolds stress becomes:

$$\frac{d}{dt}\int \overline{\rho u_i'' u_j''} dx_2 = P_{ij} + \Pi_{ij} - \epsilon_{ij}, \tag{9.12}$$

where

$$P_{ij} = -\int (\overline{\rho u_i'' u_2''}\partial_2 \widetilde{u}_j + \overline{\rho u_j'' u_2''}\partial_2 \widetilde{u}_i) dx_2, \tag{9.13}$$

$$\Pi_{ij} = \int \overline{p(\partial_j u_i'' + \partial_i u_j'')} dx_2, \tag{9.14}$$

$$\epsilon_{ij} = \int (\overline{\sigma_{ik}\partial_k u_j''} + \overline{\sigma_{jk}\partial_k u_i''}) dx_2, \tag{9.15}$$

which represent the integrated production, pressure-strain and dissipation tensors, respectively. Note that equation (9.10) implies

$$P_{11} = \rho_1 (\Delta U)^2 \delta', \tag{9.16}$$

where $\Delta U = 2$ in our normalisation. In a self-similar mixing layer the growth rate and, consequently, the integrated production is constant. Therefore, like Rogers

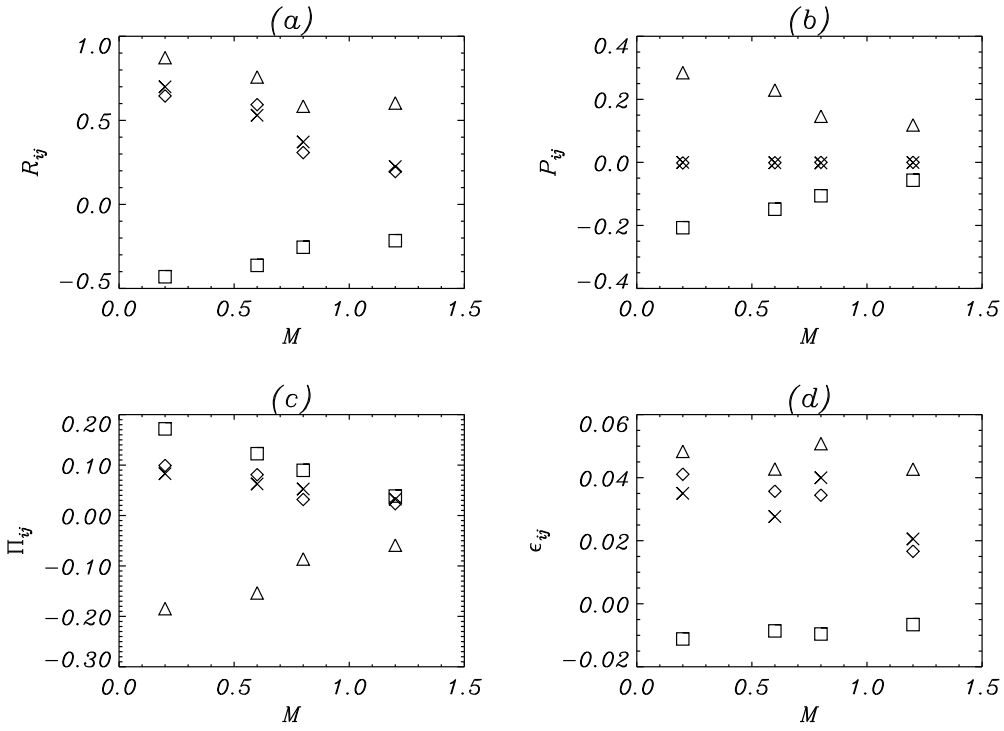

Figure 9.2: Integrated turbulence statistics: (a) Reynolds stress R_{ij}, (b) production P_{ij}, (c) pressure-strain Π_{ij} and (d) dissipation ϵ_{ij}. Components are denoted with triangles (11), crosses (22), diamonds (33) and squares (12).

& Moser (1994), we argue that in a self-similar stage the terms of equation (9.12) are independent of time and scale with $\rho_1(\Delta U)^3$. Self-similarity also implies that the values of the Reynolds-stress in the centre of the mixing layer have reached a constant level, whereas the width of the profiles grows with δ. Therefore, we define

$$R_{ij} = \frac{1}{\delta} \int \overline{\rho u_i'' u_j''} dx_2, \tag{9.17}$$

which will be independent of time in the self-similar stage and will scale with $\rho_1(\Delta U)^2$. Hence, the Reynolds stress equations reduce to an algebraic system

$$\delta' R_{ij} = P_{ij} + \Pi_{ij} - \epsilon_{ij}. \tag{9.18}$$

The values for the tensors R_{ij}, P_{ij}, Π_{ij} and ϵ_{ij} have been plotted against Mach number in figure 9.2. Since we do not have exact self-similarity at every

time, the values in figure 9.2 have been averaged over a number of samples in the region with approximately linear growth of the momentum thickness (figure 9.1). The contributions of the (1,3) and (2,3) components of the Reynolds stress have not been plotted since they are negligible compared to the other components. Figure 9.2a shows that the anisotropy of the Reynolds stresses increases with Mach number. From figure 9.2b, the production terms P_{22} and P_{33} are zero, which is expected since the only significant mean velocity derivative, $\partial_2 \widetilde{u}_1$, does not appear in these terms. Retaining only the significant terms, the system given by (9.18) and (9.16) reduces to

$$\delta' R_{11} = 4\delta' + \Pi_{11} - \epsilon_{11}, \tag{9.19}$$

$$\delta' R_{22} = \Pi_{22} - \epsilon_{22}, \tag{9.20}$$

$$\delta' R_{33} = \Pi_{33} - \epsilon_{33}, \tag{9.21}$$

$$\delta' R_{12} = P_{12} + \Pi_{12} - \epsilon_{12}. \tag{9.22}$$

The pressure-strain term Π_{11} is negative, while Π_{22} and Π_{33} are positive. Thus, pressure-strain acts to redistribute energy from the streamwise into the normal and spanwise fluctuations. We remark that the pressure-dilatation $\frac{1}{2}\Pi_{kk}$ is approximately zero, even at the highest M. The dissipation component ϵ_{11} does not decrease with increasing Mach number as much as the other two components. Thus, the dissipation in our simulations is less isotropic at higher Mach numbers. The diagonal components of the dissipation tensor are considerably larger than ϵ_{12}, although the latter is not zero.

Dilatation dissipation and pressure-dilatation are of interest because of their possible use in explaining compressibility effects. The total integrated dissipation $\epsilon = \epsilon_{kk}/2$ can be split as $\epsilon = \epsilon_s + \epsilon_d$, where ϵ_s is a solenoidal part and ϵ_d is a dilatational part. In figure 8.8 we have shown profiles of the components of dissipation against x_2, whereas we consider integrated profiles here. The integrated form of the dilatational dissipation is

$$\epsilon_d = \int \frac{4}{3}\frac{\widetilde{\mu}}{Re}\overline{(\nabla \cdot \mathbf{u}'')^2} dx_2. \tag{9.23}$$

We consider the highest Mach number case $M = 1.2$ and on figure 9.3 show the integrated total dissipation, dilatation dissipation and pressure dilatation as functions of time. The dilatational part of the dissipation is very small even in the stages of the simulation which contain eddy-shocklets. The pressure-dilatation is somewhat larger, but it changes sign a number of times and is also not significant compared to the total dissipation. These two dilatational terms are even smaller in the cases with lower convective Mach number which do not contain eddy-shocklets. Eddy-shocklets do increase the dilatational terms, but compared to the total dissipation their contributions are too small to explain the growth rate

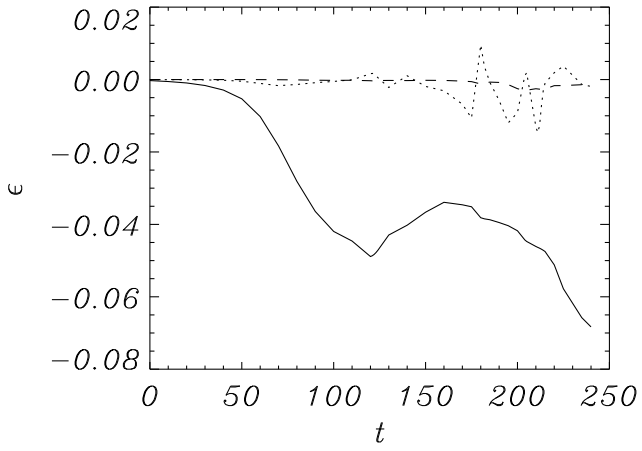

Figure 9.3: Comparison of the magnitudes of total dissipation (solid line) with dilatation dissipation (dashed line) and pressure-dilatation (dotted line) during the simulation at $M = 1.2$.

reduction. The production and pressure-strain rate terms are much more affected by compressibility than the dissipation and, consequently, the reduced growth rate must be explained from these terms.

9.3 Modelling the effect of compressibility

In this section we identify the key terms contributing to the reduced growth rate and build a complete model for the integrated Reynolds stress equations using a deterministic model for pressure fluctuations and models for turbulence anisotropy. In subsection 9.3.1 we argue that the mixing layer growth rate would be proportional to the rapid pressure-strain term if the turbulence were isotropic. Furthermore, the rapid pressure-strain term is expressed in the pressure extrema. In subsection 9.3.2, we model the pressure extrema as functions of the convective Mach number, using a compressible vortex model and the sonic-eddy concept. Thus, the isotropic model is completed, which gives a good qualitative prediction of the growth rate reduction. However, it predicts too low growth rates at high Mach numbers. In subsection 9.3.3 we correct the isotropic model taking anisotropy effects into account to obtain a better quantitative prediction of the growth rate reduction. To represent the anisotropy effects, we adopt a certain amount of turbulence modelling in order to arrive at a closed algebraic equation for the growth rate.

9.3.1 The significance of pressure-strain

In the following subsections we explain the reduced growth rate of the mixing layer by consideration of a necessary adjustment in pressure fluctuations as the Mach number is increased. A reformulation in terms of anisotropy is useful. We define the Reynolds stress anisotropy as

$$b_{ij} = \frac{R_{ij} - (2/3)k\delta_{ij}}{k} \tag{9.24}$$

and the dissipation anisotropy as

$$e_{ij} = \frac{\epsilon_{ij} - (2/3)\epsilon\delta_{ij}}{\epsilon}, \tag{9.25}$$

where $k = R_{qq}/2$ and $\epsilon = \epsilon_{qq}/2$ are respectively the turbulence kinetic energy and dissipation. With the assumption that we can neglect the pressure-dilatation term in the kinetic energy equation, the integrated equations for the diagonal terms reduce to

$$\delta'(b_{11}k - 8/3) = \quad \Pi^R_{11} + \Pi^S_{11} - e_{11}\epsilon, \tag{9.26}$$

$$\delta'(b_{22}k + 4/3) = \quad \Pi^R_{22} + \Pi^S_{22} - e_{22}\epsilon, \tag{9.27}$$

$$\delta'(b_{33}k + 4/3) = \quad \Pi^R_{33} + \Pi^S_{33} - e_{33}\epsilon, \tag{9.28}$$

where we have included the usual split of the pressure-strain term into a rapid part Π^R and a slow part Π^S (see e.g. Speziale *et al.* 1991). The rapid part is associated with the mean strain rate, while the slow part is associated with the process of return to isotropy. The Reynolds stress anisotropy term is usually small compared to 8/3 or 4/3. The dissipation anisotropy term is small compared to the other terms. This results in a proportionality between the growth rate and the diagonal pressure-strain components, which is confirmed by the data (figure 9.2). If the turbulence were isotropic we would have direct proportionality between the rapid pressure-strain term and the mixing layer growth rate.

It is proposed that the main effect of compressibility comes from modified pressure fluctuations. That the pressure fluctuation must change is evident when one considers that the typical pressure fluctuations in incompressible flow, normalised by $\rho_1 U_1^2$ would lead to negative pressures in high Mach number flow, since the free-stream pressure drops relative to $\rho_1 U_1^2$ as $1/(\gamma M^2)$. Thus, we propose to model Π^R_{11} as:

$$\Pi^R_{11} = p^*(M)(\Pi^R_{11})_{M=0}, \tag{9.29}$$

where $p^*(M)$ contains the effect of reduced pressure fluctuations. In the isotropic approximation the mixing layer growth rate would be proportional to $p^*(M)$.

To estimate $p^*(M)$ we assume that

$$p^*(M) = \frac{(p_{max} - p_{min})_M}{(p_{max} - p_{min})_0}, \tag{9.30}$$

where p_{max} and p_{min} will be estimated from a deterministic model of large vortex structures in compressible shear flow, assumed to be representative of the typical eddies that contribute to the rapid pressure-strain term.

9.3.2 Deterministic model for pressure extrema

Pressure minima in a flow can be identified with the cores of vortices, whereas pressure maxima occur at stagnation points. We present a model for the pressure minima first. A common description of a region of rotating fluid is the Oseen vortex, which has been used before to represent vortices in mixing layers (Papamoschou & Lele 1992). It assumes axisymmetric flow with the tangential velocity given by

$$v_\theta = \frac{\Gamma}{2\pi r}(1 - e^{-\alpha r^2/R^2}), \tag{9.31}$$

where Γ is the circulation, R is the vortex size, and $\alpha = 1.256$ is chosen such that $v_\theta = v_{\theta,max}$ at $r = R$.

In order to obtain the pressure minimum we turn to the inviscid radial momentum equation:

$$-\frac{1}{\rho}\frac{\partial p}{\partial r} = \frac{v_\theta^2}{r}. \tag{9.32}$$

To include the effects of density variation on the pressure field inside a vortex we need a model for the thermodynamics. Isentropic flow is not a possibility. However we observe from two-dimensional simulations (Sandham & Reynolds 1989) at $M = 0.6$ that the temperature changes inside vortices developing in temporal mixing layers are only 7% relative to the free stream, compared with fluctuations of 40-50% for the density and pressure. With the assumption of isothermal flow we can integrate (9.32) to get

$$\frac{p_{min}}{p_\infty} = e^{-(\gamma A v_{\theta,max}^2/c_\infty^2)}, \tag{9.33}$$

where $c_\infty = (\gamma p_\infty/\rho_\infty)^{\frac{1}{2}}$ is the free-stream speed of sound and

$$A = \frac{1}{v_{\theta,max}^2}\int_0^\infty \frac{v_\theta^2}{r} dr. \tag{9.34}$$

We assume that A is a constant, equal to 1.69 for the Oseen vortex.

The pressure drop is then a function of the maximum tangential velocity in a vortex, $v_{\theta,max}$. A logical value for $v_{\theta,max}$ is half the velocity difference,

$$v_{\theta,max} = \tfrac{1}{2}\Delta U, \tag{9.35}$$

which gives rise to a pressure drop of $p_{\min} - p_\infty = -A\rho_\infty(\frac{1}{2}\Delta U)^2$ for incompressible mixing layers (obtained from (9.33) for $M \to 0$). For compressible flows we define an eddy Mach number based on the velocity difference across the eddy,

$$M_e = \frac{2v_{\theta,max}}{c_\infty} = \frac{4v_{\theta,max}}{\Delta U}M, \tag{9.36}$$

where M is the convective Mach number. If equation (9.35) were used for all Mach numbers, M_e would become larger than unity for $M > 0.5$. However, the conceptual 'sonic-eddy' model of Breidenthal (1990) implies that only eddies with $M_e < 1$ play a role in the turbulent energy cascade in a compressible flow. It is therefore proposed that the following model be used for $v_{\theta,max}$:

$$v_{\theta,max} = \min(1, \frac{M_{crit}}{M})\tfrac{1}{2}\Delta U. \tag{9.37}$$

M_{crit} is the critical Mach number beyond which $v_{\theta,max}$ is affected by compressibility. The value $M_{crit} = 0.5$ corresponds to the sonic-eddy model in which the largest eddies satisfy $M_e = 1$. Without the sonic-eddy model we find that the pressure in the vortex cores would drop down to near zero pressure, which is not observed in the simulation results.

Next we turn to the prediction of the pressure maxima which corresponds to stagnation points. Isentropic flow is a good approximation for the fluid on a stream line towards a stagnation point and the standard relation yields ($U_1 = -U_2$)

$$\frac{p_{max}}{p_\infty} = (1 + \tfrac{1}{2}(\gamma - 1)M^2)^{\gamma/(\gamma-1)}. \tag{9.38}$$

Above M_{crit} we use the above formula with $M = M_{crit}$, which corresponds to flow stagnating around sonic eddies. For incompressible mixing layers the pressure rise $p_{max} - p_\infty$ equals $\frac{1}{2}\rho_\infty(\frac{1}{2}\Delta U)^2$. This value is obtained if the limit $M \to 0$ is taken and is also predicted by Bernoulli's law. Physically, the incompressible limit does not necessarily mean that the velocity difference is reduced to zero; it can also mean that the speed of sound tends to infinity.

The results for the pressure variations are summarised on figure 9.4. Smoothing has been applied to the pressure data to remove the discontinuity in the slope at M_{crit}. This only affects the curves in the immediate vicinity of M_{crit}. Figure 9.4a shows pressure relative to free-stream pressure plotted against Mach number. The solid lines are the pressure in the core of the vortex and the pressure at the

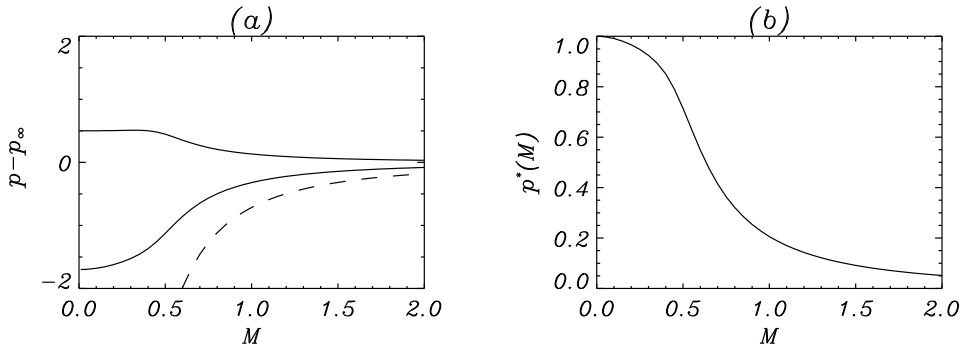

Figure 9.4: Results of the pressure model (a) pressure maximum and minimum (solid lines) relative to the free-stream pressure, also showing the lowest possible relative pressure corresponding to zero pressure in the vortex cores (dashed line), (b) the pressure reduction function $p^*(M)$ showing the strong reduction with increasing Mach number for eddies contributing to the rapid part of the pressure-strain.

stagnation point. The dashed line shows the curve for zero pressure. It can be seen how both the absolute relative core and stagnation pressures reduce as the Mach number is increased to satisfy the constraint that the pressure cannot drop below zero. Figure 9.4b shows the parameter $p^*(M)$ defined by equation (9.30), which is equal to the growth rate reduction if the Reynolds stress and dissipation are isotropic. A simple qualitative explanation for the growth rate reduction is that growth rate is proportional to pressure-strain and the pressure fluctuations must reduce as the Mach number is increased to avoid negative pressures.

9.3.3 Anisotropy effects

We have seen that a simple isotropic picture of turbulence in the compressible mixing layer is sufficient to explain qualitatively the growth rate reduction. However, for quantitative predictions we need to consider the anisotropy of the turbulence. A certain amount of turbulence modelling is required to get a closed form and we need to distinguish clearly where approximations are made. We regard the following as accurate and well supported by the data: (a) $P_{11} = 4\delta'$, as derived in subsection 9.2.1, (b) negligible pressure-dilatation, and hence from the turbulence kinetic energy equation $\epsilon = \delta'(2-k)$, and (c) negligible dilatation dissipation.

Our main model equation is equation (9.26), using the pressure reduction function (9.30) on the rapid pressure-strain and the usual Rotta form for the

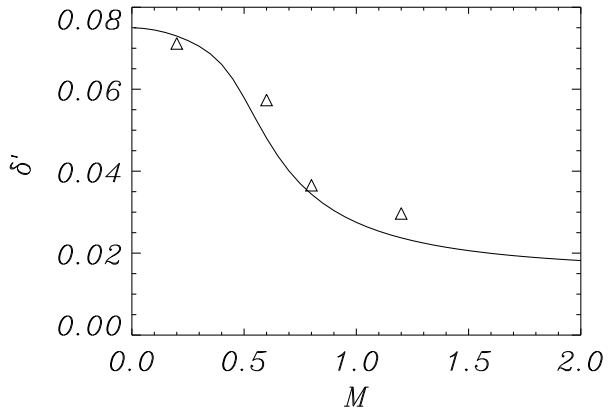

Figure 9.5: Graph of the model prediction for growth rate δ' (solid line), compared with simulation data (symbols).

slow pressure-strain term. For the time being, isotropic dissipation is assumed ($e_{11} = 0$). Thus,

$$\delta' = \frac{c_1 p^*(M) + c_2 \epsilon b_{11}}{8/3 - b_{11} k}. \tag{9.39}$$

Since there is a move to more streamwise turbulence structures as the Mach number is increased, it is expected that the anisotropy of the turbulence will change. By analogy with other flows where streamwise structure becomes important we expect the anisotropy b_{11} to increase. A model that leads to a relatively simple closed-form solution is

$$b_{11} = \frac{c_3}{\delta'} \tag{9.40}$$

Another possibility would be to model b_{11} as proportional to ϵ/k^2 which has a similar Mach number dependence to δ'.

Finally, we need to say something about the individual components. The normal and spanwise stresses are assumed to be equal and to decrease according to the growth rate

$$R_{22} = R_{33} = c_4 \delta', \tag{9.41}$$

Judging from the data, this is a very accurate choice.

As model constants we use $c_1 = 0.17$ and $c_2 = 2.5$, $c_3 = 0.009$ and $c_4 = 9$. The Rotta constant c_2 is the same as in usual second moment closures. All other constants are estimated for incompressible flow (roughly equal to the M=0.2 simulation results).

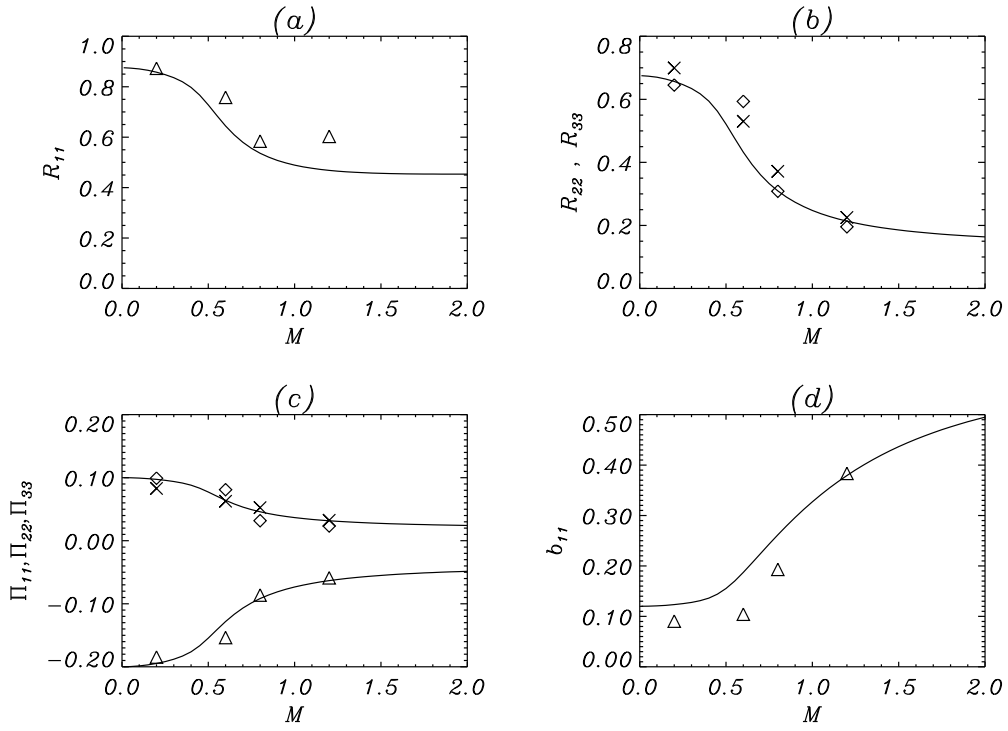

Figure 9.6: Turbulence statistics from model (solid lines) compared with simulation data (triangles for 11-component, crosses for 22, diamonds for 33): (a) Reynolds stress R_{11}, (b) Reynolds stresses R_{22} and R_{33}, (c) pressure-strain Π_{11}, Π_{22} and Π_{33}, and (d) Reynolds stress anisotropy b_{11}.

Putting all of the above together, we can derive a quadratic equation for the growth rate $a\delta'^2 + b\delta' + c = 0$ where the coefficients are related to the model constants by

$$a = \quad 16/9 + c_3c_4(c_2 - 1), \tag{9.42}$$

$$b = \quad -4/3c_3(1 + c_2) - 2/3c_1p^*(M), \tag{9.43}$$

$$c = \quad 1/2c_1c_3p^*(M) + c_2c_3^2. \tag{9.44}$$

Only the largest root of the quadratic is realisable (positive ϵ) and once δ' is known all other quantities can be easily found.

Figures 9.5-7 give the predictions from the model up to $M = 2$, compared with simulation data. Figure 9.5 shows the growth rate against M compared with the simulation data. Figure 9.6-7 shows various turbulence quantities. The

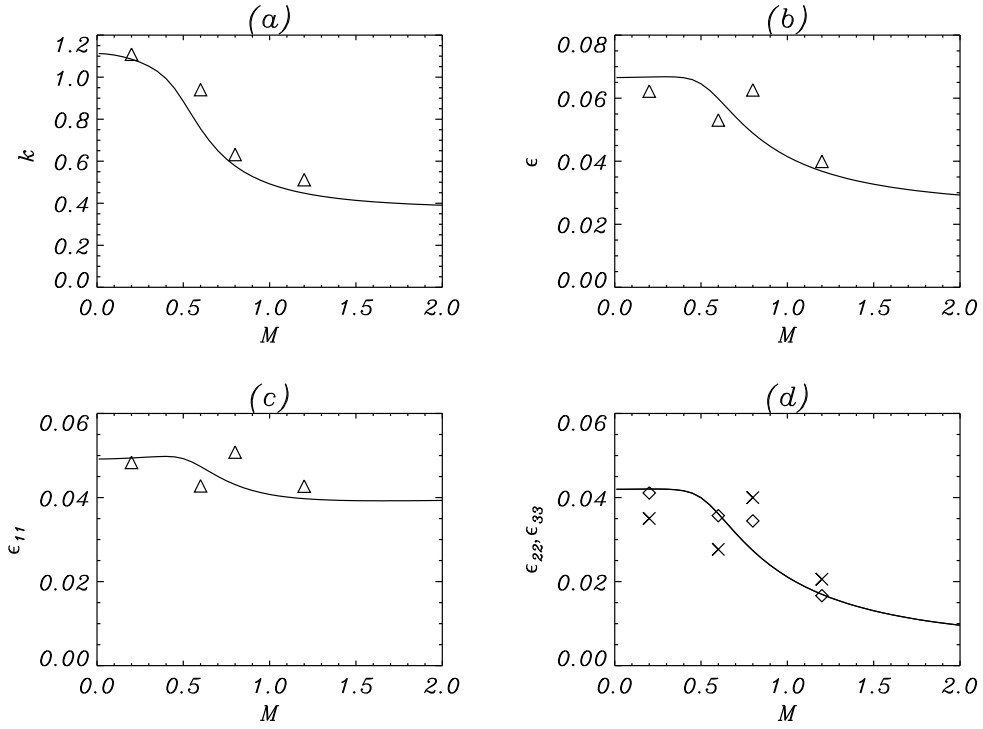

Figure 9.7: Turbulence statistics from model (solid lines) compared with simulation data (triangles for 11-component, crosses for 22, diamonds for 33): (a) turbulence kinetic energy k, (b) dissipation ϵ, (c) dissipation component ϵ_{11}, and (d) dissipation components ϵ_{22} and ϵ_{33}.

behaviour for larger Mach numbers is of considerable interest, but we should caution that there is little experimental or numerical data available between $M = 1.2$ and 2 to validate the model. The Reynolds stresses (figure 9.6a and 9.6b) are in good agreement with the simulation results. The R_{22} and R_{33} components decrease proportional to the growth rate, while the R_{11} component levels out at about half its incompressible level. Figure 9.6c and 9.6d shows the pressure-strain term and Reynolds stress anisotropy b_{11} compared with simulation data. The pressure-strain term especially is in good agreement with the simulation data. Turbulence kinetic energy k and dissipation ϵ are shown on figure 9.7a and 9.7b. The dissipation is unaffected by compressibility at low Mach numbers and only decreases by about a factor of two up to $M = 2$. The dissipation components are shown on figure 9.7c and 9.7d, The lines show the results obtained if one

combines the dissipation anisotropy with the Reynolds stress anisotropy in the Rotta model. This needs no new constants as one can just take a small portion of c_2 (we take 4%) as referring to the dissipation anisotropy. On the whole the anisotropic model gives a better representation of the dissipation components than an assumption of isotropy. One must caution that the simulations have all been conducted at low Reynolds numbers, and it may be that the turbulent cascade is not over a sufficiently wide range of scales to set up isotropy in the dissipation. Thus we cannot make definitive conclusions about the anisotropy of dissipation.

The isotropic model predicts zero growth rate for infinite Mach number, since the growth rate is proportional to $p^*(M)$. The limiting growth rate for $M \to \infty$ provided by the anisotropic model is obtained if $p^*(M) = 0$ is substituted in the coefficients of the quadratic (9.42-9.44). Using the values of the model constants proposed above, we obtain $\delta' \to 0.015$ for $M \to \infty$, which is about 20% of the incompressible growth rate.

The model is well-conditioned, i.e. not very sensitive to variations in the model constants. Additional calculations of the growth rate have been performed in which each of the model constants was changed separately. The relative variations of the growth rate were approximately equal or less than the relative changes of the model constants.

9.4 Discussion

One important observation in this chapter has been that dilatation dissipation and pressure-dilatation are not large in the compressible mixing layer, even when eddy-shocklets are present. Turbulence models constructed using dilatation dissipation or pressure-dilatation are not necessarily invalidated by this, but their claim to be based on the correct physics of the flow would now appear to be false. Some of the initial support for the dilatation dissipation concept came from simulations of isotropic or fully homogeneous compressible turbulence. eddy-shocklets were observed in isotropic and homogeneous shear flow (Lee *et al.* 1991; Blaisdell *et al.* 1991) and the magnitude of the dilatational contribution to dissipation was computed and compared with models for dilatational dissipation, for example that of Sarkar *et al.* (1991). Blaisdell *et al.* found the model by Sarkar *et al.* to be accurate for turbulent Mach numbers below 0.3. For larger turbulent Mach numbers the dilatation dissipation was found to be constant at a level of no more than 10% of the total dissipation. Also Lee *et al.* (1991) found only 5% dilatation dissipation at a turbulent Mach number of 0.5, whereas Sarkar's model would predict 25%. Thus, even in isotropic and homogeneous shear flow, the dilatational terms cannot be regarded as essential in causing reduced growth

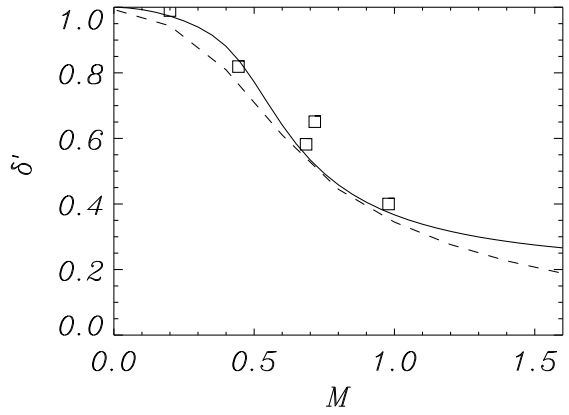

Figure 9.8: Normalised growth rate against Mach number comparing the current model (solid line) with the linear stability result (dashed line) and experimental data from Goebel & Dutton (1991) (symbols).

rates. This is confirmed by recent work on homogeneous shear flow (Sarkar 1995), in which compressibility was found to affect other terms (e.g. production) more than the dissipation. Another recent confirmation is the work by Simone & Cambon (1995), which shows that the effect of compressibility is reflected in pressure-strain correlations and related to the anisotropy of the Reynolds stress tensor, rather than in explicit dilatation terms such as pressure-dilatation and dilatation dissipation. The subject of the latter paper is also homogeneous shear flow, studied by means of DNS and rapid distortion theory (Durbin & Zeman 1992, Cambon *et al.* 1993, Jacquin *et al.* 1993). Furthermore, a different form of splitting the dissipation into solenoidal and dilatational parts has recently been proposed (Huang 1995). This decomposition would predict even smaller dilatational effects.

The mixing layer is very strongly affected by compressibility. Using the model from this chapter, this can be explained by the large pressure fluctuations of the typical eddies in the flow. Similarly large pressure fluctuations and hence Mach number sensitivity would be found in jet and wake flows. Other flows, such as the turbulent boundary layer on a wall, have comparatively much weaker pressure fluctuations and the effects of compressibility do not appear until much higher Mach numbers.

In the introduction it was remarked that the reduction in growth rates with Mach number for the most unstable waves from linear stability theory matches

almost exactly the reduction in shear layer growth rate of the fully turbulent flow. On figure 9.8 we compare the growth rate reduction from temporal stability theory with the result from the turbulence model of section 9.3.3 and experimental data from Goebel & Dutton (1991). The latter is chosen because the density ratio across the shear layer is always less than 2:1, so that these data are comparatively insensitive to the model for incompressible growth rate used for normalisation. As can be seen there is a good correlation between the two curves and the experiments. To examine the relation further we consider the same averaging procedure of section 9.2, applied to the linear stability results.

In temporal linear stability theory of the mixing layer the fluctuating variables have the following form:

$$\phi(x,y,z,t) = (\hat{\phi}^r(x_2) + i\hat{\phi}^i(x_2))e^{\omega_i t + i(\alpha x_1 + \beta x_3)}, \tag{9.45}$$

where ω_i is the temporal growth rate, α and β are the streamwise and spanwise wavenumbers, i is the imaginary unit and $\hat{\phi}^r$ and $\hat{\phi}^i$ are the real and imaginary part of the eigenfunction $\hat{\phi}$. The integrated diagonal Reynolds stress equations reduce to

$$\begin{aligned}
\omega_i \|\hat{u}_1\|^2 &= \hat{P}_{11} + \hat{\Pi}_{11}, & (9.46)\\
\omega_i \|\hat{u}_2\|^2 &= \hat{\Pi}_{22}, & (9.47)\\
\omega_i \|\hat{u}_3\|^2 &= \hat{\Pi}_{33}, & (9.48)
\end{aligned}$$

where $\|\hat{\phi}\|^2 = \int |\hat{\phi}|^2 dx_2$ and the terms on the right-hand side reflect production and pressure-strain:

$$\begin{aligned}
\hat{P}_{11} &= -\int (\hat{u}_1^r \hat{u}_2^r + \hat{u}_1^i \hat{u}_2^i) \frac{d\bar{u}_1}{dx_2} dx_2, & (9.49)\\
\hat{\Pi}_{11} &= \alpha \int (\hat{p}^i \hat{u}_1^r - \hat{p}^r \hat{u}_1^i) dx_2, & (9.50)\\
\hat{\Pi}_{22} &= \int (\hat{p}^r \frac{d\hat{u}_2^r}{dx_2} + \hat{p}^i \frac{d\hat{u}_2^i}{dx_2}) dx_2, & (9.51)\\
\hat{\Pi}_{33} &= \beta \int (\hat{p}^i \hat{u}_3^r - \hat{p}^r \hat{u}_3^i) dx_2. & (9.52)
\end{aligned}$$

In the derivation we have assumed $\bar{\rho} = 1$ following Blumen (1970). The pressure eigenfunction satisfies the following relation (Blumen 1970):

$$\omega_i M^2 \|\hat{p}\|^2 = -\hat{\Pi}_{kk}. \tag{9.53}$$

We observe that positive growth rate implies $\hat{\Pi}_{22} > 0$, $\hat{\Pi}_{33} > 0$, $\hat{\Pi}_{kk} < 0$ and, consequently, $\hat{\Pi}_{11} < 0$ and $|\hat{\Pi}_{kk}| < |\hat{\Pi}_{11}|$. Furthermore, negative $\hat{\Pi}_{11}$ implies

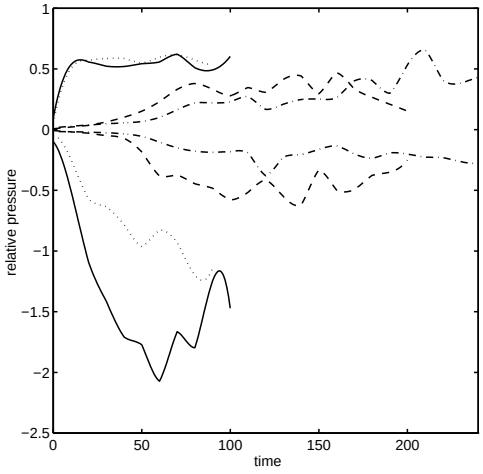

Figure 9.9: Maximum and minimum pressures relative to free-stream pressure during simulations at $M = 0.2$ (solid), 0.6 (dotted), 0.8 (dashed) and 1.2 (chain dotted), showing the large reduction of pressure depressions as Mach number is increased.

positive $\hat{P}_{11}$. Hence, the production and pressure-strain terms in the linear regime have the same sign as in the turbulent regime. One difference in the linear regime is that an analogue of the relation between growth rate and production does not seem to exist. Thus the equations cannot be closed in exactly the same way as the equations for self-similar turbulent flow. We have solved the linear stability problem for several Mach numbers from 0.0 up to 1.6 and obtained the most unstable mode normalised with $\|\hat{u}_1\| = 1$ for each Mach number. Up to $M = 0.6$ the production and pressure-strain decrease in exact proportion to the growth rate ω_i, as in the turbulent case. However, above $M = 0.6$ the pressure-strain drops more rapidly than production and both drop more rapidly than the linear growth rate. The explanation for this latter behaviour is not clear but may be related to the change to oblique disturbances in the stability theory above $M = 0.6$. Furthermore, the square pressure fluctuation $\|\hat{p}\|^2$ rapidly drops for $M > 0.6$. Thus the pressure-dilatation $\hat{\Pi}_{kk}$, satisfying equation (9.53), stops growing at high Mach number. Although we are not able to close the equations in the linear regime, it does seem that substantially the same physical phenomena are occurring, which goes some way towards explaining why the stability growth rate matches the turbulent shear layer growth rate.

The agreement between the actual level of the pressure fluctuations and the model predictions is reasonable. Figure 9.9 shows $p^+ = p_{max} - p_\infty$ and $-p^- = -(p_\infty - p_{min})$ plotted against time as obtained from the simulations. The

reference pressure p_∞ equals 16.85, 1.98, 1.12 and 0.50 for the different Mach numbers respectively. We observe large drop in p^-, whereas p^+ stays at a more constant level. Since the values for p^- at $M = 0.2$ are considerably larger than p_∞ at $M = 1.2$, p^- must decrease with increasing Mach number in order to keep the minimum pressure positive. However, whereas the actual level of p^- is in good agreement with the model prediction, p^+ at higher Mach numbers is larger than the model prediction. This could be due to different types of eddy contributing to the pressure field. There are eddies that contribute to the rapid pressure-strain (the part that depends on mean velocity gradients and modelled in section 9.3) and eddies that contribute to the slow part. For the latter types of vortices the pressures may be higher than those obtained with the isentropic model. Furthermore, shocks will also give rise to higher pressure maxima than predicted with isentropic assumptions, since the entropy of the fluid increases when passing through a shock. The high pressure then comes from a supersonic eddy which generates a shock wave. Supersonic eddies may be present in the flow, but according to Breidenthal (1990) do not have time to rotate and contribute to mixing and growth rate. If the parameter $p^*(M)$ is corrected for higher pressures at higher Mach numbers, the predicted growth rate will be somewhat larger. Reasonable agreement with experimental and simulation data is nevertheless still obtained, if $p_{max} = p_\infty + 0.5$ is substituted in equation (9.30), assuming that p^+ does not exceed its incompressible value (0.5 for $\Delta U = 2$ and $\rho_\infty = 1$).

9.5 Conclusions

Detailed analysis has been made of DNS-databases of compressible mixing layers with convective Mach number M ranging from 0.2 to 1.2. All simulations contained a fully-resolved turbulent energy cascade to small spatial scales. The simulations showed a reduction in growth rate matching the reduction found in previous experimental work. Statistical information was extracted from the databases to determine reasons for the reduced growth rate that is observed as the convective Mach number is increased. It was found that the dilatational contribution to dissipation is negligible even when eddy-shocklets were observed in the flow. Also pressure-dilatation was not found to be significant. Therefore the eddy-shocklets, and the dilatational terms in the averaged equations, were not found to be important for understanding the reduced growth rate.

It was shown that reduced pressure fluctuations were responsible for the changes in growth rate via the rapid pressure-strain term. The analysis was based on the integrated equations for the Reynolds stress tensor and an accurate relation between between the momentum thickness growth rate and the integrated production of turbulence kinetic energy was derived. Furthermore,

a deterministic model for the required pressure fluctuations was given based on the structure of variable density vortices and the assumption that the limiting eddies for the rapid pressure-strain term are sonic. Simple anisotropy considerations closed the model which was then demonstrated to predict the variation of integrated Reynolds stresses, pressure-strain terms, and dissipation, in good agreement with the DNS-data.

Chapter 10

Conclusions and recommendations

In section 1.3 the main purposes of this thesis were stated: to advance the Large-Eddy Simulation technique for compressible flows and to study the effects of compressibility on physical processes in the turbulent mixing layer.

To advance LES for compressible flows, we focussed on subgrid modelling. The essential subgrid-term in incompressible LES, the turbulent stress tensor τ_{ij}, is also the main subgrid-term in compressible LES. In addition the governing equations for compressible LES contain the so-called energy subgrid-terms α_{1-6} (chapter 2).

The six subgrid-models for τ_{ij} investigated in this thesis were formulated in chapter 3. The models taken from literature are: the Smagorinsky, similarity, gradient and dynamic eddy-viscosity models. The dynamic mixed model was also proposed by others, but we altered the formulation in order to remove a mathematical inconsistency. Furthermore, we introduced the dynamic Clark model, which is the gradient model supplemented with a dynamic eddy-viscosity. Using a 1D-analysis and 3D-simulations, the pure gradient model was shown to be severely unstable. However, the instability can be overcome if sufficient viscosity is added and, therefore, the dynamic Clark model was proposed. Furthermore, we proposed an optimal value for the consecutive filter width needed if the dynamic procedure is applied using top-hat filters.

In chapter 4 we showed that τ_{ij} is positive definite if and only if the filter function is positive. Among the three common filters, the top-hat and Gaussian filters give thus rise to a positive subgrid kinetic energy $k = \tau_{ii}/2$, but the spectral cut-off filter causes negative values of k. Such 'realizability conditions' show that the choice of a subgrid-model should take the filter type into account. Imposing these conditions on eddy-viscosity models provided a lower bound for k.

A systematic comparison of the six models for τ_{ij} was performed using LES and DNS of the mixing layer at low Mach number (chapter 5). The Large-Eddy Simulations were compared with filtered DNS results in so-called *a posteriori* tests and afterwards a set of Large-Eddy Simulations at high Reynolds number was obtained for a case in which no DNS can yet be performed. From the *a posteriori* tests it appeared that the dynamic models accurately model the dissipation to subgrid scales, when compared to the other models. The most accurate results were obtained with the (computationally most expensive) dynamic mixed model. Comparison of the models at high Reynolds number confirmed the relative accuracy of the dynamic models, but revealed a somewhat different picture regarding the best model within the group of dynamic models. If we desire the turbulent state of the mixing layer to be as self-similar as possible, the dynamic eddy-viscosity model seems to be better than the dynamic mixed and dynamic Clark model. However, all dynamic models turned out to be much better than the other (non-dynamic) models studied. The Smagorinsky model was too dissipative, and simulations with the similarity and gradient model were unstable, like the simulation without any subgrid-model. These simulations at high Reynolds number illustrate the value of LES. In a case where DNS is not possible with the current computer capacity, acceptable results are obtained using LES, provided a good subgrid-model is used.

In chapter 6 we addressed the role of the numerical errors in LES. It appeared that the results are not sufficiently independent of the specific numerical scheme when the common filter width $\Delta = h$ is used. The simulations should rather be conducted but rather at $\Delta = 2h$, in which case the fourth-order scheme (a new scheme based on weighted central differences, section 2.3) was found to be more accurate than the second-order scheme.

Large-Eddy Simulations of a moderately ($M = 0.6$) and highly compressible mixing layer ($M = 1.2$) were also conducted (chapter 7) and their results were compared with DNS-data. Comparison of the dynamic eddy-viscosity and the dynamic mixed model for τ_{ij} in *a posteriori* tests showed that the first model is more accurate at moderate and high Mach number. The energy subgrid-terms, extensively studied in this chapter, do not play a major role in actual LES of these compressible mixing layers. The *a priori* tests demonstrated that in the group of energy subgrid-terms the four terms α_{1-4} are more or less equally important. This is an interesting result, since in the compressible Large-Eddy Simulations reported in literature only α_{1-2} are taken into account. We subsequently developed new dynamic models for the energy equation modelling the four subgrid-terms α_{1-4}. The inclusion of these models for the energy subgrid-terms in LES of the compressible mixing layer has very small effects on momentum related quantities (even at $M = 1.2$), but the effects on thermodynamic quantities are larger and

increase with Mach number. Furthermore, since energy subgrid-terms partially cancel each other, omitting all energy subgrid-terms in LES was found to be preferred over omitting α_{3-4} only.

The effects of compressibility on physical processes in the turbulent mixing layer were studied by means of Direct Numerical Simulations in chapters 8 and 9. In chapter 8 DNS at convective Mach number $M = 1.2$ was performed. The mixing layer at $M = 1.2$ could be simulated further into the nonlinear regime than previous simulations reported in literature. It was the first time that shock-waves were detected in numerical simulations of the three-dimensional mixing layer. A numerical discretization scheme consisting of fourth-order central differences and third-order upwind differences was proposed in order to capture shocks together with an accurate representation of the transitional and turbulent flow features. Shock-waves occurred at several times and existed for relatively short times. They were found to be created by different types of turbulent vortices.

In chapter 9 we presented a new physical explanation for the mixing layer growth rate reduction with increasing Mach number. Four DNS-databases covering the convective Mach numbers 0.2, 0.6, 0.8 and 1.2 were investigated by calculating turbulent statistics. Previous explanations in literature assumed a significant contribution of the dilatational terms in the Reynolds stress transport equations. We showed that (even in the presence of shocks) these terms are not important in compressible mixing layers. After the derivation of a relation between momentum thickness and the production term, we were able to connect the reduced growth rate to reduced pressure fluctuations through the rapid pressure-strain term. A deterministic model was constructed, based on the pressure fluctuations in compressible vortices, and modified to include anisotropy effects. It predicts the growth rate reduction in good agreement with experimental and simulation data.

Finally a number of recommendations for future research are made. The attempt to answer scientific questions always leaves some questions unanswered and raises new questions.

At this point no definite answer can be given whether the dynamic eddy-viscosity or the dynamic mixed model is most appropriate for LES. Tests at low Mach number and relatively low Reynolds number showed the second model to be the most accurate, in agreement with other recent work (Zang *et al.* 1993, Wu & Squires 1995). However, in our high Reynolds number calculations and in particular in our simulations at higher Mach number the dynamic eddy-viscosity model led to better results. Although in section 5.3.2. a first attempt was made to explain the different behaviour, the results should be further analysed to give a complete explanation. Testing these models in another compressible flow would be a useful extension.

The energy subgrid-terms were found not to play an important role in the compressible mixing layers in this thesis (even at $M = 1.2$). It would be interesting to investigate the role of the energy subgrid-terms in mixing layers with large free-stream temperature ratios. In such mixing layers turbulent diffusion and its subgrid contributions are expected to be more prominent.

LES is attractive because of its applicability to flows where no DNS can be performed with the current computers. We have performed LES for a high Reynolds number mixing layer at low Mach number in a large computational domain (section 5.4). To perform such simulations at higher Mach numbers too and investigate whether a self-similar state is reached could be the next step.

Furthermore, the shocks present in the DNS at $M = 1.2$ could be explored in relation with LES. Their effect on the structure of the turbulent stress tensor can be investigated using *a priori* tests on the present DNS-database and possible implications for subgrid-modelling could be deduced. Furthermore, in chapter 8 we used an upwind scheme when necessary to capture shocks. From the few Large-Eddy Simulations that we performed at $M = 1.2$ (chapter 7), we did not yet find such a scheme necessary in order to obtain good LES-results. It could be that the dynamic eddy-viscosity is able to supply the additional dissipation required to smooth the shock, but this issue certainly requires more research.

From chapter 9 it appeared that the compressible shear layer growth is not connected to dissipation, but rather to production and pressure-strain. Production is determined by the large scales and initiates the turbulent energy cascade, whereas dissipation mainly happens at the small scales. It could indicate that the large-scale turbulence is considerably altered by compressibility while the small eddies keep a more incompressible character. This statement is in agreement with our finding that, in order to obtain accurate LES, it does not seem necessary to take compressibility effects into account in subgrid modelling by modelling the energy subgrid-terms (chapter 7). The shock-waves obviously seem to contradict the statement, since shocks are compressible phenomena that clearly contribute to small scales. However, chapters 8 and 9 show that the shocks do not long exist and marginally contribute to the turbulent statistics. Shocks not created by turbulent vortices may have larger significance. An example is the flow over a transonic wing, in which the shock strongly increases the displacement thickness (Brandsma & Kuerten 1990). In any case more research is needed to study the possibly different roles of compressibility in large- and small-scale turbulence.

In this thesis we simulated temporal mixing layers. Spatial simulations are more realistic than temporal simulations, but require much more computer time. However, it is feasible to study spatially developing compressible flows with LES. Even DNS of such flows can soon be performed if the computer capacity continues to increase. In future research the 3-D spatial compressible mixing layer could

be simulated, and the standard opinion that spatial and temporal mixing layers have the essential things in common could be verified.

Although in recent years the knowledge about turbulence has increased and progress in modelling has been made, much is still unknown about this complicated phenomenon with so many different aspects. Thus, at the end of this thesis the subject of turbulence looks even more challenging than at the beginning.

Bibliography

Bardina, J., Ferziger, J.H., and Reynolds, W.C. (1984). Improved turbulence models based on LES of homogeneous incompressible turbulent flows. Department of Mechanical Engineering. *Report No. TF-19*, Stanford.

Birch, S.F. and Eggers, J.M. (1973). A critical review of the experimental data for developed free turbulent shear layers. *NASA SP-321*, 11-40.

Blaisdell, G.A., Mansour, N.N., and Reynolds, W.C. (1991). Numerical simulation of compressible homogeneous turbulence. Department of Mechanical Engineering. *Report No. TF-50*, Stanford.

Blaisdell, G.A., Mansour, N.N. and Reynolds, W.C. (1993). Compressibility effects on the growth and structure of homogeneous turbulent shear flow. *J. Fluid Mech.*, **256**,443-485.

Blumen, W. (1970). Shear layer instability of an inviscid compressible fluid. *J. Fluid Mech.*, **40**, 769-781.

Bogdanoff, D.W. (1983). Compressibility effects in turbulent shear layers. *AIAA J.*, **21**, 926-927.

Bradshaw, P. (1977). Compressible turbulent shear layers. *Ann. Rev. Fluid Mech.*, **9**, 33-54.

Brandsma, F.J., and Kuerten, J.G.M. (1990). The ISNaS Compressible Navier-Stokes Solver; First Results for Single Airfoils. *Lecture Notes in Physics 371*, Springer-Verlag, 152-156.

Breidenthal, R. (1990). The sonic eddy - a model for compressible turbulence. AIAA 90-0495, 28th Aerospace Sciences Meetings.

Brownand, F.K., and Latigo, B.O. (1979). Growth of the two-dimensional mixing layer from a turbulent and nonturbulent boundary layer. *Phys. of Fluids*, **22**, 1011.

Brown, G.L., and Roshko, A. (1974). On density effects and large structure in turbulent mixing layers. *J. Fluid Mech.*, **64**, 775-816.

Cambon, C., Coleman, G.N., and Mansour, N.N. (1993). Rapid distortion analysis and direct simulation of compressible homogeneous turbulence at finite Mach number. *J. Fluid Mech.*, **257**, 641-665.

Carati, D., Ghosal, S., and Moin, P. (1995). On the representation of backscatter in dynamic localization models. *Phys. of Fluids*, **7**, 606-616.

Chatelin, F. (1993). *Eigenvalues of matrices*. John Wiley & Sons, Chichester.

Clark, R.A., Ferziger, J.H., and Reynolds, W.C. (1979). Evaluation of subgrid-scale models using an accurately simulated turbulent flow. *J. Fluid Mech.*, **91**, 1-16.

Clemens, N.T. and Mungal, M.G. (1992). Two- and three-dimensional effects in the supersonic mixing layer. *AIAA J.*, **30**, 973-981.

Clemens, N.T. and Mungal, M.G. (1995). Large-scale structure and entrainment in the supersonic mixing layer. *J. Fluid Mech.*, **284**, 171-216.

Comte, P., Lesieur, M., and Lamballais, E. (1992). Large and small-scale stirring of vorticity and a passive scalar in a 3D temporal mixing layer. *Phys. Fluids A*, **4**, 2761.

Deardorff, J.W. (1970). A numerical study of three-dimensional turbulent channel flow at large Reynolds numbers. *J. Fluid Mech.*, **41**, 453-480.

Deardorff, J.W. (1971). On the magnitude of the subgrid scale eddy viscosity coefficient. *J. Comp. Phys.*, **7**, 120-133.

Durbin, P.A., and Zeman, O. (1992). Rapid distortion theory for homogeneous compressed turbulence with application to modelling. *J. Fluid Mech.*, **242**, 349-370.

Du Vachat, R. (1977). Realizability inequalities in turbulent flows. *Phys. Fluids*, **20**, 551-556.

Eidson, T.M. (1985). Numerical simulation of the turbulent Rayleigh-Bénard problem using subgrid modelling. *J. Fluid Mech.*, **158**, 245-268.

El Baz, A.M., and Launder, B.E. (1993). Second-moment modelling of compressible mixing layers. *Engineering Turbulence Modelling and Experiments 2*, W. Rodi and F. Martelli (Editors), Elsevier.

El-Hady, N.M., Zang, T.A. and Piomelli, U. (1993). Dynamic subgrid-scale modelling for high-speed transitional boundary layers. *ASME FED-Vol. 162*, 103-112.

Elliott, G.S. and Samimy, M. (1990). Compressibility effects in free shear layers. *Phys. Fluids A*, **2**, 1231-1240.

Erlebacher, G., Hussaini, M.Y., Speziale, C.G., and Zang, T.A. (1987). Toward the large-eddy simulations of compressible turbulent flows. *ICASE Report No. 87-20*.

Erlebacher, G., Hussaini, M.Y., Speziale, C.G., and Zang, T.A. (1992). Toward the large-eddy simulations of compressible turbulent flows. *J. Fluid Mech.*, **238**, 155-185.

Favre, A. (1983). Turbulence: space-time statistical properties and behavior in supersonic flows. *Phys. Fluids*, **26**, 2851-2863.

Germano, M., Piomelli, U., Moin, P., and Cabot, W.H. (1991). A dynamic subgrid-scale eddy viscosity model. *Phys. Fluids A*, **3**, 1760-1765.

Germano, M. (1992). Turbulence: the filtering approach. *J. Fluid Mech.*, **238**, 325-336.

Geurts, B.J., Kuerten, J.G.M, Vreman, A.W., Theofilis V., and Zandbergen, P.J. (1993a). A finite volume approach to compressible large eddy simulation. *Applied Scientific Research*, **51**, 325-329.

Geurts, B.J., Vreman, B., Kuerten, H., and Theofilis, V. (1993b). LES Modeling errors in free and wall bounded compressible shear layers. *Engineering Turbulence Modelling and Experiments 2*, eds. W. Rodi, F. Martelli, Elsevier, 325-334.

Geurts, B., Vreman B., and Kuerten, H. (1994). Comparison of DNS and LES of transitional and turbulent compressible flow: flat plate and mixing layer. *Application of Direct and Large Eddy Simulation to Transition and Turbulence*, AGARD Conference Proceedings 551, 5.1-14.

Ghosal, S., Lund, T.S., Moin, P., and Akselvoll, K. (1995). A dynamic localization model for large-eddy simulation of turbulent flows. *J. Fluid Mech.*, **286**, 229-255.

Ghosal, S., and Moin, P. (1995). The basic equations for the large eddy simulation of turbulent flows in complex geometry. *J. Comp. Phys.*, **118**, 24-37.

Goebel, S.G. and Dutton, J.C. (1991). Experimental study of compressible turbulent mixing layers. *AIAA J.*, **29**, 538-546.

Henningson, D.S., and Reddy, S.C. (1994). On the role of linear mechanisms in transition to turbulence. *Phys. Fluids*, **6**, 1396-1398.

Horiuti, K. (1985). Large Eddy Simulation of turbulent channel flow by one- equation modeling. *J. Phys. Soc. Japan*, **54**, 2855-2865.

Horiuti, K. (1995). Backward cascade of subgrid-scale kinetic energy in wall bounded and free turbulent flows. *Proceedings Turbulent Shear Flows 10*, The Pennsylvania State University, 20.13-18.

Huang, P.G. (1995). Relations between viscous diffusion and dissipation of turbulent kinetic energy. *Proceedings Turbulent Shear Flows 10*, The Pennsylvania State University, P2.79-84.

Humi, M. (1990). Optimal large eddy simulation in one dimension. *Phys. Fluids A*, **2**, 1046-1048.

Jameson, A. (1983). Transonic flow calculations. *MAE-Report 1651*, Princeton University.

Jiménez-Härtel, C.J. (1994). Analyse und Modellierung der Feinstruktur im wandnahen Bereich turbulenter Scherströmungen. *Forschungsbericht 94-22*, Institut für Strömungsmechanik, Göttingen.

Kolmogorov, A.N. (1941). The local structure of turbulence in incompressible viscous fluid for very large Reynolds numbers. *Dokl. Akad. Nauk. SSSR*, **30**, 301-305. Reprinted in 1991, *Proc. R. Soc. Lond. A*, **434**, 9-13.

Kuerten, J.G.M., Geurts, B.J., Van der Burg, J.W., Vreman A.W., and Zandbergen, P.J. (1993). Development and applications of a 3D compressible Navier-Stokes solver. *Proceedings of the Thirteenth International Conference on Numerical Methods in Fluid*

Dynamics, eds. M. Napolitano and F. Sabetta (Springer-Verlag, Berlin), 529-533.

Kwak, D., Reynolds, W.C., and Ferziger, J.H. (1975). Three-dimensional time dependent computation of turbulent flow. *Report TF-5*, Stanford.

Lee, S. and Lele, S.K. and Moin, P. (1991). Eddy shocklets in decaying compressible turbulence. *Phys. Fluids A*, **3**, 657-664.

Lele, S.K. (1989). Direct Numerical Simulation of Compressible Free Shear Flows. *AIAA Paper* 89-0374.

Lele, S.K. (1994). Compressibility effects on turbulence. *Ann. Rev. Fluid Mech.*, **26**, 211-254.

Leith, C.E. (1990). Stochastic backscatter in a subgrid-scale model: Plane shear mixing layer. *Phys. Fluids A*, **2**, 297-299.

Lesieur, M. (1990). *Turbulence in Fluids*. Kluwer Academic Publishers, Dordrecht.

Lesieur, M., Staquet, C., Le Roy, P., and Comte, P. (1988). The mixing layer and its coherence examined from the point of view of two-dimensional turbulence. *J. Fluid Mech.*, **192**, 511-534.

Lilly, D.K. (1967). The representation of small-scale turbulence in numerical simulation experiments. *Proceedings of the IBM scientific Computing Symposium on Environmental Sciences* IBM Form no. 320-1951, 195-210.

Lilly, D.K. (1992). A proposed modification of the Germano subgrid-scale closure method. *Phys. Fluids A*, **4**, 633-635.

Liu, S., Meneveau, C., and Katz, J. (1994). On the properties of similarity subgrid-scale models as deduced from measurements in a turbulent jet. *J. Fluid Mech.*, **275**, 83-119.

Love, M.D. (1980). Subgrid modelling studies with Burgers' equation. *J. Fluid Mech.*, **100**, 87-110.

Lu, G. and Lele, S.K. (1994). On the density ratio effect on the growth rate of a compressible mixing layer. *Phys. of Fluids*, **6**, 1073-1075.

Lu, P.J., and Wu, K.C. (1992). Assessment of total variation diminishing schemes in compressible mixing flow computations. *AIAA Journal*, **4**, 939-946.

Luo, K.H. and Sandham, N.D. (1994). On the formation of small scales in a compressible mixing layer. In *Direct and Large-Eddy Simulation I*, Kluwer Academic Publishers, 335-346.

Luo, K.H. and Sandham, N.D. (1995). Reynolds number effects on transitional compressible free shear flows: direct numerical simulation. in *Proc. First Asian Computational Fluid Dynamics Conference*, Hong Kong, January 16-19, 403-408.

Meneveau, C. (1994). Statistics of turbulence subgrid-scale stresses: Necessary conditions and experimental tests. *Phys. Fluids*, **6**, 815-833.

Michalke, A. (1964). On the inviscid instability of the hyperbolic-tangent velocity profile. *J. Fluid Mech.*, **13**, 543-556.

Moin, P., and Jimenez, J. (1993). Large Eddy Simulation of complex turbulent flows. *AIAA 24th Fluid Dynamics Conference*, Orlando.

Moin, P., and Kim, P. (1982). Numerical investigation of turbulent channel flow. *J. Fluid Mech.*, **118**, 341-377.

Moin, P., Squires, K., Cabot, W., and Lee, S. (1991). A dynamic subgrid-scale model for compressible turbulence and scalar transport. *Phys. Fluids A*, **3**, 2746-2757.

Monin, A.S., and Yaglom, A.M. (1971). *Statistical Mechanics*. The MIT Press.

Moser, R.D., and Rogers, M. (1993). The three-dimensional evolution of a plane mixing layer: pairing and transition to turbulence. *J. Fluid Mech.*, **247**, 275-320.

Normand, X., and Lesieur, M. (1992). Numerical experiments on transition in the compressible boundary layer. *Theor. Comp. Fluid Dyn.*, **3**, 231-252.

Ortega, J.M. (1987). *Matrix Theory*. Plenum Press, New York.

Papamoschou, D. and Roshko, A. (1988). The compressible turbulent mixing layer: an experimental study. *J. Fluid Mech.*, **197**, 453-477.

Papamoschou, D. (1995). Evidence of shocklets in a counterflow supersonic shear layer. *Phys. of Fluids*, **7**, 233-235.

Papamoschou, D., and Lele, S.K. (1992). Vortex-induced disturbance field in a compressible shear layer. *CTR Proceedings of the Summer Program 1992*, 259-276.

Passot, T., and Pouquet, A. (1987). Numerical simulation of compressible homogeneous flows in the turbulent regime. *J. Fluid Mech.*, **181**, 441-466.

Piomelli, U., Zang, T.A., Speziale, C.G., and Hussaini, M.Y. (1990a). On the large-eddy simulation of transitional wall-bounded flows. *Phys. Fluids A*, **2**, 257-265.

Piomelli, U., Cabot, W.H., Moin, P., and Lee, S. (1990b). Subgrid-scale backscatter in transitional and turbulent flows. *CTR Proceedings of the Summer Program 1990*, 19-30.

Piomelli, U., and Liu, J. (1994). Large-Eddy Simulation of rotating channel flows using a localized dynamic model. *Application of Direct and Large Eddy Simulation to Transition and Turbulence*, AGARD Conference Proceedings 551, 3.1-9.

Ragab, S.A., and Sheen, S. (1992). The nonlinear development of supersonic instability waves in a mixing layer. *Physics of Fluids A*, **4**, 553-566.

Ragab, S.A., and Wu, J.L. (1989). Linear instabilities in two-dimensional compressible mixing layers. *Phys. Fluids A*, **1**, 957-966.

Reynolds, O., (1883). An experimental investigation of the circumstances which determine whether the motion of water shall be direct and sinuous, and the law of resistance in parallel channels. *Phil. Trans. Roy. Soc.*, 51-105.

Reynolds, W.C. (1990). The potential and limitations of direct and large eddy simulations. In: *Whither turbulence? Turbulence at crossroads*, edited by J.L. Lumley, Springer-Verlag, 313.

Richardson, L.F. (1992). *Weather prediction by numerical process.* Cambridge University Press.

Rogallo, R.S., and Moin, P. (1984). Numerical simulation of turbulent flows. *Ann. Rev. Fluid Mech.*, **16**, 99-137.

Rogers, M.M., and Moser, R.D. (1994). Direct simulation of a self-similar turbulent mixing layer. *Phys. of Fluids*, **6**, 903-924.

Rudin, W. (1973). *Functional analysis.* McGraw-Hill, Inc.

Sandham, N.D., and Reynolds, W.C. (1989). A numerical investigation of the compressible mixing layer. *Report TF-45*, Department of Mechanical Engineering, Stanford University.

Sandham, N.D., and Yee, H.C. (1989). A numerical study of a class of TVD schemes for compressible mixing layer. *NASA Technical Memorandum 102194.*

Sandham, N.D., and Reynolds, W.C. (1990). Compressible mixing layer: Linear theory and direct simulation. *AIAA J.*, **28**, 618-624.

Sandham, N.D., and Reynolds, W.C. (1991). Three-dimensional simulations of large eddies in the compressible mixing layer. *J. Fluid Mech.*, **224**, 133-158.

Sarkar, S., Erlebacher, G., Hussaini, M.Y. and Kreiss, H.O. (1991). The analysis and modelling of dilatational terms in compressible turbulence. *J. Fluid Mech.*, **227**, 473-493.

Sarkar, S. (1995). The stabilizing effect of compressibility in turbulent shear flow. *J. Fluid Mech.*, **282**, 163-186.

Schumann, U. (1975). Subgrid scale model for finite difference simulations of turbulent flows in plane channels and annuli. *J. Comput. Phys.*, **18**, 376-404.

Schumann, U. (1977). Realizability of Reynolds-stress turbulence models. *Phys. Fluids*, **20**, 721-725.

Schumann, U. (1991). Direct and large eddy simulation of turbulence - summary of the state-of-the-art 1991. Lecture Series 1991-02: *Introduction to the modeling of turbulence*, Von Karman Institute, Brussels.

Simone, A., and Cambon, C. (1995). Rapid distortion and direct simulation approach to compressibility in turbulent shear flow. *Proceedings Turbulent Shear Flows 10*, The Pennsylvania State University.

Smagorinsky, J. (1963). General circulation experiments with the primitive equations. *Mon. Weather Rev.*, **91**, 99-164.

Speziale, C.G. (1985). Galilean invariance of subgrid-scale stress models in the large eddy simulation of turbulence. *J. Fluid Mech.*, **156**, 55-62.

Speziale, C.G., Erlebacher, G., Zang, T.A., and Hussaini, M.Y. (1988). The subgrid-scale modeling of compressible turbulence. *Phys. Fluids*, **31**, 940-942.

Speziale, C.G., Sarkar, S., and Gatski, T.B. (1991). Modelling the pressure-strain correlation of turbulence: an invariant dynamical systems approach. *J. Fluid Mech.*, **227**,

245-272.

Tennekes, H., and Lumley, J.L. (1972). *A first course in turbulence*. The MIT Press.

Theofilis, V., Vreman, B., Geurts, B., and Kuerten, H. (1993). A finite volume study of compressible shear layer instabilities. *Proceedings ASME-conference*, ASME: FED-155, 71.

Van der Burg, J.W. (1993). Numerical techniques for transonic flow calculations. *Ph. D. Dissertation*, University of Twente.

Vreman, B., Geurts, B., Kuerten, H., and Zandbergen, P. (1992). A finite volume approach to Large Eddy Simulation of compressible, homogeneous, isotropic, decaying turbulence. *Int. J. Num. Meth. Fluids*, **15**, 799-816.

Vreman, B., Geurts, B., and Kuerten, H. (1994a). Realizability conditions for the turbulent stress tensor in Large Eddy Simulation. *J. Fluid Mech.*, **278**, 351-362.

Vreman, B., Geurts, B., and Kuerten, H. (1994b). On the formulation of the dynamic mixed subgrid-scale model. *Phys. Fluids*, **6**, 4057-4059.

Vreman, B., Geurts, B., and Kuerten, H. (1994c). Discretization error dominance over subgrid-terms in Large Eddy Simulation of Compressible Shear Layers in 2D. *Comm. Num. Meth. Eng.*, **10**, 785-790.

Vreman, A.W., Geurts, B.J., and Kuerten, J.G.M. (1994d). Subgrid-modelling in LES of compressible flow. *Direct and Large-Eddy Simulation I*, Eds. P.R. Voke, L. Kleiser and J.P. Chollet, 133-144.

Vreman, B., Kuerten, H., and Geurts, B. (1994e). Comparison of subgrid-models in LES of the compressible mixing layer. *Proceedings ETC-V*, Siena.

Vreman, B., Geurts, B., and Kuerten, H. (1994f). Comparison of subgrid-models in Large Eddy Simulation of the temporal mixing layer. *Memorandum No. 1243*, University of Twente.

Vreman, B., Geurts, B., and Kuerten, H. (1995a). A priori tests of Large Eddy Simulation of the compressible plane mixing layer. *J. Eng. Math.*, **29**, 299-327.

Vreman, B., Geurts, B., and Kuerten, H. (1995b). Subgrid-modelling in LES of compressible flow. *Applied Scientific Research*, **54**, 191-203.

Vreman, B., Geurts, B., and Kuerten, H. (1995c). Large eddy simulation of the temporal mixing layer using the Clark model. *Theoretical and Computational Fluid Dynamics*, to appear.

Vreman, B., Geurts, B., and Kuerten, H. (1995d). Comparison of numerical schemes in Large Eddy Simulation of the temporal mixing layer. *Int. J. Num. Meth. Fluids*, to appear.

Vreman, B., Geurts, B., Kuerten, H., Broeze J., and Wasistho, B. (1995e). Dynamic subgrid-scale models for LES of transitional and turbulent compressible flow in 3-D shear layers. *Proceedings Turbulent Shear Flows 10*, The Pennsylvania State University, 10.25-30.

Vreman, B., Kuerten, H., and Geurts, B. (1995f). Shocks in Direct Numerical Simulation of the confined three-dimensional mixing layer. *Phys. Fluids*, **7**, 2105-2107.

Vreman, B., Kuerten, H., and Geurts, B. (1995g). Shocks in DNS of the three-dimensional mixing layer. *Proceedings Turbulent Shear Flows 10*, The Pennsylvania State University, P3.31-36.

Vreman, A.W., Sandham, N.D., and Luo, K.H. (1995h). Compressible mixing layer growth rate and turbulence characteristics. *J. Fluid Mech.*, submitted.

Wu, X., and Squires, K.D. (1995). Large-eddy simulation of a canonical three-dimensional boundary layer. *Proceedings Turbulent Shear Flows 10*, The Pennsylvania State University, 8.19-24.

Yoshizawa, A. (1986). Statistical theory for compressible turbulent shear flows, with the application to subgrid modeling. *Phys. Fluids*, **29**, 2152-2164.

Zang, T.A., Dahlburg, R.B., and Dahlburg, J.P. (1992). Direct and large-eddy simulations of three-dimensional compressible Navier-Stokes turbulence. *Phys. Fluids A*, **4**, 127-140.

Zang, Y., Street, R.L., and Koseff, J.R. (1993). A dynamic mixed subgrid-scale model and its application to turbulent recirculating flows. *Phys. Fluids A*, **5**, 3186-3196.

Zeman, O. (1990). Dilatation dissipation: The concept and application in modeling compressible mixing layers. *Phys. of Fluids A*, **2**, 178-188.

Zeman, O. (1991). On the decay of compressible isotropic turbulence. *Phys. of Fluids A*, **3**, 951-955.

Acknowledgements

The time for the computations was provided by Stichting Nationale Computerfaciliteiten (National Computing Facilities Foundation, NCF), which is financially supported by the Nederlandse Organisatie van Wetenschappelijk Onderzoek (Netherlands Organization for Scientific Research). NWO also provided financial support for a ten-weeks visit at Queen Mary and Westfield College, London.

Summary

The Large-Eddy Simulation technique of compressible flows and the effect of compressibility on mixing layers are the main subjects of this thesis. Direct Numerical Simulations (DNS) and Large-Eddy Simulations (LES) of the temporal compressible mixing layer at various Mach and Reynolds numbers have been conducted to investigate these subjects.

With respect to the LES technique, Large-Eddy Simulations have been performed at convective Mach numbers 0.2, 0.6 and 1.2 and the results have been compared with filtered DNS-data. It appeared that the dynamic subgrid-models lead to relatively accurate results compared to the other models tested. The dynamic approach turned out to yield acceptable results too in LES of a mixing layer that currently cannot be simulated using DNS. Care has to be taken to ensure that the numerical errors in LES are sufficiently small. It was found that these errors are usually sufficiently small if the filter width equals twice the grid-spacing. In addition to modelling the turbulent stress tensor, compressible LES formally requires the modelling of the subgrid-terms in the energy equation, which do not occur in incompressible LES. However, the compressible Large-Eddy Simulations demonstrated that the turbulent stress tensor is the dominant subgrid-term, even at convective Mach number 1.2. This important subgrid-term was also investigated from a theoretical point of view and realizability conditions for this tensor were derived.

Regarding compressibility effects in the mixing layer, shock-waves were found in the three-dimensional DNS at convective Mach number 1.2. Furthermore, we have investigated the cause of the mixing layer growth rate reduction with increasing compressibility, using four DNS-databases covering the range of convective Mach numbers from 0.2 to 1.2. It was found that the growth rate reduction cannot be explained by the dilatational terms, but rather by the reduced pressure fluctuations, leading to reduced pressure strain and turbulent production terms.